Experimental and Numerical Analysis of the Performance of a Marine Propeller in Oblique Flow

MT MSc Thesis

Bart van Broekhoven

Delft University of Technology

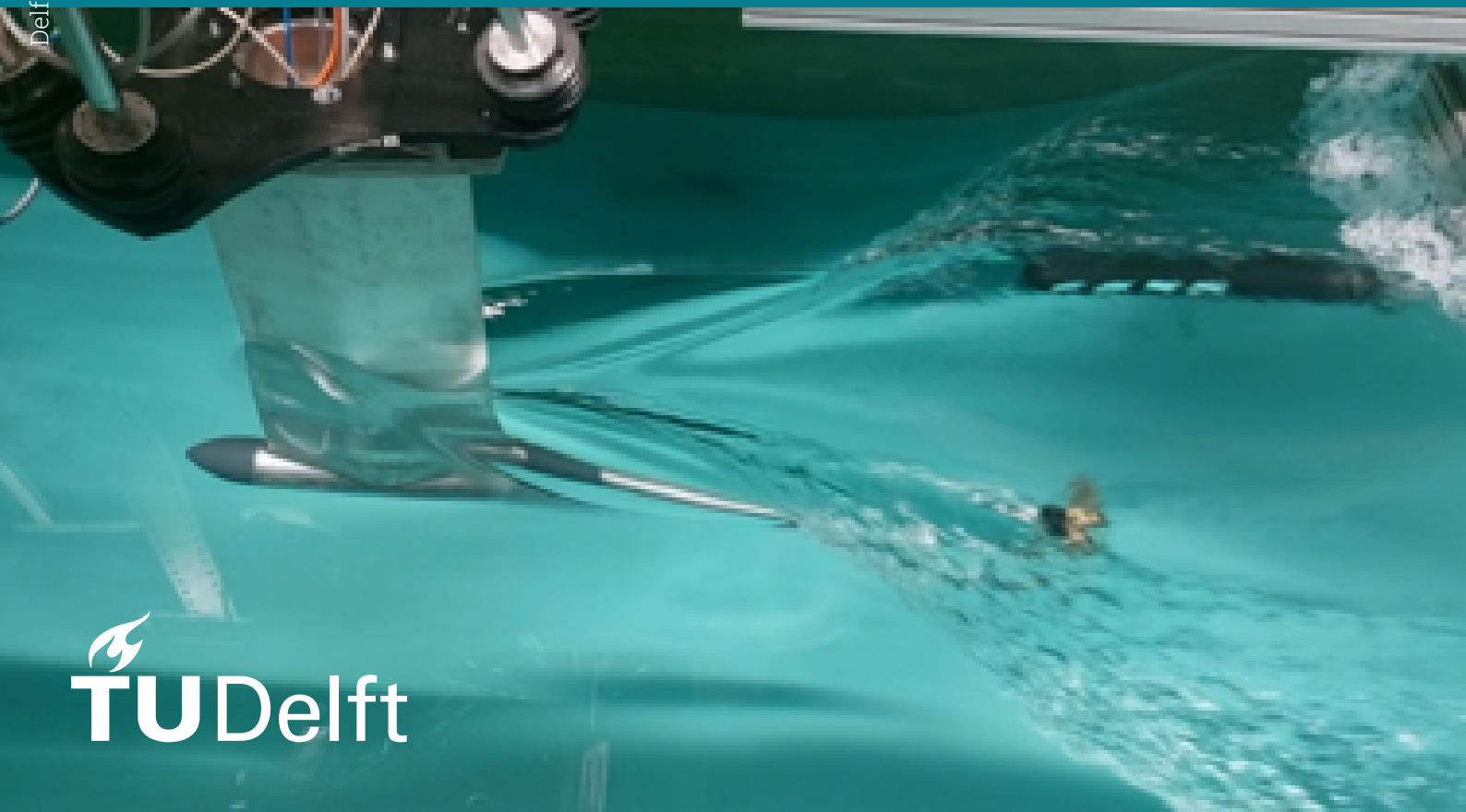

TU Delft

Thesis for the degree of MSc in Marine Technology
in the specialization of Ship Hydromechanics

Experimental and Numerical Analysis of the Performance of a Marine Propeller in Oblique Flow

by

Bart van Broekhoven

Performed at
TU Delft

This thesis MT.25/26.014.M. is classified as confidential in accordance with the general conditions for projects performed by the TU Delft.

To be defended publicly on Friday 28th of November 2025 at 1:30 PM.

Thesis exam committee

Chair/Responsible Professor:	Dr. D. Fiscaletti
Staff Member:	Dr. G. Jacobi
Staff Member:	Prof.Dr.Ir. T.J.C. van Terwisga
Staff Member:	B. Vera Garcia

Author details

Student number:	5415411

Cover: Experimental set-up of the gondola in the MTT Towing Tank.

TU Delft

Preface

This thesis marks the end of my Master's degree in Marine Technology at Delft University of Technology. Over the past two years, my interest in ship hydromechanics grew, which led me to follow most of the courses in this specialization and ultimately perform my thesis on this subject.

Firstly, I would like to thank my daily supervisors, Daniele Fiscaletti and Gunnar Jacobi. Their feedback and insights from their experience with both experimental and numerical challenges were invaluable to my progress with the thesis. I also want to thank Tom van Terwisga and Braulio Vera Garcia for their feedback and suggestions, as well as for being part of the exam committee.

I would also like to thank the technicians of the Towing Tank, who assisted me during the experiments. In particular, I want to thank Peter Poot and Frits Sterk for their help in the preparation and construction of the set-up, and Sedat Tokgoz for his assistance during the execution of the experiments. It was both valuable and enjoyable to gain some experience conducting experiments in the towing tank. Finally, I want to thank my family and friends for their support during this process. Their support kept me motivated for the project.

Lastly, I want to acknowledge the use of AI during the project. I used AI to help generate parts of certain functions in my code, for example for the implementing the FFT of the signals, as well as to rephrase some parts of the text to improve on grammar and style. I carefully reviewed all AI-generated output and remain fully responsible for the content of this thesis.

Bart van Broekhoven
Delft, November 2025

Summary

Wind assisted ship propulsion is one of the realistic options that are considered as alternative ways to propel a ship, with the goal of reducing a ship's emissions. With WASP, the propeller is still needed, but will be less loaded as wind energy takes over part of the required thrust force. Ships that sail are always under a small drift angle. This does not only affect the forces on the ship, but also the performance of the propeller. Previous research studies are mainly focussing on manoeuvring applications. However, an important difference is that the speed of the ship is close to zero here, whilst the drift angles are very high. The goal of this thesis is to experimentally capture the influence of small drift angles on propeller performance. Also, the influence of the advance ratio is studied, as this will vary, as it is dependent on the wind speed.

For the experiment, a gondola is used. The gondola was connected to the HexaPod to alter the position of the gondola and the propeller. The propeller was positioned downstream of the gondola, in pulling condition. The results of the experiments showed that the gondola upstream of the propeller affects the thrust and torque of the propeller for small drift angles. Therefore, measurements were also performed at pitch angles to avoid this influence.

The results show an increase in both thrust and torque for increasing pitch angle. Due to the high uncertainty, the increase is not significant for the smallest angle considered. For experiments performed at higher Reynolds numbers, these experimental uncertainties decreased, and they showed the same trend. Moreover, it was found that the advance ratio also influences the change in thrust and torque. This shows that a lightly-loaded propeller is more prone to fluctuations in the inflow than a highly-loaded propeller.

Lastly, a numerical analysis was performed to also capture the blade loads and the wake of the propeller. Here, an increase in torque was observed for increasing pitch angle. However, this was not the case for thrust. The results showed that thrust and torque on a single blade start to oscillate, also for small angles. The in-plane loads were observed, as a result of imbalance of side and vertical force. The wake also showed the inclination angle and the imbalance of the thrust generation during a propeller revolution.

Contents

List of Figures

List of Tables

Nomenclature

Abbreviations

Abbreviation	Definition
BEMT	Blade Element Momentum Theory
BPF	Blade Passing Frequency
FFT	Fast Fourier Transform
IMO	International Maritime Organization
ITTC	International Towing Tank Conference
RANS	Reynolds-Averaged Navier Stokes
WASP	Wind Assisted Ship Propulsion

Symbols

Symbol	Definition	Unit
A_E	Expanded blade area	[m^2]
A_R	Rudder area	[m^2]
c	Chord length	[m]
$c_{0.7}$	Chord length at 0.7R	[m]
C_D	Drag coefficient	[-]
C_f	Skin friction coefficient	[-]
C_L	Lift coefficient	[-]
C_p	Pressure coefficient	[-]
C_μ	Turbulence model constant	[-]
D	Drag force	[N]
D_p	Propeller diameter	[m]
I	Turbulence intensity	[-]
J	Advance ratio	[-]
k	Turbulent energy	[$\frac{m^2}{s^2}$]
K_T	Thrust coefficient	[-]
K_Q	Torque coefficient	[-]
L	Lift force	[N]
n_p	Propeller rotational velocity	[1/s]
P	Pitch	[m]
p	Pressure	[$\frac{N}{m^2}$]
p_0	Ambient pressure	[$\frac{N}{m^2}$]
P_D	Delivered power	[kW]
P_T	Thrust power	[kW]
Q	Propeller torque	[Nm]
Q_0	Propeller torque signal	[mV/V]

Symbol	Definition	Unit
Q_m	Propeller torque	[Nm]
R	Propeller radius	[m]
r	Radial position on propeller blade	[m]
r_h	Radius of the hub	[m]
$\boldsymbol{R}$	Reynolds stress tensor	$[\frac{N}{m^2}]$
R_{ship}	Ship resistance	[N]
$Re_{0.7}$	Reynolds number at 0.7R	[-]
T	Propeller thrust	[N]
T_0	Propeller thrust signal	[mV/V]
T_m	Measured propeller thrust	[N]
t	Thrust deduction factor	[-]
$\boldsymbol{u}$	Velocity vector	[m/s]
U_x	Uncertainty of variable x	[-]
U_τ	Friction velocity	[m/s]
V	Inflow/Free-stream velocity	[m/s]
V_A	Advance velocity	[m/s]
V_R	Inflow velocity at rudder	[m/s]
V_S	Ship speed	[m/s]
V_{rel}	Relative inflow velocity	[m/s]
V_{rot}	Rotational velocity	[m/s]
w	Wake fraction	[-]
y^+	Wall distance	[-]
Z	Number of blades	$[\#]$
α	Propeller angle of attack	[deg]
α_0	Rudder angle for zero lift	[deg]
α_e	Effective rudder angle	[deg]
α_R	Rudder angle of attack	[deg]
β	Drift angle	[deg]
β_m	Drift angle of the model	[deg]
β_p	Hydrodynamic pitch angle	[deg]
γ	Flow straightening factor	[-]
δ	Rudder angle	[deg]
ϵ	Turbulent dissipation rate	$[\frac{m^2}{s^3}]$
η_0	Open water efficiency	[-]
Θ	Pitch angle	[deg]
θ	Position of propeller blade	[deg]
θ_m	Pitch angle of the model	deg
ν	Kinematic viscosity	$[m^2/s]$
ρ_w	Density of water	[kg/m^3]
σ_x	Standard deviation of variable x	[-]
$\overline{\boldsymbol{\tau}}$	Averaged stress tensor	$[\frac{N}{m^2}]$
τ_w	Wall shear stress	$[\frac{N}{m^2}]$
ϕ_m	Roll angle of the model	[deg]
ω	Rotational speed	[rad/s]

1

Introduction

The shipping industry is facing new challenges, as green house gas emissions must be reduced significantly. In 2021, maritime transport was responsible for 3-4% of the total CO_2 emissions in the European Union ("Reducing emissions from the shipping sector" (n.d.)). Globally, the share was similar, as 2.9% of the total emissions were caused by the shipping industry in 2018. To address this, regulations to reduce the amount of these green house gases are introduced by the International Maritime Organization (IMO). In 2030, ships should emit 40% less CO_2 compared to 2008 levels(IMO (2023)).

Achieving this requires reduction of CO_2 emissions of both new-build as already existing ships. Therefore, alternative ways to sail a ship are considered. One of these methods is using wind to generate the energy that is needed to propel a ship instead of burning fossil fuels. Wind Assisted Ship Propulsion (WASP) converts wind energy into a lift force to reduce the energy needed to generate this force with a propeller. Examples of WASP technologies include Flettner rotors, Dynaring, wing sails and kites (Eggers (2019), Werner et al. (2023)).

Studies have shown the potential of WASP: Tillig and Ringsberg (2020) reported fuel savings for a tanker on the Pacific Ocean can become greater than 30%, whilst 14% reduction for a RoRo ship in the Baltic Sea was obtained. These savings were based on different routes and weather conditions.
However, the effectiveness of WASP is highly depended on wind speed and direction. Olsson et al. (2020) showed the probabilities of facing certain combinations of wind speed and direction on a transatlantic route. Using a Monte Carlo simulation, the average time to travel from Europe to America has been calculated. They found that the difference between the average and median of the data obtained is seven days, underlining the influence of the weather conditions. The effects of depowering was also investigated in their research. This is because WASP can also introduce heel angles, which may exceed the limits of comfort for the crew. The influence of depowering was found to be less significant than the influence of the wind itself.
As stated in Giovannetti et al. (2020), the ship operates mostly in motor-sailing mode, where both the propeller as the WASP system provide thrust. The combination of both sails and propeller gives the best overall efficiency in the range of all wind directions.

As WASP cannot fully power the ship all time, a propeller is still necessary for these ships. However, the operating conditions of ships equipped with WASP technology differ from traditional working points of a propeller. WASP thus alters the flow in the stern region of the ship, where the propeller and rudder are located. Ship propellers are normally designed to deliver the highest thrust in combination with the lowest torque, to obtain the optimal efficiency of the propeller. However, WASP introduces variable loading during operation, as the thrust power delivered by the WASP system is weather dependent (Gypa et al. (2023)). In this research the total fuel consumption was found to be the lowest when the propeller was designed for the highest expected loading.

Furthermore, WASP systems introduce side forces and yaw moments on the ship (Thies and Ringsberg (2023)). These side forces clearly alter the ship's hydrodynamics. Firstly, the ship's resistance increases, due to the increased frontal area. The influence of a drift angle on side forces and yaw mo-

ments were measured both experimentally and numerically by Struijk (2015). These measurements also showed an increase for these forces and moments for increasing drift angles. The propeller's performance is also affected by the oblique flow conditions.

Research studies specifically focussing on propellers operating in combination with WASP are not found. However, some work is done on propellers operating in oblique flow, for example by Dubbioso et al. (2013). However, this research is mainly focused on manoeuvring applications, where drift angles are significantly larger and the time in this operational condition is shorter than those encountered by WASP ships.

The main objective of this thesis is to experimentally investigate the influence of oblique flow conditions in an open-water set-up. Tests are conducted in the large towing tank at the Faculty of Mechanical Engineering at the TU Delft. The focus is on the thrust and torque generated by the propeller under these oblique flow conditions. The results of the tests will be presented to describe the influence of small drift angles on the propeller in open water. Additionally, numerical simulations are performed to compare the experimental results and get insight in the wake of the propeller in these conditions. The research question for this study is as follows:

What are the effects on thrust and torque generated by a marine propeller model, measured experimentally in an open-water environment, under oblique flow conditions and varying loading conditions, imitating typical WASP conditions?

To answer this research question, four sub-questions are formulated:

1. Which effects of oblique flow and advance coefficient on propeller performance and wake characteristics of a propeller are already found in previous studies?
2. Which specific experimental set-up can be used for accurately determining the thrust and torque under oblique flow and varying loading conditions?
3. How does a wing profile upstream the propeller influence the performance of the propeller in oblique flow compared to open water conditions?
4. What are the effects on the wake characteristics of the propeller model and the propeller loading as a function of the rotation angle under oblique inflow and varying loading conditions determined using numerical simulations?

The report is structured as follows. Chapter 2 provides background theory on propellers, covering propeller geometry, propeller performance, interaction with a ship hull and guidelines for open-water tests. Furthermore, some basic rudder theory is included. Chapter 3 reviews findings of research done on the effects on propellers operating at drift angles, including the effects on the wake and velocity field around the propeller and the forces and moments generated in these conditions. Also a short section is spend on propeller rudder interaction. Chapter 3 covers sub-question 1.

Chapter 4 describes the methodology of the experiment, such as the experimental set-up and the parameters used, answering the second sub-question. In Chapter 5, the results of the experiments are presented, showing the mean and uncertainties for thrust and torque, and analysing the frequencies of the signal. This chapter answers sub-question 3 and the research question. Chapter 6 includes the numerical simulations. Both the set-up as the results are presented. In this chapter, sub-question 4 is addressed. Finally, in Chapter 7 some conclusions are drawn and some suggestions for future research are given.

2

Fundamental background

This chapter describes fundamental background of propellers and rudders. The first section covers the working principles of propellers operating under conventional conditions. In the second section, general rudder theory is presented.

2.1. Propeller

Propellers described in this section are operating in straight inflow. The aim of this section is to describe geometry of a propeller, and give definitions for the performance. The implications of a ship upstream are also discussed and the generation of thrust and torque is explained conceptually using blade element theory. Finally, some guidelines for experimental measurements are provided.

2.1.1. Propeller geometry

Propellers generate the ship's thrust force by accelerating or decelerating the surrounding water. Most ship propellers consist of three to five propeller blades attached to a hub, as shown in Figure 2.1.

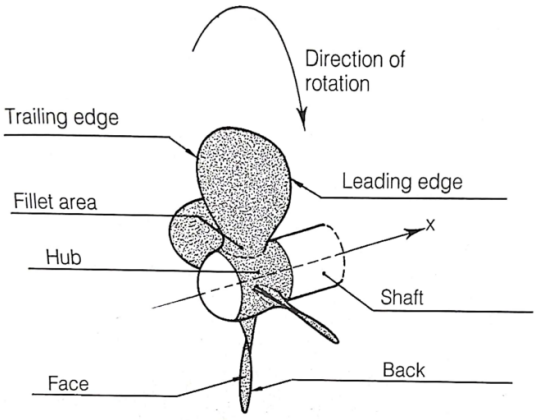

Figure 2.1: Propeller geometry (Woud and Stapersma (2002))

The propeller hub is connected to a shaft, which transfers rotational energy of the shaft to the propeller. The leading edge is the side of the propeller that passes first at a given location, while the trailing edge logically follows. The face of a propeller blade is seen when looking at the propeller from behind the ship, while the back faces towards the ship. The face of the propeller is also called the pressure side, and the back of the propeller is called the suction side (Woud and Stapersma (2002)).
Propellers have various geometry parameters that can be adjusted to achieve the highest efficiency under certain design conditions. These are summarized below.

Blade profile
The blade profile is the cross-sectional shape of the propeller blade. Most propellers have a blade profile which looks similar to standard aerofoil sections (Carlton (2007)). An example of an aerofoil section is shown in Figure 2.2a.

A blade section represents one single radial position on the propeller blade and changes along the propeller radius. The leading and trailing edge define the direction of rotation. The chord line of an aerofoil section is the straight line between the leading and trailing edge. The chord length c of the section is the length of the chord line. The camber line is defined as the line trough the midpoints of the perpendicular lines between the camber line and the upper and lower sides of the section (Carlton (2007)).

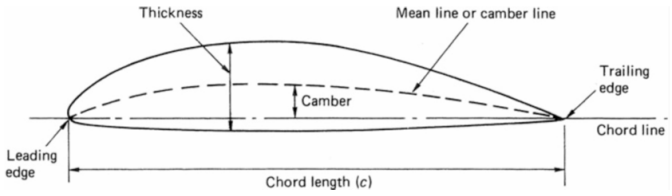

(a) Standard aerofoil section (Carlton (2007))

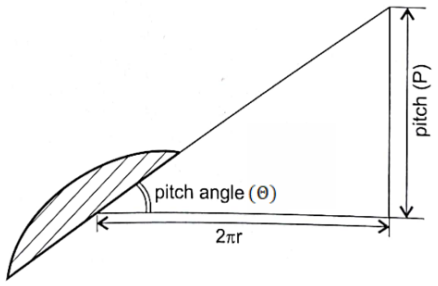

(b) Pitch of a propeller without slip (Adapted fromWoud and Stapersma (2002))

Figure 2.2: Pitch definitions (Adapted from Woud and Stapersma (2002) and Carlton (2007))

Pitch
The pitch of a propeller is defined as the distance P that a propeller advances during one rotation in the absence of slip (Woud and Stapersma (2002)). This is shown in Figure 2.2b.

As shown in this Figure, the distance that a propeller travels during one rotation is equal to $2\pi r$. Here r is the radial position of this blade section, in other words, the distance between this section of the propeller blade and the propeller hub.

$$\Theta = \tan^{-1}\left(\frac{P}{2\pi r}\right) \tag{2.1}$$

According to Carlton (2007), several different definitions exist for the pitch angle. The nose-tail pitch line, which is the line from leading edge to trailing edge is the most commonly used convention (Carlton (2007)) and therefore this will also be used in this report. Another relevant pitch definition mentioned is the hydrodynamic pitch angle β_p. This is the angle at which the flow actually encounters the propeller blade, which directly influences thrust and torque.

Blade Area Ratio
The blade area ratio is the ratio that indicates which percentage of the propeller disk is covered by the propeller. This is important for both the efficiency of the propeller and cavitation performance. In Figure 2.3a, the expanded outline for a Wageningen B4-series propeller is shown, with different blade area ratios. A higher blade area ratio will likely reduce the efficiency of the propeller. This is caused by frictional losses that increase as the propeller surface increases. However, the cavitation performance of the propeller improves. This is caused by the fact that the total thrust delivered by the propeller remains the same. When the propeller blades cover a higher area, the thrust loading on each propeller decreases, reducing the probability of cavitation.

Skew and Rake
Skew and rake also have an impact on the efficiency and cavitation performance of the propeller. Skew is the bending of the mid-chord line of the propeller blade. The skew angle is the angle between the most outer positions of the midline, as shown in Figure 2.3b. Skew is applied to flatten the pressure pulses

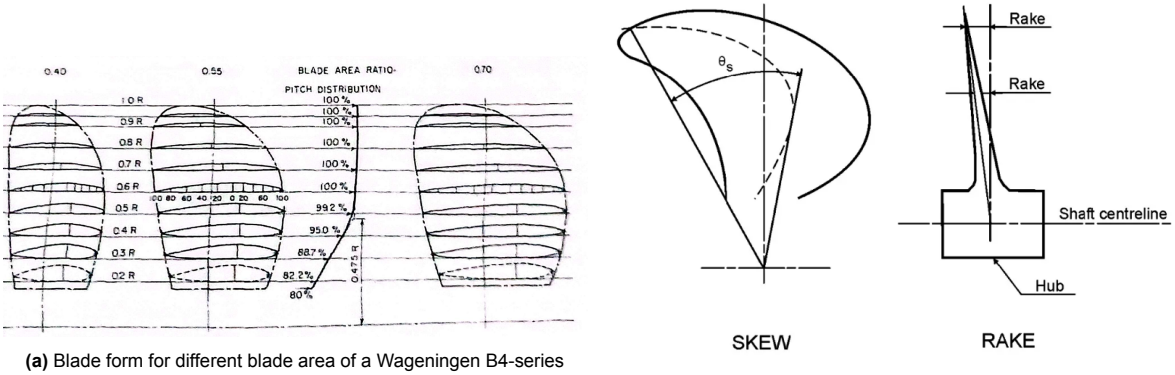

(a) Blade form for different blade area of a Wageningen B4-series (Kerwin et al. (2010))

(b) Skew and rake of a propeller ("Propeller, screw propeller" (n.d.))

Figure 2.3: Blade Area, skew and rake of a propeller (Kerwin et al. (2010) and "Propeller, screw propeller" (n.d.))

as a result of the passing propeller blades. This is beneficial for the propeller's cavitation performance, as high pressure fluctuations can also cause too low pressure resulting in cavitation. The tip rake is the angle of the propeller blades with respect to the hub in the x-z-plane. Tip rake does have a slightly negative influence on propeller efficiency. However, its influence on cavitation is positive as the distance between the hull and the propeller tip increases. This increased tip clearance reduces the chance of cavitation when the tip passes close to the hull. The tip rake also increases slightly by the angle of skew (Carlton (2007)). This is caused by the helix structure of the propeller blades. This means that skew and rake are connected to each other and should be considered together when applying it to a propeller.

2.1.2. Propeller performance

The performance of the propeller is important both for comparing propellers and matching them to a ship with a given operational profile. Therefore some non-dimensional numbers are introduced. Firstly, the advance coefficient gives the relation between the axial inflow velocity (advance velocity V_A in m/s) and the circumferential velocity, which is the propeller rotational velocity n_p in rps times the propeller diameter D_p in meters, as shown in formula 2.2.

$$J = \frac{V_A}{n_p D_p} \tag{2.2}$$

The propeller generates forces and moments. The thrust T is the resulting force in the ship moving direction (in N). The torque Q is the moment generated by the propeller (in Nm). Both can be non-dimensionalised by the density of water ρ_w, the propeller rotational speed n_p and the propeller diameter D_p, as shown in equations 2.3 and 2.4.

$$K_T = \frac{T}{\rho_w n_p^2 D_p^4} \tag{2.3}$$

$$K_Q = \frac{Q}{\rho_w n_p^2 D_p^5} \tag{2.4}$$

According to an analysis of the non-dimensional groups in Carlton (2007), both K_T and K_Q can be written as a function of the advance coefficient J, the Reynolds number Re and the cavitation number σ_0. Approaching the free surface, the Froude number (gravity effects) and Weber number (surface tension) also become important.

As the thrust and torque for the propeller are known, the open-water efficiency of the propeller can be determined using equation 2.5.

$$\eta_0 = \frac{1}{2\pi}\frac{K_T J}{K_Q} \tag{2.5}$$

This formula follows from equation 2.6 Kerwin et al. (2010), where P_T is thrust power and P_D is delivered power to the propeller.

$$\eta_0 = \frac{P_T}{P_O} = \frac{TV_A}{2\pi n_p Q} \tag{2.6}$$

The values of K_T, K_Q and η_0 for a propeller can be obtained experimentally by open-water tests. For the Wageningen B-series, a variety of open-water tests are performed and published. As an example, the open-water diagram for a Wageningen B4-40 propeller is shown in Figure 2.4.

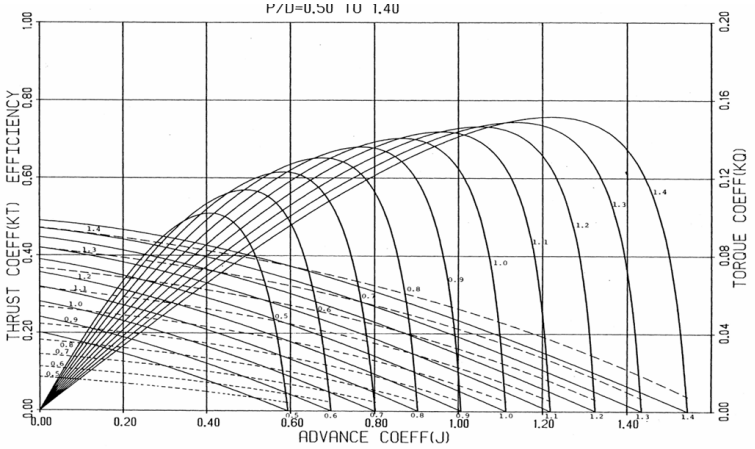

Figure 2.4: Open-water diagram of a Wageningen B4-40 propeller (Bernitsas et al. (1981))

Open-water diagrams are useful in propeller design. To match a propeller to the ship's demand, it should overcome the resistance and the added resistance due to its velocity. In a design condition, it is possible to optimise for the propeller diameter or rotational speed of the propeller (Woud and Stapersma (2002)). To optimise for the rotational speed, the maximum propeller diameter is used. Then it is possible to calculate the $\frac{K_T}{J^2}$ characteristic of a ship. The intersection of the line $\frac{K_T}{J^2} \cdot J^2$ gives the optimal advance coefficient. The same procedure can be performed to optimise the diameter of the propeller, but then $\frac{K_T}{J^4}$ is needed.

The parameters introduced earlier affect the magnitude of K_T, K_Q and η_0. For example, an increase in thrust and torque is observed for increasing pitch, while higher blade area ratio would also increase forces, but lower effciency

2.1.3. Hull-propeller interaction

Most propellers are placed in the stern region of the ship. The propeller encounters therefore a turbulent flow, as the flow around a full-scale ship is turbulent. The flow entering the propeller plane in non-uniformly distributed over the propeller disk. The wake profile shows the velocity on each circumferential and radial position in the plane. According Carlton (2007), there are three main causes for a wake field behind the ship. These are the fact that the flow needs to go around the hull, the boundary layer at the hull and, if free-surface is important, the impact of wave-making.

Rijpkema et al. (2013) shows the difference between different numerical methods to determine the wake field of a hull and propeller. In Figure 2.5 the nominal wake field is shown for a container ship. Note that starboard and port side of the propeller plane differ, as two different methods are compared: free-surface effects are accounted for on the port side.

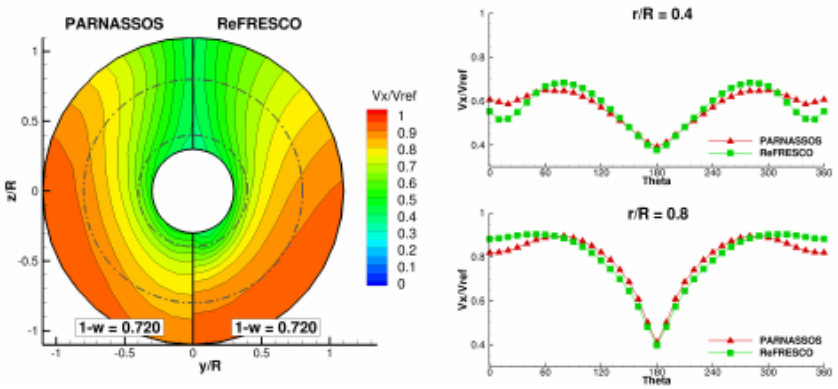

Figure 2.5: Axial velocity behind a container ship (Rijpkema et al. (2013))

Besides some differences between both sides, the general properties of the container ship's wake field are shown well. Firstly, a peak in the top section of the plane is observed. In this region the flow is decelerated compared to the free stream flow. This is caused by the particles that are within the boundary layer and close to the hull, where the velocity is lower. These particles stay close to the hull and therefore flow into the top part of the propeller disk. Secondly, it can be seen that the axial velocity in the lower part of the plane is almost equal to the free-stream velocity. On the right-hand side of Figure 2.5, it can also be seen that the axial inflow velocity at a radial position closer to the hub is changing less during a revolution than radial positions closer to the tip. In Figure 2.5, it is shown that the wake fraction for both methods is the same. As already shown in equation 2.9, the wake fraction w is relating the ship speed V_s to the advance speed V_A at the propeller. The wake fraction can be determined from the inflow information at each position in the propeller plane using equation 2.7.

$$1 - w = \frac{\int_{r_h}^{R} \left(\frac{V_A}{V_s}\right) r dr}{\int_{r_h}^{R} r dr} \tag{2.7}$$

For U-shaped, such as an container ship, the region of the wake peak is much wider than for smaller V-shaped vessels. Moreover the influence of a bilge vortex can be observed for U-shaped vessels (Carlton (2007)). As the curvature of these ships change fast over a small distance at the bilge, the flow is not able to follow the ship hull. Therefore, the boundary layer will separate from the hull, and different particles will flow in the gap left by the separated flow.

Also, the transverse velocity components are affected by the presence of the ship. As already described, the flow follows the hull. Approaching the propeller, the contour of the hull in moving upwards, causing the flow also to move upward. This change in direction causes a difference in propeller loading as one side of the propeller is moving against the transverse velocity, increasing its loading, whilst the other is loaded less, as it is rotating in the same direction as the transverse flow velocity.

Two wake field types can be distinguished: nominal wake and effective wake. Nominal wake is the field that is observed when the flow is passing the hull, without the presence of a propeller rotating behind it. This profile only forms due to the presence of the ship. When a propeller is operating behind the ship, the wake field will look different as the propeller is. Here is an influence of the propeller induced velocities and the vorticity interaction (Rijpkema et al. (2013)).

The effective wake does differ from the nominal wake. This is caused by the fact that the flow is accelerating approaching the propeller, when the propeller is rotating. The leads to a wake peak that is smaller compared to the nominal wake. According Rijpkema et al. (2013), radial positions close to the hub are mostly affected by interaction effects. There, the axial velocity of the effective wake is varying less during a revolution than for the nominal wake.

The interaction between the ship hull and the propeller does not only influence the inflow velocity, and therefore the forces on the propeller blade. It is also affecting the resistance of the ship. The relation

between propeller thrust and ship resistance is called the thrust deduction factor t, as shown in equation 2.8.

$$t = \frac{T - R_{ship}}{T} \tag{2.8}$$

As Reynolds numbers for full-scale ships are typically high, the flow around the hull is turbulent. In terms of turbulence, there are two types of wake that can be distinguished: plane wake and axisymmetrical wake (Pope (2000)). The plane wake is the wake that is caused by a flow around a cylinder. This is a two-dimensional flow that is symmetrical around the y-axis. For such flows, the velocity deficit function can be plotted against the y-coordinate. In Figure 2.6, the normalised velocity defect for a plane wake is shown. On the x-axis, the normalized y-coordinate ξ is given, while the y-axis presents the normalized velocity deficit $f(\xi)$.

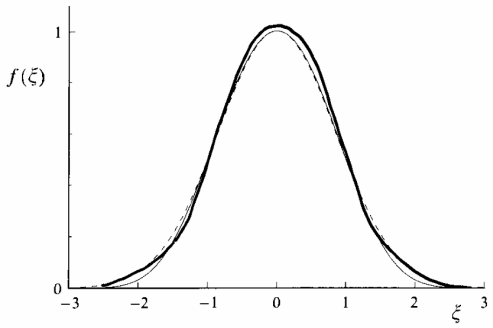

Figure 2.6: Normalised velocity defect in a plane wake (Pope (2000))

Just as in the wake-profile described before, the largest velocity defect can be observed at the location right after the object it flows around. Also at the ends the velocity defect function is approaching 0, meaning that the free-stream velocity is again dominant in this region. The axisymmetrical wake is caused by the flow around a sphere or other round object, which looks very similar to the plane wake. However, this flow is a 3D-flow, which is dependent on radial and x-position. The wake of a ship is a combination of plane and axisymmetrical wake.

2.1.4. Propeller inflow vectors

Generation of thrust is the result of accelerating water. The inflow to the propeller influences this thrust force, as the angle of attack changes when the magnitude and direction of the inflow velocity changes. There are several methods to determine the magnitude of the thrust and torque without performing experiments or simulations. The Blade Element Theory of William Froude (Carlton (2007)) is such a model. This theory explains thrust generation by the velocities acting on a propeller blade, as shown in Figure 2.7.

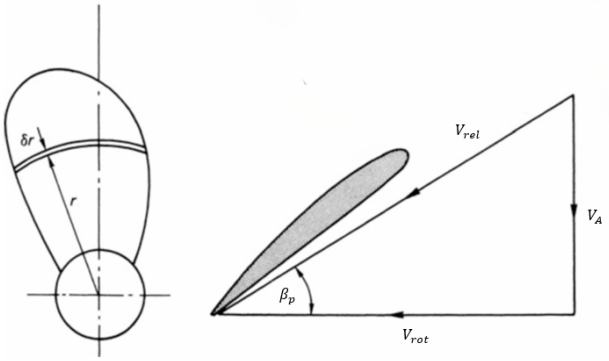

Figure 2.7: Blade element theory (Adapted from Carlton (2007))

In this theory, a blade section is analysed at a certain radial location. The velocity acting on the propeller blade section can be decomposed in two velocities. The advance velocity V_A, which is the inflow velocity due to the speed of the ship, and the rotational or circumferential velocity, which is the velocity due to the fact that the propeller is rotating. These velocities can be calculated using formulas 2.9 and 2.10.

$$V_A = (1 - w) \cdot V_s \tag{2.9}$$

$$V_{rot} = \omega r = (2\pi n_p) r \tag{2.10}$$

Note that formula 2.9 is a simplified version of formula 2.7. Here V_A is the advance velocity in m/s, w is the wake fraction, V_s is the ship speed in m/s. In equation 2.10, V_{rot} is the circumferential velocity in m/s, ω is the rotational speed of the propeller in rad/s, r the radial position of the blade section and n_p the rotational speed of the propeller in 1/s. These velocities are perpendicular to each other and therefore, the relative inflow velocity can simply be determined using equation 2.11.

$$V_{rel} = \sqrt{V_A^2 + V_{rot}^2} \tag{2.11}$$

V_{rel} is the relative inflow velocity in m/s. Besides these two velocities, there is also the induced velocity due to the propeller's rotation. This velocity is left out in this representation. This slightly changes the relative inflow to the propeller blade, but the method as described above can still be used for first approximations of the propeller forces.

For the blade section considered, the velocities are known. The angle of attack can be derived from the angles formed by these velocities. Firstly, the hydrodynamic pitch angle β_p needs to be calculated. This angle is defined by the direction and magnitude of the inflow and circumferential velocity vectors. Using the tangent, as in equation 2.12, it is possible to find the hydrodynamic pitch angle, which is the angle that the relative velocity encounters the blade section, as shown in Figure 2.8b.

$$\beta_p = \tan^{-1}\left(\frac{V_a}{V_{rot}}\right) \tag{2.12}$$

As the local pitch angle Θ is also known, see formula 2.1, it is possible to find the angle of attack. The angle of attack is introduced by slip. Slip is the phenomenon that the propeller blade does not advance the maximum distance (Woud and Stapersma (2002)) that it theoretically could advance, as shown in Figure 2.8a. The angle of attack α is the difference between the pitch angle and the advance angle, as in formula 2.13.

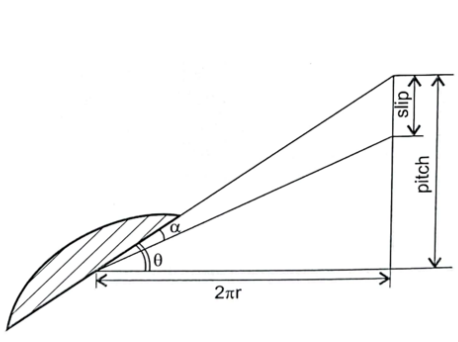

(a) Definition of slip and angle of attack (Woud and Stapersma (2002))

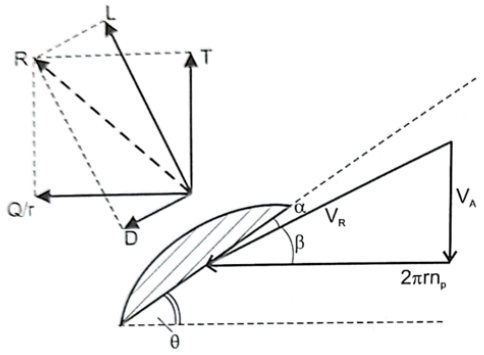

(b) Angle of attack (Woud and Stapersma (2002))

Figure 2.8: Definition of angles using velocities

$$\alpha = \Theta - \beta_p \tag{2.13}$$

The angle of attack influences the lift generated by the blade section. This can be seen in Figure 2.10, as the propeller can have a similar profile as a ship rudder. The figure shows that for small angles of attack an increase in angle of attack leads to an increase for the generated lift force. More lift, and thus also more thrust, leads to a higher loading of the propeller blade. In Figure 2.8b, it can be seen that an increase in rotational speed, leads to an higher angle of attack. Also a decrease in inflow velocity results in higher propeller blade loading, due to the increase in angle of attack. This means that for those conditions the thrust generated by that particular blade section is also increased. As the propeller blade is rotating, the inflow velocities are directed differently on each propeller blade position. In this report the blade position θ, in degrees, is as follows. $\theta = 0°$ is at the top of the propeller, whilst the starboard side is $\theta = 90°$. This lead to the lowest position at $\theta = 180°$ and $\theta = 270°$ at the port side.

2.1.5. Open water test methods

To obtain open water diagrams as in Figure 2.4, the thrust and torque generated by a propeller must be measured. Experimentally, this can be done in either a towing tank test or a test in the cavitation tunnel. Experiments are important to characterise the model of the propeller. Also for ship models, characteristics of the ship in terms of resistance, sea-keeping behaviour and manoeuvring capabilities can be measured experimentally. According to Tupper (2013), experiments can contribute to fuel savings of 3 to 5%, by optimising hull form. The propeller performance can also be optimised by comparing experimental test results. Nowadays, numerical methods such as CFD become more important and can be used to compare the experimental results. Both the towing tank test and the test in a cavitation tunnel will be described shortly.

Towing tank

In a towing tank, the propeller can be pulled through the water to obtain thrust and torque coefficients. The conventional set-up for an open water test in a towing tank of International Towing Tank Conference (2021) is shown in Figure 2.9.

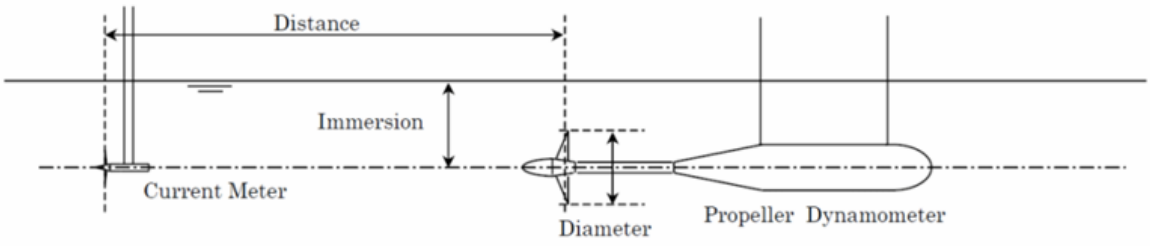

Figure 2.9: Typical open water test set up (International Towing Tank Conference (2021))

International Towing Tank Conference (2021) describe some important parameters and conditions that should be achieved when performing the test. Firstly the immersion of the propeller shaft line should be at least 1.5 times the propeller diameter D, to avoid free surface influences. Also, the dimensions of the towing tank should be large enough to avoid influences of the wall and guarantee a uniform inflow. Parameters that must be measured during open-water test are thrust, torque, rate of revolutions, speed of the propeller, and temperature of the water. ITTC gives some boundaries for the required accuracy of the measurement instrument, such that measurements are accurate enough. Calibration before performing the test is of great importance to comply to this accuracy, as the instruments could provide results that are all shifted compared to the real results. As the model scale propeller is operating in a flow that has a lower velocity and lower rotational speed than full-scale, the Reynolds number will be significantly lower. International Towing Tank Conference (2021) defined the Reynolds number based on the chord length at $\frac{r}{R} = 0.7$ ($c_{0.7}$), as shown in equation 2.14.

$$Re_{0.7} = \frac{c_{0.7}\sqrt{V_A^2 + (0.7\pi n_p D_p)^2}}{\nu} \tag{2.14}$$

Here $Re_{0.7}$ is the Reynolds number for the chord length at 0.7R and ν is the kinematic viscosity in m^2/s. Preferably, the Reynolds number should be as high as possible to avoid scaling problems from laminar to turbulent flows.
Heinke et al. (2019) did open-water tests for different Reynolds numbers to find the influence of the Reynolds number on thrust and torque coefficient. The lowest Reynolds numbers considered is $Re_{0.7} = 2.0 \cdot 10^5$, as the flow is probably laminar in this flow. It was found that K_T and K_Q are increasing between $Re_{0.7} = 1.5 \cdot 10^5$ and $Re_{0.7} = 3.0 \cdot 10^5$. In this region, thrust increases the most, so open-water efficiency increases. For $Re_{0.7} > 5.0 \cdot 10^5$, the open-water efficiency is still increasing, while K_T remains constant for these Reynolds numbers. This was declared by the linear decrease of K_Q.

Cavitation tunnel
In a cavitation tunnel the inflow parameters can be controlled, as the water follows a closed loop. Therefore, it is possible to simulate conditions that are closer to full-scale conditions than for tests in a towing tank. However, it should be noted that the propeller cavitation should be minimised as much as possible, as this will influence the measured open-water characteristics. One of the main requirements for open-water tests is that the test should be performed at atmospheric pressure. The selection of the propeller diameter is important in a cavitation tunnel as the dimensions of the tunnel are significantly smaller than that for the towing tank. Therefore, the diameter should be selected such that scaling effects are not important, while avoiding interaction with the walls of the tunnel (International Towing Tank Conference (2021)).

2.2. Rudders

Rudders are applied to a ship to change the course of a ship or to compensate for deviations due to current or waves for example. In this section rudders will be explained shortly. Firstly, some profiles and types will be mentioned. In the second subsection the lift and drag forces acting on a rudder will be explained.

2.2.1. Rudder profiles and types

In the literature review on ship rudders of Liu and Hekkenberg (2017), seven profiles are distinguished. One of the simplest profile is the flat plate. It was found that this profile can have high efficiency for small rudder angles. However, stalling starts to occur at smaller angles, since the flow separates earlier with this profile. The most applied rudder profile is the NACA profile. These profiles were initially designed for aerodynamics applications, but can also be used for hydrodynamics when the Mach number is low.

Research is done to optimise the efficiency of the ship rudder. The HSVA requires a lower rudder area for the same performance, resulting in a lower fuel consumption. The IFS profile is designed to have an as high as possible lift coefficient for a large stall angle.
There are also rudder profiles with a tail or flap at the trailing edge of the profile. These are the Fishtail, Wedge tail and flapped rudder. These rudders have additional area at the trailing edge to generate more lift. This type of rudder is designed to perform better during manoeuvring operations. However, as stated by Liu and Hekkenberg (2017), the extra lift generated does have the disadvantage of inducing extra drag, and thus lower the rudders efficiency.

Molland and Turnock (2007) distinguishes some rudder types. The balanced rudder is a rudder in which the rudder area before and after the stock is balanced. In other words, the forces acting on both part are balanced, reducing the required size of the steering gear. An example of a balanced rudder is the spade rudder. This rudder is longer at the top than at the bottom, which is frequently used on single and twin-screwed ships (Molland and Turnock (2007)). For unbalanced rudders the stock is in front of the rudder. There are also rudders that are fully or partially connected to the skeg, instead of connections with a pintle on the top and bottom. This is done to improve the connection to the ship and allow for higher rudder areas, needed on big seagoing vessels. However, the manoeuvring performance of these rudders is worse than for rudders connected to pintles (Liu and Hekkenberg (2017)).

2.2.2. Forces on an aerofoil profile

The forces on a rudder can be determined in the same way as forces on an aerofoil profile, following the rudder profiles in subsection 2.2.1. As shown in Figure 2.8b, the lift is the force that is perpendicular to the inflow on the foil. The drag is the force in the stream-wise direction, perpendicular to the lift force.

For NACA-profiles, data is mostly presented as a non-dimensional number. Equations 2.15 and 2.16 show how lift and drag can be calculated using these non-dimensional coefficients.

$$L = \frac{1}{2} C_L \rho_w V_R^2 A_R \tag{2.15}$$

$$D = \frac{1}{2} C_D \rho_w V_R^2 A_R \tag{2.16}$$

Here, C_L is the lift coefficient, C_D the drag coefficient, ρ_w the density of water in kg/m^3, V_R the inflow velocity at the rudder in m/s and A_R the rudder area in m^2. Kramer et al. (2016) simulated the lift and drag on a spade rudder, with a NACA 0018 profile. The results are shown in Figure 2.10.

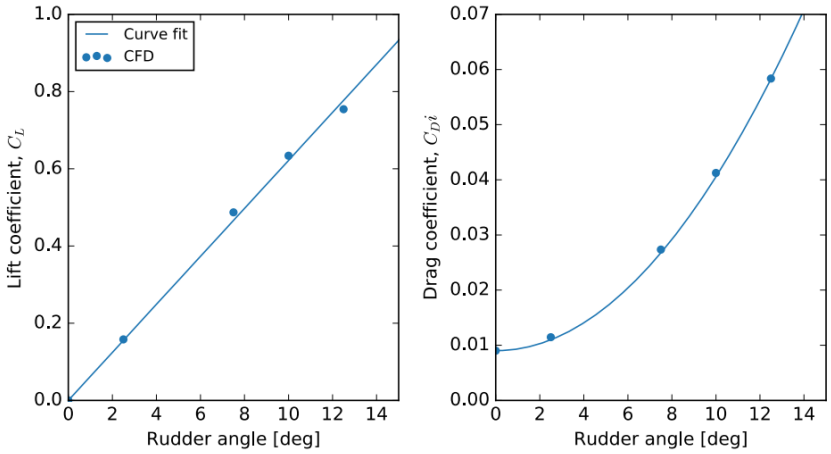

Figure 2.10: Lift coefficient and drag coefficient for a rudder (Kramer et al. (2016))

It can be found that the lift coefficient is increasing almost linear with the rudder angle. For the drag coefficient, a second order relation can be found. According to Liu and Hekkenberg (2017), these trends are observed when analysing any foil shaped rudder. However, these trends stop at the stall angle. This is the rudder angle where maximum lift is achieved. The lift coefficient will drop when increasing the rudder angle after the stall angle.

Liu and Hekkenberg (2017) also describe how the forces on a rudder are dependent on both the Reynolds number as the angle of attack. Firstly, also for rudders, the Reynolds number does influence the lift and drag coefficients. According to Liu and Hekkenberg (2017) the lift coefficient increases for increasing Re, while the drag coefficient is even more sensitive to fluctuations of the Reynolds number. To have the dynamic similar rudders in both model test as full-scale experiments, the Reynolds number should be as high as possible. This is because the flow is turbulent for higher Reynolds numbers and laminar for lower Reynolds numbers. Above a Reynolds number of about $3 \cdot 10^6$ the influence of Re on the lift and drag coefficient reduces.

Lift and drag coefficients are also a function of the angle of attack. However, when operating under drift, the angle of attack of the rudder is also affected as shown in formula 2.17 (Liu and Hekkenberg (2017)).

$$\alpha_R = \delta - \beta \tag{2.17}$$

Here α_R is the angle of attack of the rudder, δ the rudder angle, and β the drift angle. Liu and Hekkenberg (2017) found that for inland vessels, the most commonly applied rudder angles were between 15 and -15 degrees. Moreover, it was observed that higher rudder angles were used at a much lower speed, corresponding to manoeuvring operations, which will be one of the main research fields considered in chapter 3.

3

Propeller at a drift angle

In Chapter 2, propellers and rudders in straight inflow were introduced. For WASP, the ship and propeller are at a small drift angle, whilst the propeller loading depends on power generated by wind. This influences efficiency of the propeller, since it is not operating in one single design condition. The aim of this chapter is to answer the first sub-question:

Which effects of oblique flow and advance coefficient on propeller performance and wake characteristics of a propeller are already found in previous studies?

Focus in this research field is on manoeuvring, which also meets the conditions formulated in the sub-question. In this chapter the propeller at a drift angle will be analysed. In the first section, the wake of the propeller operating in oblique flow will be studied. The forces and moments acting on and generated by the propeller in oblique flow are explained in section 2. In the last section, propeller-rudder interaction under a drift angle is shortly discussed.

3.1. Oblique flow

Oblique flow alters the load on propeller blades. During a revolution, the incoming flow is at a different angle with respect the blade. For propellers in straight inflow, the angle between incoming velocity and circumferential velocity of the blade is constant. Even in open-water conditions, this is changed by drift angles. The inflow or advance velocity V_A is under an angle and changes the inflow to the propeller. Consequently, the angle of attack is not constant during a propeller revolution. In Figure 3.1, the influence of a drift angle β on the velocity vectors is shown.

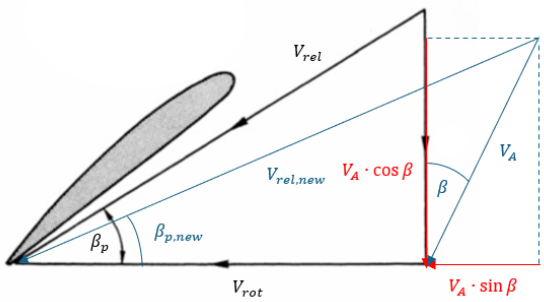

Figure 3.1: Velocity vectors with the influence of a positive drift angle β. Adapted from Carlton (2007)

This figure shows the impact of drift on both advance velocity V_A and circumferential velocity V_{rot}. The decomposed inflow vector shows a decrease in advance velocity and an increase in rotational velocity, due to the contribution of the inflow at drift, which is $V_A \sin(\beta)$. This positive drift angle leads to a new relative velocity $V_{rel,new}$. The hydrodynamic pitch angle has decreased, which increases the angle of

attack. This effect is depended on blade position θ. At an opposite position then described above, the drift angle generate an opposite contribution to V_{rot}. This deceases angle of attack. Figure 3.2 shows the impact of drift on the angle of attack.

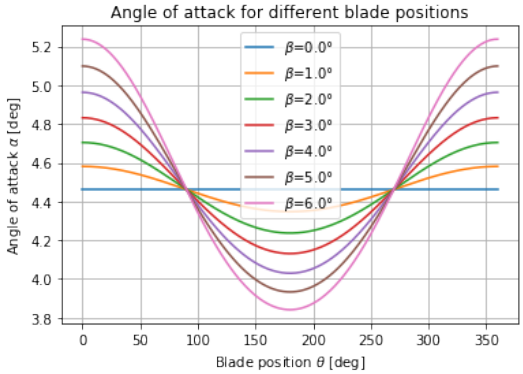

Figure 3.2: Angle of attack as function of the blade position θ for different drift angles β

Figure 3.2 shows the biggest effect of drift on the 0 degrees and 180 degrees position. No influence is observed at $\theta = 90°$ and $\theta = 270°$, because the circumferential velocity is still perpendicular to the inflow vector at this position. The difference between the top and bottom is declared by the opposite contribution to the circumferential velocity in the 180 degrees position, which decreases angle of attack. Therefore, the angle of attack is the smallest in that position. The influence of the drift angle is opposite for negative β_p. Then the maximum angle of attack can be found in the lowest propeller blade position.

This section focus on the wake characteristics of a propeller operating in oblique flow. Oblique flow changes the wake of the propeller itself and the inflow to the propeller, which is even more complex behind a ship hull. These effects and the influence of the advance ratio J on the flow around the propeller are explained.

3.1.1. Influence of oblique flow before the propeller plane

Oblique inflow to the propeller influences the propeller loads. Oblique flow can be encountered for example during manoeuvring, where the propeller is shortly affected by large drift angles. Oblique inflow can also be the result of current or wind, which is the case for WASP ships.

Velocity field

Most propellers are positioned at the centreline behind a ship hull. The inflow to the propeller is also altered by the ship's wake. The influence on the velocity profile behind a ship at drift is shown in Figure 3.3 (Sun et al. (2018)).

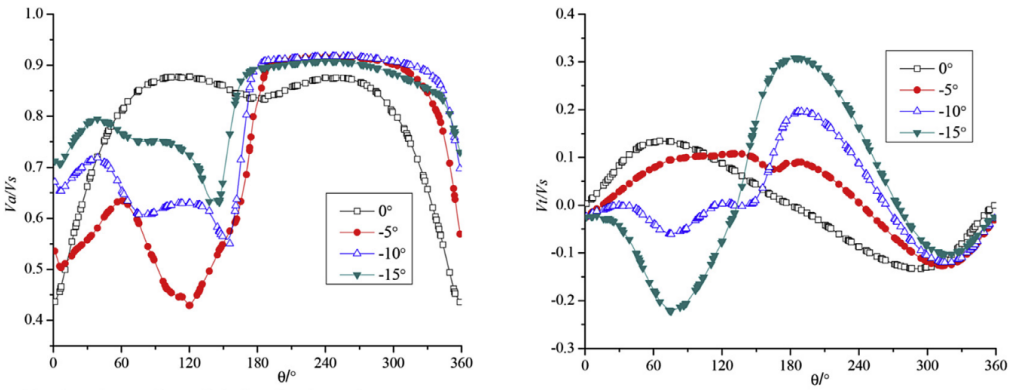

(a) The circumferential distribution of *Va* at 0.7R

(b) The circumferential distribution of *Vt* at 0.7R

Figure 3.3: (a) Axial and (b) tangential velocity for one blade rotation for different drift angles (Sun et al. (2018))

Sun et al. (2018) examined the influence of drift on propeller forces, using RANS and VOF in their simulations. The cause of the varying forces was shown in the velocity profiles in the wake of the ship. The axial and tangential velocity acting on a propeller blade change during a propeller revolution, which combine to the relative inflow velocity. The figures above show the distribution during a rotation for the axial (Figure 3.3a) as well as the tangential velocity (Figure 3.3b) is given for radial position $r = 0.7R$.

The axial inflow is symmetrical for $\beta = 0°$The velocity deficit due to the presence of the ship is visible around $\theta = 0°$. The effect of the negative drift angle becomes visible on the starboard side of the propeller, between $\theta = 0°$ and $\theta = 180°$. The location of the maximum velocity deficit is shifted to starboard for the axial velocity competent. The lowest highest velocity deficit is found for the smallest considered drift angle, which could be an disadvantageous effect for WASP. According to Sun et al. (2018), one of the reasons for the non-uniformity of the velocity profile in this region is fluid separation and vortices from the starboard side of the hull. The port side of the propeller is not affected by those vortices from the hull and its appendages and therefore experiences a uniform oblique inflow, resulting in a slightly higher velocity as the flow is less disturbed by the ship. For the tangential flow component in Figure 3.3b, the drift angle completely changes its distribution. For zero drift angle the maximum and minimum can be found at close to $\theta = 90°$ and $\theta = 270°$ respectively. This is caused by the up-going flow behind the hull, causing opposite influence on the flow between port side and starboard. For increasing drift angle the peaks shift to the starboard and port side of the propeller, and also the amplitude changes. The changes in both velocity components lead to a completely changed angle of attack at each blade position, which cause an asymmetrical distribution of the forces.

Marcu and Robe-Voinea (2024) also visualised the asymmetrical flow around a ship, by performing a numerical study on a high block coefficient ship. It describes the development of the axial velocity before the propeller (at $x = 0.85L_{pp}$ and $x = 0.95L_{pp}$), at the propeller plane and behind the propeller ($x = 1.00L_{pp}$ and $x = 1.10L_{pp}$). The goal of the simulations was to visualise the difference between bare hull simulation and the hull in combination with a propeller with and without drift angle. The bilge vortices are clearly visible in all cases, as the ship used in this research is a tanker. When a drift angle is applied, the strength of the vortex side that is in the ship's wake is amplified. For increasing drift angle, the position where the bilge vortices formate moves forward.

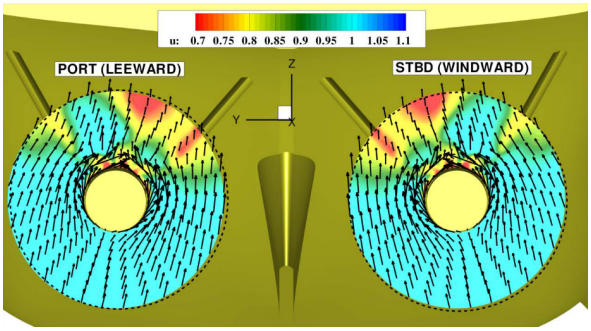

(a) Wake at β=0° for a twin-screwed ship (Ortolani et al. (2018))

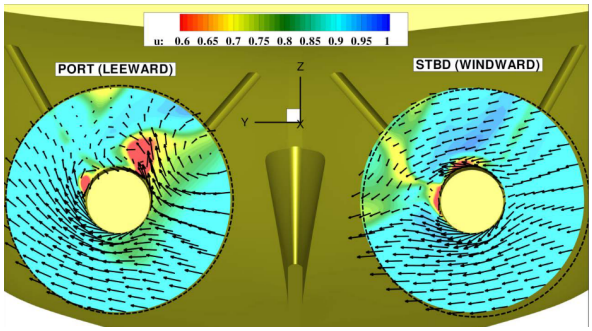

(b) Wake at β=15° for a twin-screwed ship (Ortolani et al. (2018))

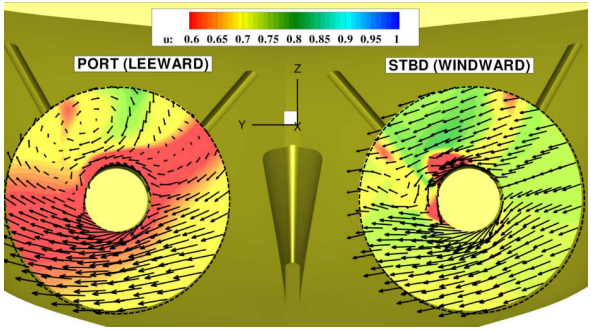

(c) Wake at β=35° for a twin-screwed ship (Ortolani et al. (2018))

Figure 3.4: Wake for a twin-screwed ship at different drift angles

Besides ships with one propeller, a lot of research has been done by a group from the University of Genova and CNR-INSEAN in Rome on a twin-screw ship. For these ships in oblique flow, both propellers experience different inflow. Several experimental (Ortolani and Dubbioso (2019), Ortolani et al. (2020), Ortolani et al. (2018)) and computational (Muscari, Dubbioso, Ortolani, and Di Mascio (2017), Gaggero et al. (2019)) research was done on this ship with two propellers. In Figure 3.4, the axial and tangential components of the velocity for both propellers are given with the colours and arrows respectively.

Other than with a single propeller, the inflow to the propellers differs already in straight ahead condition. This is clearly visible in Figure 3.4a. Both propellers are facing a velocity deficit, due to the ship hull and the brackets of the shaft. This region of lower velocity is however not exactly at 0° , but slightly shifted, since the propellers are positioned off-centre. However, it should be noted that both propellers are rotating in opposite direction, the port propeller is rotating clockwise whilst the starboard propeller is rotating counter clockwise. This means that the propeller blades are facing the low velocity at the same circumferential position.

The main purpose of Ortolani et al. (2018) was to capture the forces on the propellers during manoeuvring. In the paper, the internal propeller during the manoeuvre is referred to as leeward, while the external propeller is referred to as windward. For the relative small drift angle of β=15°, some differences are already visible in Figure 3.4b. Where the tangential component was still directed upwards for β=0°, this is now more sideways. Especially for the windward propeller, the sideways component is dominant. In Figure 3.4c, where β=35°, the propeller is in almost pure oblique flow, according to the authors. This means that the influence of the ship hull and its appendages are almost negligible and the propeller is basically operating as a propeller in open water, but with oblique inflow. On the other hand, the leeward propeller is heavily influenced by the ship hull. For β=15° the velocity deficit is slightly shifted compared to straight ahead, and is a result of the presence of a skeg. The propeller faces swirling flow components for β=35°. Those are caused by the influence of the bilge vortex, which appears in the propeller plane of the leeward propeller due to the drift angle. Moreover, this vortex is interacting with other appendages, in this case the brackets and the skeg, resulting a more non-uniform inflow. There are also ships that have even more propellers. Sun et al. (2023) showed how the inflow field of a four screwed propeller looks. This case is in principle similar to the twin-screw ship. The main difference is that there is two propellers on each side, which are essentially a leeward and windward propeller compared to each other. In straight ahead condition, the outer propellers are less influenced by the ship. At a drift angle, the inflow of the outer propeller is dependent on which side it is, as for the twin screwed ship. However, the biggest difference is showing up at large drift angles. Here, the vortices coming from the propeller can influence the propeller next to it, again contributing to the non-uniformity of the inflow. For WASP, the amount of propellers should be considered well, as these propellers would operate for large parts of operations in these asymmetrical conditions.

The wake of propellers is, besides the ship hull and the drift angles, also dependent on advance coefficient J. L. Wang et al. (2023) numerically examined the wake of an INSEAN E779A propeller for two different advance coefficients; $J = 0.65$ and $J = 0.38$. The wake of a propeller in open-water conditions was tested without applying drift angles. The wake produced by the higher loaded propeller differs from the lighter loaded propeller in several aspects. The velocity profile behind the high loaded propeller is mostly dominated by the axial velocity. This is a result of the higher loads that the propeller exert on the water. However, L. Wang et al. (2023) found that that wake is less stable than for the propeller in light loading conditions. The wake of the lighter loaded propeller has a higher convection velocity, which reduced the interaction between tip vortices and avoid wake instabilities. This phenomenon is also observed further downstream of the propeller. As the propeller with low advance coefficient is producing a less stable wake, the wake of the propeller is less observable.

Ducts can diminish the influence of oblique flow. This was investigated by Q. Zhang et al. (2020). Ducts are devices that are placed around the propeller to straighten the inflow to the propeller. Ducts are mostly used for highly-loaded propellers, as the most losses are regained in this loading domain. Numerical simulations were performed at very high drift angles, up to 60 degrees, to prove the working of a nozzle. The main conclusion of the authors is that torque of a propeller with a duct in oblique flow is, for a certain amount of generated thrust, is lower than without a duct. The main reason can be found in the straightening of the flow in the nozzle and the additional generation of thrust by the

nozzle itself. However, the ducted propeller showed a faster reduction in thrust than the open propeller for increasing J, showing its range of interest. This means that nozzles are best applicable on ship that frequently perform manoeuvring operations, as the nozzles benefits are found for low advance coefficients in combination with high drift angles. On the contrary for WASP, this would lead to faster thrust reductions of propeller, and therefore decrease the efficiency of the WASP system. Moreover, pressure distributions still show asymmetry in pressure on the propeller blades at different positions. The starboard side of the propeller still experiences oblique inflow due to the high drift angles. Therefore, the pressure on the suction side is way lower at this position in comparison to the other blades.

Pressure distribution

As the velocity distribution is varying, the pressure distribution on the propeller blade is also changing during a rotation. To compare these pressures, a pressure coefficient is introduced. The pressure is normalised using formula 3.1.

$$C_P = \frac{p - p_0}{\frac{1}{2}\rho_w V_{rel}^2} \tag{3.1}$$

Here C_P is the pressure coefficient and $p - p_0$ the relative pressure in $\frac{N}{m^2}$. L. Wang et al. (2019) compared numerical simulations of the pressure distributions over the chord of the propeller blade to experimental values. These are given in Figure 3.5.

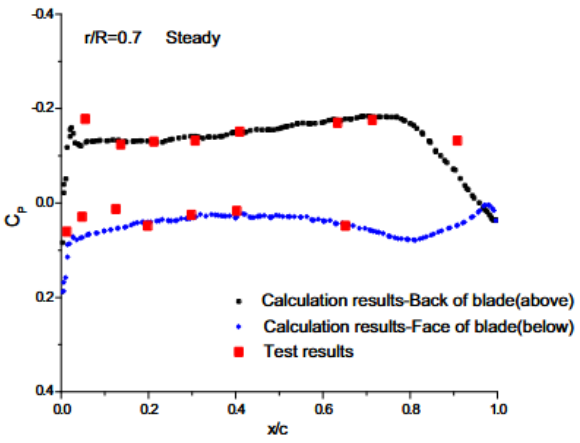

(a) Pressure coefficient for β=0°, θ=90° (L. Wang et al. (2019))

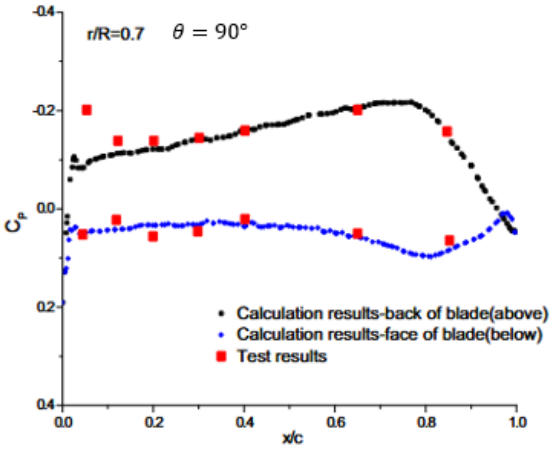

(b) Pressure coefficient for β=7.5° at θ=90° (Adapted from L. Wang et al. (2019))

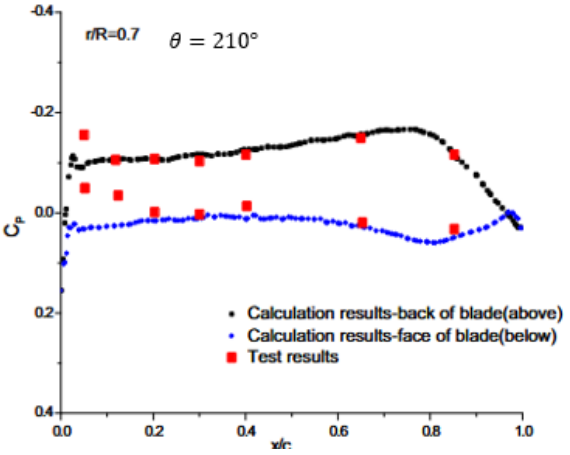

(c) Pressure coefficient for β=7.5° at θ=210° (Adapted from L. Wang et al. (2019))

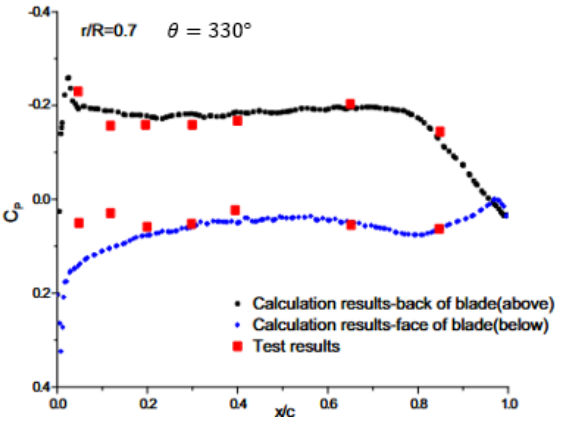

(d) Pressure coefficient for β=7.5° at θ=330° (Adapted from L. Wang et al. (2019))

Figure 3.5: Pressure distributions for different blade positions and drift angles (Adapted from L. Wang et al. (2019))

According to Wang et al., these distributions are important as thrust is highly related to these pressures. As can be noted, the value for the back and face of the blade are the same at x/c=1.0 indicating that this is the trailing edge. Figure 3.5a and 3.5b shows that a drift angle does not influence the loading of the propeller on $\theta = 90°$ as the values are almost the same. In Figure 3.5c and 3.5d, the distribution at $r = 0.7R$ is very similar to the other positions but some aspects differ. Firstly, θ=210° is close to the lowest position of the propeller blade. Here the values of the pressure coefficient are the lowest. In Figure 3.5d, the position is close to the twelve o'clock position, which experiences the highest pressure. Moreover, the peak at the leading edge indicates that the propeller loading is highest at this position. L. Wang et al. (2019) also showed that for the same position and drift angle, and a lower advance coefficient J that those peaks become even larger, as the loading of the blade is also larger. Gaggero et al. (2019) also stated that higher drift angles also enlarge the difference between the 0 degrees positions and the 180 degrees position. Also, the radial distribution changes as a result of the drift angle. The tip is highest loaded in the top position and this loading is increasing for increasing drift angle. Before and after the 0 degrees position the middle part of the propeller blade is higher loaded.

Y.-x. Zhang et al. (2020) also visualised the pressure distribution for varying drift angles. The aim of the paper is to find the periodic loads in oblique flow, and the pressure distribution gives a good insight in the distribution of the forces for each circumferential position. In Figure 3.6, the pressure distribution for both the suction side as the pressure side are given, for drift angles varying between β=-20° and β=20°

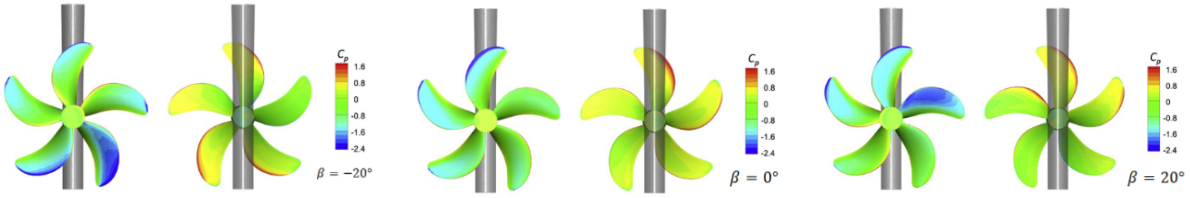

(a) Pressure coefficient for β=-20° (Adapted from Y.-x. Zhang et al. (2020))

(b) Pressure coefficient for β=0° (Adapted from Y.-x. Zhang et al. (2020))

(c) Pressure coefficient for β=20° (Adapted from Y.-x. Zhang et al. (2020))

Figure 3.6: Pressure distributions for different drift angles, suction side(left) and pressure side (right) (Adapted from Y.-x. Zhang et al. (2020))

Here, again the difference between the blade at the top and the blade at the bottom is clearly visible. Firstly, for positive drift angles the high pressure at the pressure side is found in the top region. This is in line with what other research showed. However, for negative drift angles the peak values are found in the 180 degrees position. This could indicate that this simulation belong to an open-water set-up. However, the authors do not specify this, as both open water as simulations with a hull are performed. As stated before, the radial distribution is clearly visible. At the top, for positive drift angles, and bottom, for negative drift angles, the tip is higher loaded, whilst the middle part is higher loaded in the regions next to it.

3.1.2. Wake at and behind the propeller plane

Propellers are mostly operating in front of a rudder, so the wake profile of propellers at drift is of importance for the rudder as this experiences this wake as inflow. Felli et al. (2009) experimentally studied the wake of a propeller in combination with a rudder using LDV. The focus of Felli's research is on vortices interacting with the rudder. One of the phenomena described is the collision of the flow with the leading edge of the rudder profile. Figure 3.7 shows axial velocity planes before and behind the rudder, for different blade positions.

In the position of the propeller blades, it can be clearly observed that the flow is accelerated. However, a lower axial velocity due to the presence of the rudder can be found in both considered planes. Even in the plane before the rudder a velocity dip is observed. This can be declared by both the approaching of the stagnation point and the experimentally observed deformation of the tip vortex when approaching the leading edge of the rudder. The velocity behind the rudder is lower because of both viscous losses on the rudder surface and viscous effects in the boundary layer and momentum transfer to other velocity components (Felli et al. (2009)). This momentum transfer changes the direction and

thus the contribution to the axial component of the velocity as a side force is generated. Felli et al. also described the tip vortex-rudder interactions, which can be seen by the highest velocity deficits.

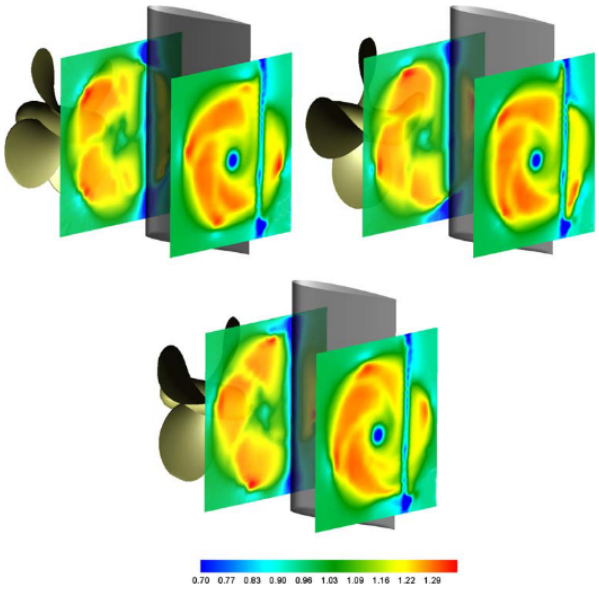

Figure 3.7: Axial velocity for blade positions: $\theta = 0$ (left), $\theta = 30$ (right), $\theta = 60$ (bottom) (Felli et al. (2009))

Dubbioso et al. (2013) included the influence of both advance coefficient and drift angle in their research. On the propeller disk, the distribution of both pressure and velocity is different than for wake profiles described in section 2.1.3. This is caused by the fact that Dubbioso only included a propeller in the simulations. The axial velocity profile of the propeller is mostly changed by the induced velocities of the propeller itself. These induced velocities cause a low speed region in the 180 to 270 degrees quadrant. This is opposite to the wake profile of a propeller behind a ship, since the wake is dominated by the velocity deficit caused by the ship in that case. In this paper, the open water effect leads to higher loads on the lower propeller blade.
It was found that a drift angle shifts the peak in loading on the propeller blade to a position between the 180 and 270 degrees position. As the blade is loaded the most in this region, the pressure profile shows a peak here. The peak in pressure even increases when the advance coefficient drops. This also has its effect on the propeller wake. In Figure 3.8 the total velocity is shown for both a lightly loaded propeller with a small drift angle in Figure 3.8a and a medium loaded propeller with a big drift angle in Figure 3.8b.

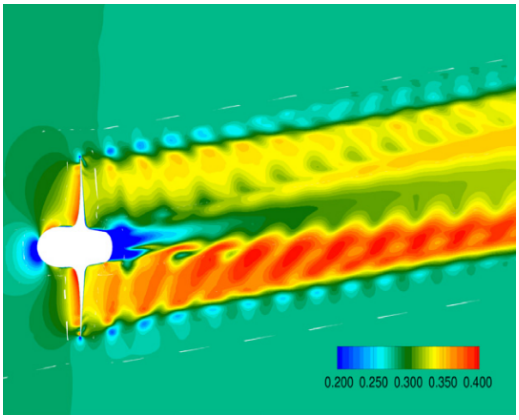

(a) J=0.88, β=10° (Dubbioso et al. (2013))

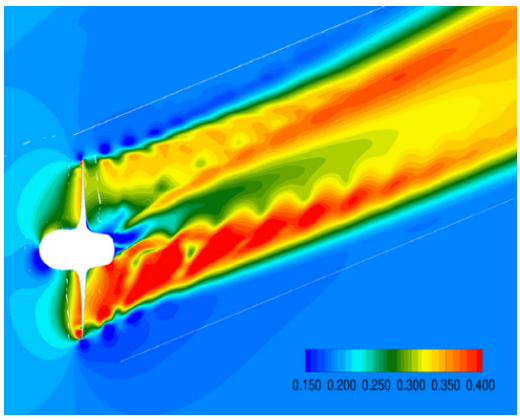

(b) J=0.60, β=30° (Dubbioso et al. (2013))

Figure 3.8: Profile of absolute velocity for two different advance coefficients (Dubbioso et al. (2013)

In these Figures, some important differences where highlighted by Dubbioso. First, the difference in velocity of the flow behind the propeller is different on the port side and the starboard side. This is due to the asymmetrical loading of the propeller. The highest loaded part also accelerates the flow the most behind the propeller. The difference becomes more significant for increasing drift angle. The second main difference is in the interaction between vortices in the wake. In Figure 3.8a, the vortices of the propeller tip can be distinguished and are not interacting. On the contrary, some interaction can be observed at higher drift angles. The authors concluded that both the drift angle and the convection speed of the vortices are advantageous in this case to amplify the interaction behind the propeller.

Felli and Falchi (2018) experimentally studied a propeller under an inclination angle using PIV to visualize the flow. In open water, the flow effects of this set up are similar to a drift angle. The mean velocity field show the influence of the inclination angle. In Figure 3.9a, it can be seen that the flow is symmetric, as the inflow the same on each propeller blade. Also the path of the hub vortex can be located, as the velocity is lower there. Due to turbulent diffusion, the velocity reduces when propagating further downstream. In Figure 3.9a and 3.9b, it can be seen that the flow is not axisymmetric anymore, as a result of the inclination angle. A difference of both propeller sides is observed. In the region of high thrust loading the velocity is again the highest. This difference is increased when the inclination angle is increased. However, it can be seen that further downstream the windward and leeward side of the wake of the propeller are more difficult to distinguish.

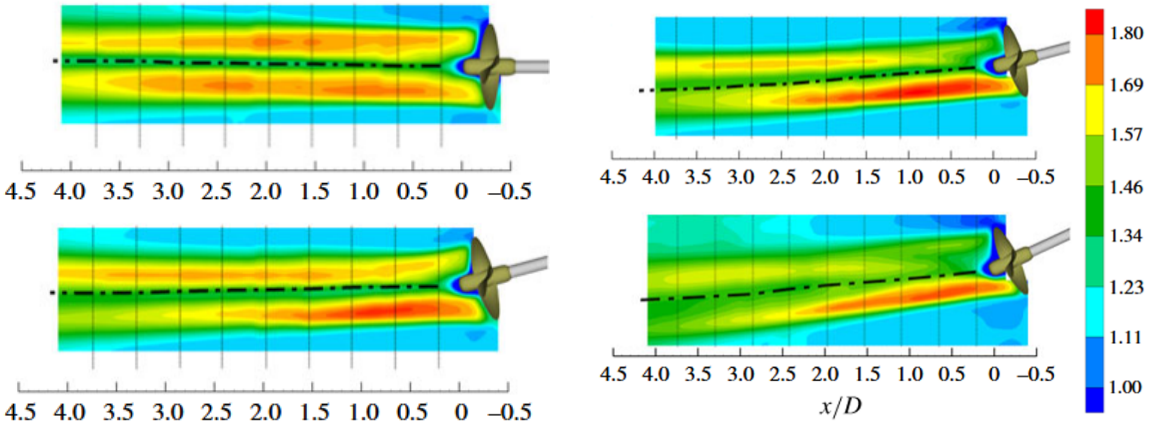

(a) β=0° and β=7.5° (Felli and Falchi (2018))

(b) β=15° and β=22.5° (Adapted from Felli and Falchi (2018))

Figure 3.9: Profile of the stream-wise velocity behind propeller for different inclination angles (Adapted from Felli and Falchi (2018))

Felli and Falchi (2018) also describe several vortex systems in the wake of the propeller. These consist of the hub vortex and tip vortices, where the leeward and windward side of the propeller differ as the vorticity is in the opposite direction. Moreover, due to the inclination angle there are also so-called 'trailing vortices' and 'shed vortices', which represent secondary vortex systems. However, since this is outside the scope of this report, this will not be explained further here.

3.2. Propeller forces and moments

In the section before the focus was on the flow parameters due to oblique inflow. As the main research field related to oblique flow is manoeuvring, most research focusses on finding the forces and moments generated by the propeller determining the manoeuvring capabilities of a ship. In this section, the propeller performance for a ship under different drift angles, subsection 1, and advance coefficients, subsection 2, will be shown. Also, the in-plane forces generated by the propeller are explained in subsection 3. The last subsection shortly covers the influence of the propeller forces on global ship forces and manoeuvrability of the ship.

3.2.1. Influence of drift angle

A drift angle changes the distribution of thrust and torque during a rotation, which is mainly caused by the changing angle of attack. This effect is for example shown by the numerical work of Y.-x. Zhang et al. (2020) and C. Wang et al. (2017). In Figure 3.10a the non-dimensional thrust generated by one blade during a rotation is shown for different drift angles. Figure 3.10b shows K_T and $10K_Q$ for a propeller in open-water conditions for one specific drift angle, as a function of blade position θ.

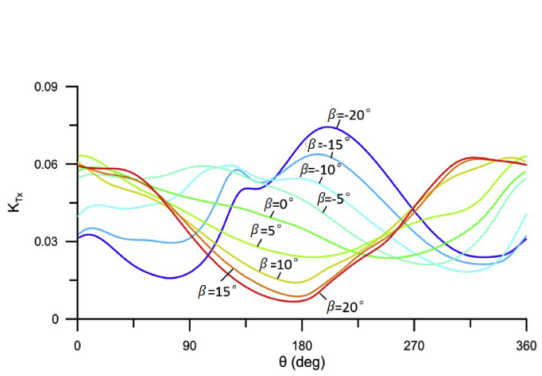

(a) Single blade thrust load for different drift angles (Adapted from Y.-x. Zhang et al. (2020))

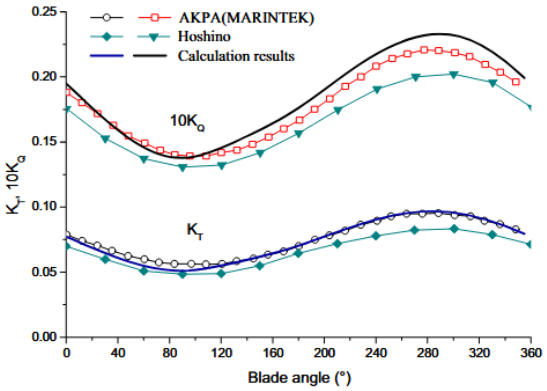

(b) K_T and $10K_Q$ for β=7.5° (C. Wang et al. (2017))

Figure 3.10: Blade loads for propellers at a drift angle at different blade positions (Adapted from Y.-x. Zhang et al. (2020) and C. Wang et al. (2017))

Figure 3.10b shows the same variations as the angle of attack. Both coefficients are varying sinusoidally, like the angle of attack as shown earlier with the inflow vectors. However, the lowest values are observed on the starboard side of the propeller plane (90°) is caused by the test conditions. The propeller is placed under a pitch angle here, instead of a drift angle. A pitch angle has the largest influence on port side and starboard, whilst the top and bottom parts are unaffected. Compared to a drift angle, the variation is shifted 90 degrees. Y.-x. Zhang et al. (2020) also noted that thrust and torque increase almost linearly for increasing drift angle. However, for the highest considered drift angles, the trend becomes slightly non-linear and thrust increases faster for increasing β. The reason for this is that the axial component of the inflow velocity decreases for increasing drift angle, resulting in a higher thrust loading.

This almost perfect sinusoidal variation disappears when the propeller is behind a ship. However, in Figure 3.10a, which shows the behind-hull condition, a similar trend as for oblique flow in open-water conditions is still observed. For straight ahead conditions, the highest contribution to thrust is done in the top position, whilst the least thrust is generated in the lower half of the propeller. As can be seen in Figure 3.10a, the lowest thrust is not perfectly at 180°, as the ship shift the positions as the wake profile of the ship mixes with the oblique inflow. For clockwise rotating propellers, this means that the location of maximum thrust shifts in starboard direction. The positive drift angle amplifies the minima and maxima, as the direction of the flow contribute to a higher and lower angle of attack in the 0 and 180 degrees position respectively. For the negative drift angles, the distribution flips, as the blade load is higher on the opposite side of the propeller. This is caused by the fixed direction of rotation of the propeller, which induces opposite effects on each blade position. It should be noted that the influence of the drift angle on the lower half of the propeller plane is way bigger than on the upper half. This difference is caused by the presence of the ship diminishing the effect in the upper half.

The presence of the ship is for example studied in some experimental research on capturing propeller forces behind a ship. Ortolani et al. (2018) described a experimental test using the twin screwed ship, as introduced before. Here again, the focus was to capture the differences between the leeward and windward propeller during manoeuvring operations. The wake evaluation of the propellers was performed for the steady turning manoeuvres. The thrust on the propellers is evaluated in Figure 3.11. Note that here rudder angle δ is used to show the oblique inflow. This is not exactly the same as the drift angle to the rudder.

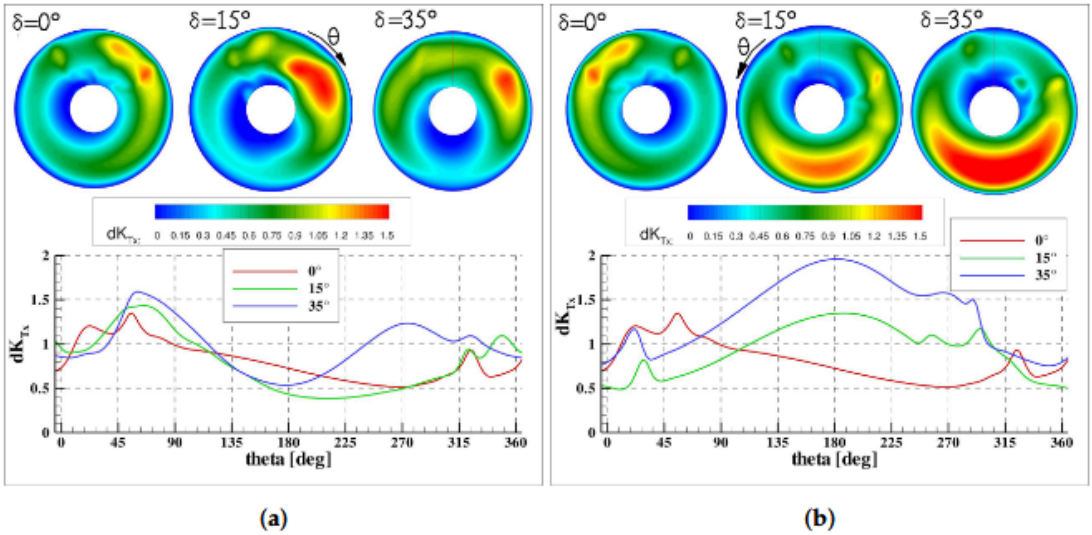

Figure 3.11: Thrust on the propeller blades of the (a) Internal propeller and (b) External propeller (Ortolani et al. (2018))

As can be seen the counter-rotating propellers have a similar thrust loading in straight ahead conditions. For $\delta = 0$, the higher thrust loading is found in the top part that is the closest to the hull, due to the velocity deficit. During manoeuvring, the thrust distribution over the blade start to vary between these propellers. Starting with the external propeller, which is not operating in the wake of the ship for high drift angles, shows indeed the behaviour of a propeller in open water under pure oblique inflow conditions. The fact that the thrust is mostly generated in in the bottom position of the propeller disk is due to the rotation direction of the propeller. The thrust loading distribution of the internal propeller is completely different. For δ=15°, there is large influence of the skeg vortex, as this propagates in the propeller plane. For the highest drift angle, there is less influence of this vortex, as this propagates past the propeller plane. Also the imbalance between both sides is reduced for the internal propeller, as the tangential up-going flow coming from the ship is dominant in this region compared to the oblique inflow.

Also, Lücke (n.d.) focus on ships that will encounter off-design conditions for a large parts of its operational time, which is the case with WASP. In this study a RoRo-ship is used to perform a case study where wind and current form a certain angle are included. To compensate for the forces originating from those factors, a rudder is needed to avoid long exposure to cross flows. However, in the paper it was shown that the rudder angle needs to be 5 degrees to maintain a small drift angle of 1 to 2 degrees. This shows that the conditions described in this section could be probably faced during trips of a WASP ship.

The effect of drift angle on the total thrust and torque is also captured by the experimental study of Gutsche (1964). In this study, Gutsche tested six different propeller models in open-water conditions. These propellers tested covered different inclination angles, P/D-ratios and blade area ratios. Based on the results of the experiments, Gutsche developed a approximation method for thrust and torque at an inclination angle compared to an already known open-water characteristic. This method is based on a change in the advance coefficient and in the circumferential velocity. From these changes the change in both K_T and K_Q can be approximated. This calculation method is shown in Appendix D, in chapter 11.

3.2.2. Influence of advance coefficient

Oblique flow is mostly found in conditions where the speed of the propeller is low, as this is the case during ship manoeuvres. This means that the propeller is typically highly-loaded in those conditions. However, WASP ships will operate at a relatively high advance coefficient. The propeller is in fact unloaded by the added wind energy resulting in lightly-loaded propeller blades. Therefore, the influence of advance coefficient is as important as the influence of the drift angle.

Firstly, in open-water conditions thrust and torque decrease for increasing J. The rate of decrease is

dependent on the parameters of the propeller geometry. Yao (2015) studied the influence of both drift and advance coefficient on the forces developed by the propeller. This was done by systematically varying the drift angle between 0 and 30 degrees or by changing the rotational speed of the propeller, to operate under a different advance coefficient J. This was done by performing full-scale RANS simulations on a propeller in open water. The numerical method used is OPENFOAM, where a sliding grid was applied to the propeller area to capture the forces of the blade on each position during rotation. The simulations show decreasing thrust for increasing J as in open-water diagrams. Side force and vertical force increase for increasing advance coefficient. The moments follow almost the same trend as the forces. Moreover, the main conclusion that was drawn from the measured forces and moments is the dependency of the advance coefficient on the sensibility of propeller forces to a drift angle. For lower advance coefficients, the influence of the drift angle reduces compared to higher advance coefficients. So, at high thrust loading, the propeller is less prone to fluctuations of the inflow velocity. This effect can be explained the inflow vectors, which were explained in section 2.1.4. For high J, there are two conditions that can lead to a different relative inflow vector V_{rel}. The rotational speed V_{rot} can be lower than for low advance coefficients. When the rotational speed decreases and other velocities remain the same, the angle of attack of the propeller blade decreases and produces a lower thrust and torque. The second condition is that the speed of the ship is higher compared to a situation with low J. In this case V_A is higher, which again reduces the angle of attack. The reason that the change in angle of attack is more significant for high J is that the rotational or circumferential velocity V_{rot} is low compared to the advance velocity V_A in this case. The drift angle only changes the advance velocity. However, the rotational speed is also affected by the drift angle due to the contribution of the tangential component. The share of the change in the the relative inflow velocity is bigger when the circumferential velocity is relatively small. Also the share of the tangential contribution to the circumferential velocity is relatively bigger in this case. Therefore drift angles influence propeller forces and moments more for a high advance coefficient. This influence of J in open water is shown in Figure 3.12.

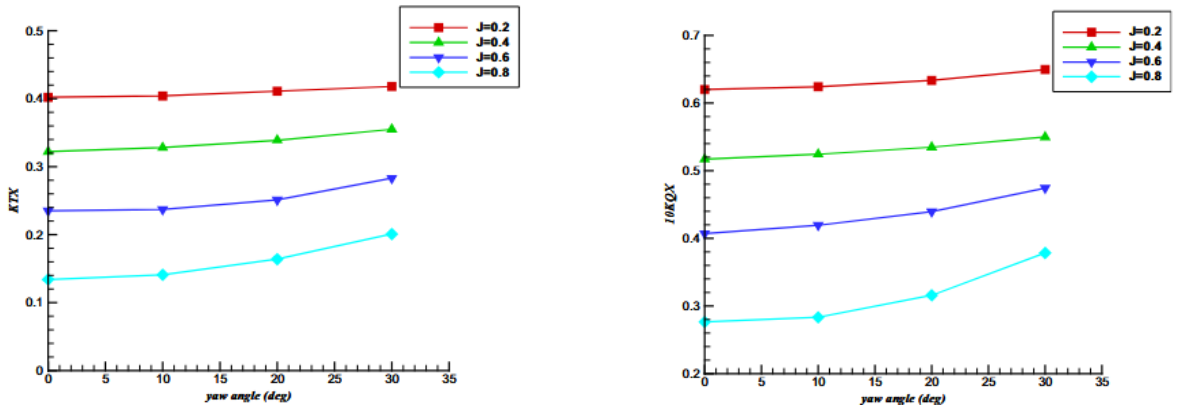

(a) K_T against drift angle for different J (Shamsi and Ghassemi (2017))

(b) $10K_Q$ against drift angle for different J (Shamsi and Ghassemi (2017))

Figure 3.12: K_T and $10K_Q$ against drift angle for different J (Shamsi and Ghassemi (2017)

As already explained, it can be observed that increasing drift angles are affecting propeller performance more for high advance coefficient. Shamsi and Ghassemi (2017) showed that the increase in drift angle from 0 to 30 degrees is only resulting in 4% more thrust for the lowest J, while this is more than 50% for the highest J. For WASP applications, the influence of advance coefficient is therefore of great importance as the range of forces acting on the propeller is much higher of a propeller that is working in conditions with high advance coefficient in combination with a drift angle.

3.2.3. In-plane loads

Drift angles cause asymmetry between top and bottom half of the propeller plane and there is also difference between starboard and port side of the propeller. These imbalances cause a new problem, as the forces generated on opposite sides of the propeller are not of the same magnitude anymore. In Figure 3.13 the generation of in-plane loads is visualised.

On the left side, the forces in the upper and lower half are not equal to each other. This is caused by the fact that on the top half of the propeller, the drift angle increases the generation of side force, as the total force is higher as a result of increased angle of attack. On the bottom half, this effect is opposite, and the tangential flow component are in the same direction as the propeller. The result is that net side force is produced by the propeller. This force is in the same direction as the side force produced in the upper half. Moreover, the difference in magnitude introduces a bending (pitch) moment in the vertical plane. On the right side, it is shown that the imbalance between the left and right half of the propeller plane result in a net force that is in the same direction as the force generated on the right side of the propeller plane. This result in a moment around the z-axis of the of the propeller.

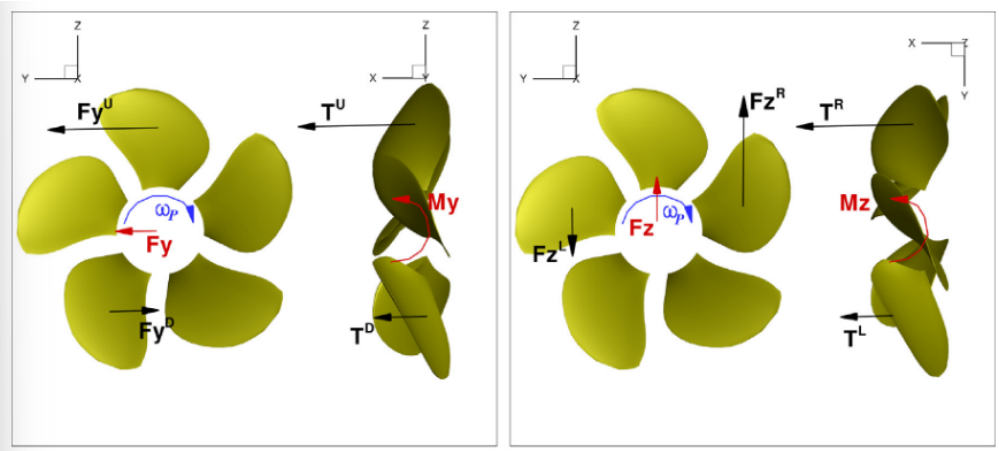

Figure 3.13: Generation of in-plane loads (Muscari, Dubbioso, Ortolani, and Di Mascio (2017))

The in-plane forces and moments generated by a propeller were numerically analysed by Dubbioso et al. (2013) using an unsteady RANS model in combination with overlapping grids. The goal of these simulations is to find the bearing loads that the propeller produces during manoeuvres. They used the CNR-INSEAN E779A propeller to compare two different advance coefficients J and multiple different drift angles. The two conditions which represent real operating manoeuvring conditions were analysed using a finer grids, as these cases were of the highest interest of the authors. These conditions are $J = 0.88; \beta = 10°$ and $J = 0.60; \beta = 30°$, which correspond with two different phases during manoeuvring. The first is typically the start of a manoeuvre, with low drift angle and still relative high ship speed, and thus a higher J. The second condition is during the manoeuvre itself, where the drift angle increases, and the speed, and therefore J, decreases. The forces and moments that were generated are calculated for three different drift angles, including the cases mentioned above. In Figure 3.14 the results of Dubbioso et al. (2013) are given.

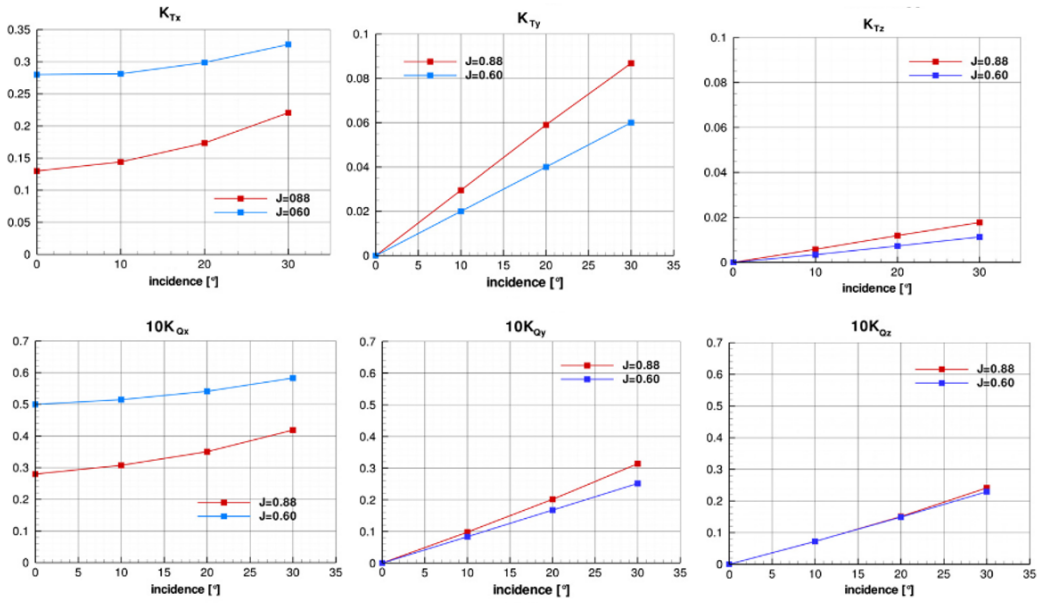

Figure 3.14: In-plane loads for different drift angles and advance coefficients (Adapted from Dubbioso et al. (2013)).

Firstly, as already mentioned, the forces and moments increase at a different rate for increasing drift angle when comparing two advance coefficients. For the thrust, it can be seen that thrust increases faster for the higher advance coefficient. However, this trend is less for propeller torque. According Dubbioso et al. (2013), this is related to the source of the thrust and torque generation. Thrust is related to pressure effects, whilst torque originates from viscous effects. At higher advance coefficients, the pressure effects must therefore increase faster than the viscous effects, as the thrust increases faster than torque. Moreover, this implicates that propeller open water efficiency also increases faster for high J, as K_T increases faster than K_Q, see equation 2.6. Also, the side force and vertical force show a faster increase for low thrust loads. The vertical force is smaller than the side force, as the imbalance between upper and lower half is amplified by a drift angle, whilst the sides are almost unaffected. The in-plane moments seem to be less prone to varying advance coefficient, as these moments increase almost at the same rate.

The in-plane loads of a propeller blade are varying during a rotation, as this is the case with thrust and torque. In Figure 3.15, the forces and moments on one propeller blade during one propeller revolution are shown. Note that the propeller is rotating clockwise and that in this paper the 90 degrees position is referred to as the top position of the propeller.

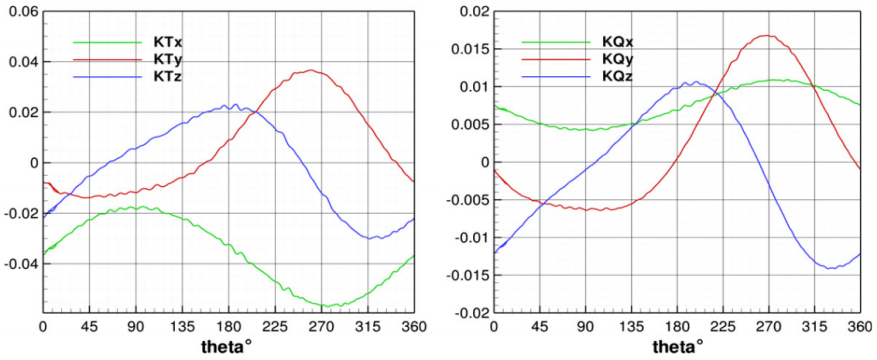

Figure 3.15: Forces (left) and moments (right) generated by one propeller blade (Dubbioso et al. (2013)) for J=0.88 and β=10°

The sinusoidal trend of the forces and moments is again observed. What can be noted is that the side

force and thrust have a small phase shift in the bottom position of the propeller plane. According to Dubbioso et al. (2013), this can be ascribed to the fact that thrust is mainly affected by the pressure field, while the side force is dependent on viscous effect in the boundary layer of the propeller blade. Moreover, the vertical force has a phase shift of $\frac{\pi}{2}$, as the generation of this force is caused by the imbalance of the left and right half of the propeller plane. However, despite having no vertical component in the inflow, the vertical force still appears in this set-up. Dubbioso et al. (2013) concluded that the non-uniform inflow also causes the presence of vertical components.

A problem caused by those in-plane loads is the influence on the strength of the propeller. The fact that the forces and bending moments vary periodically introduce vibrations that can damage the propeller and shaft. C. Wang et al. (2017) analysed the frequencies of the forces and moments. In this numerical study, a three-bladed propeller in open-water conditions was analysed. The frequencies that were observed from the frequency-domain signal are the blade passing frequency and multiples of that. Also the shaft frequency was observed. The in-plane forces and moments showed the same frequencies as the thrust and torque, but their amplitude is even higher. This means that despite having a lower time-averaged value, the in-plane loads are of great importance regarding the vibrations of the propeller.

In-plane loads are also analysed for twin-screwed ships, as the non-uniform inflow is even greater when the propeller is not centered behind the ship. The propellers are working in different inflow fields and therefore also the side force and vertical force can vary between the two propellers. Ortolani et al. (2018), Ortolani and Dubbioso (2019), Ortolani et al. (2020) described the same case and were able to experimentally determine the variations of the in-plane loads. The external propeller, in almost open-water oblique flow, shows indeed that side force and vertical force are generated in the regions as shown in 3.13. The magnitude of both forces increases with the drift angle increasing. On the internal propeller, the distribution of side and vertical force seems to be less influenced by the drift angle. The peaks in both forces are lower, as the flow to the propeller is straightened by the ship hull. Locally, due to the influence of vortices and ship wake there are bigger contributions to the forces, but in general produced side and vertical force components are lower due to the smaller experienced drift angle. Moreover, in Sun et al. (2023), the effect of negative drift angles was added. There it was found that for the internal propeller, the side force was the lowest in straight ahead condition, whilst the moments are lower at a negative drift angle.

3.2.4. Influence on ship forces

Drift angle also influence forces on the ship before the propeller. The biggest differences can be found in the forces on the ship itself, which influence the course of the ship. These are the resistance force, side force and yaw moment. The influence of β on these forces and moment is shown by Sun et al. (2018). In this research the forces on a bare hull are simulated as the influence of a ship in combination with a propeller was examined. A Volume of Fluid method was used to account for free surface effects. The range of drift angles is the same range that could be expected for WASP ships, that are drift angles up to a maximum of 15 degrees. It was shown that the side force and yaw moment grow proportional to the drift angle. The resistance force on the hull also increases but there is a non-linearity when increasing the drift angle. Between β=5° and β=10°, the resistance force increases faster than outside this region. The same trend was found by Y. Zhang et al. (n.d.), who used a BEMT model in combination with RANS to analyse ship and propeller forces at a drift angle. One reason mentioned for this is the fact that the area that is exposed to the incoming flow is bigger and therefore a larger total force and moment is generated. Also the increasing bow wave on the windward side of the ship bow increases the resistance, as frictional and wave making resistance increase due to the bow wave. This is also the reason that resistance increases fast between certain angles. Also flow separation was mentioned as a cause of the increase of both the forces and the yaw moment, as this results in a higher viscous pressure resistance. Longo and Stern (2002) showed that these forces and moments are also depended on Reynolds number. For a ship without a propeller they found that the resistance gradually increases for increasing Froude number. Due to the rapidly increasing wave making resistance, a rapid increase was found between two Froude numbers. The side force and yaw moment are almost independent of the Froude number. However, for high Froude numbers, the influence of drift angles on side force and yaw moment becomes larger, as the bigger drift angles show a larger growth at these Froude numbers.

The main reason that these forces are important is for course keeping of the vessel. When a WASP

ship sails at a drift angle, the above-mentioned forces needs to be cancelled by the propellers or the rudder. Ortolani et al. (2018) already explained that the side force of the propeller is stabilizing the ships course, as the force is always directed to the centre of the ships curvature trajectory. This means that when a ship tends to rotate to port side, the propeller side force is also directed in this direction and creates a yaw moment in the opposite direction. One additional problem for WASP ships could be the Munk moment. This is a destabilizing yaw moment that tend to increase the yaw angle of the ship (Perez and Blanke (2002)). This is caused by the fact that a ship at drift is translating and the forces acting on the ship hull will produce a non-zero moment in this situation.

3.3. Propeller-rudder interactions with a drift angle

Most ship propellers operate before one or more rudders, which is therefore in the wake of the propeller. This influences the performance of the rudder. The two major effects of a propeller are the influence on the experienced angle at which the flow encounters the rudder, and the influence on the lift and drag forces on the rudder. To capture the influence, both experimental and numerical studies give insight in propeller-rudder interaction.

The presence of the propeller influences the direction of the flow. When the flow is entering under a drift angle, this definitely has an effect on the propeller and rudder. However, the rudder experiences this drift angle way less than the propeller or the ship hull. This is caused by flow straightening effects. Flow straightening is extensively studied by Molland and Turnock. They performed several experimental tests in the wind tunnel of the university of Southampton to capture those flow straightening effects. The influence of different centreboards or a hull in front of a propeller-rudder configuration was studied by Molland and Turnock (2002). Also, for a bare propeller-rudder configuration, two different rudders were compared to find the influence of the propeller itself. In this paper some terminology is used to describe flow straightening, as shown in Figure 3.16.

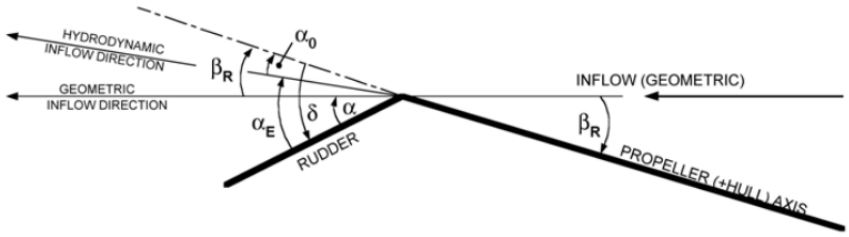

Figure 3.16: Flow straightening terminology (Molland and Turnock (2002))

Here β is the geometric drift angle, α the geometric rudder angle, α_E the effective rudder angle, δ the nominal rudder angle and α_0 the rudder angle for zero lift. From this figure, the flow straightening factor γ was derived.

$$\alpha_E = \delta - \gamma\beta \tag{3.2}$$

$$\gamma = \frac{\alpha_0}{\beta} \tag{3.3}$$

As can be seen, flow straightening affects the effective rudder angle, as zero lift is obtained on a different position than in straight ahead conditions. This is indicated by the fact that the rudder angle is not equal to the drift angle of the ship. From the tests it was found that flow straightening is depended on both the configuration before the propeller and rudder and also on the advance coefficient.

Molland and Turnock observed that γ is the highest for the lowest J at the highest drift angle (15°). For smaller angles, this effect is less important and in some test results the influence was even reversed. Moreover, it was found that the configuration before the propeller-rudder system is of big importance, as centreline boards showed more flow straightening than propeller and hull only. A small increase

in flow straightening was observed for increasing length of these boards. Lastly, the influence of the span of the rudder was also tested, as increasing the span leads to a reduction of the percentage of the rudder that is in the propeller slip stream. As expected, this leads to less total flow straightening as the top of the rudder is not or less affected by the flow straightening of the propeller.

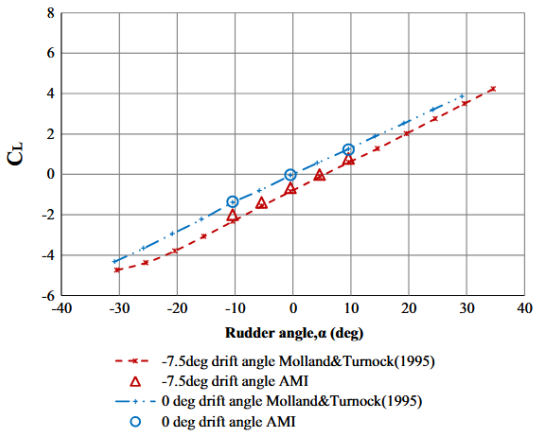

(a) C_L for propeller and rudder with a drift angle (Badoe et al. (2015))

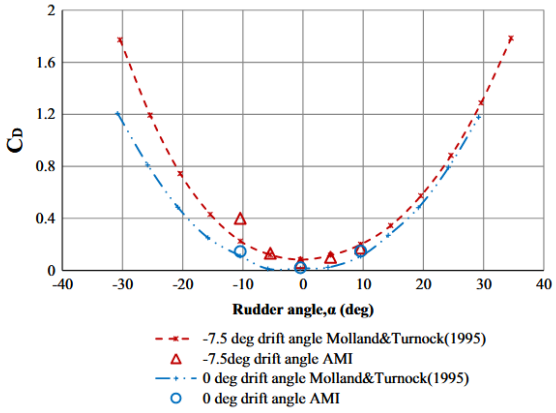

(b) C_D for propeller and rudder with a drift angle (Badoe et al. (2015))

Figure 3.17: C_L and C_D for propeller and rudder with a drift angle (Badoe et al. (2015)

Badoe et al. (2015) repeated this research numerically, for the propeller-rudder configuration in an open-water set-up at different drift angles. The results for the lift and drag measured on the rudder are given in Figure 3.17. Badoe et al. (2015) observed that the trend of the lift curve remains the same when a drift angle is applied. However, the whole line is shifted downwards, shown in Figure 3.17a, so zero lift on the rudder is now reached when the rudder is also at an angle. They noted that these forces depend on their propeller force calculation, as a slight over-prediction of the forces leads to discrepancies for the rudder lift and drag. Also, the influence of the advance coefficient J on C_L and C_D was found. The highly-loaded propeller (low J) has a steeper slope of lift coefficient for varying rudder angles than than mildly-loaded propellers. As stated, a higher thrust loading also increases the drag on the rudder.

Badoe et al. (2015) also showed the influence of flow straightening devices on propeller thrust and side force. The less flow straightening, the higher the influence on the thrust of the propeller, as the flow before the rudder is affected by the blockage of the rudder itself. The highest side force is generated by the device that straightens the flow the most. Moreover, it was found that for high advance coefficients, the propeller side force is bigger than for low advance coefficients for increasing rudder angles.

As RANS simulations of a fully described hull-propeller-rudder system still requires big computational efforts, lower fidelity models were compared by Bruzzone et al. (2014) to capture propeller-rudder interaction accurately. Propeller forces were inserted in the momentum term of the (time-varying) Navier-Stokes equations. Four methods for determining propeller forces were used: Actuator disk, radial distribution, body force approach and a full RANS method. The methods were compared by lift and drag on the rudder and their distribution over the span of the rudder. RANS simulations showed the most accurate results whilst actuator disk showed the highest discrepancies. However, the authors concluded that the radial distribution, which can be determined using BEMT, is the best trade-off. The lift coefficient was less accurate than the higher fidelity models, but the rudder load distribution almost followed the same trend. The peak of the load is shifted downward span-wise, but it has the same magnitude as the higher fidelity models. Phillips et al. (2010) found the same results. He described the propeller by applying both axial momentum and angular or tangential momentum source terms to the flow. Philips et al. found that results of a predefined distribution of thrust and torque and that of a BEMT solver are both able to predict the lift and drag on the rudder. On the contrary, uniform thrust distribution overestimates rudder drag, since it cannot capture swirling components of the flow.

Also, Morteza Javadpour et al. (2019) concluded that the propeller affects the rudder more than vice versa, as the propeller is upstream of the rudder. They showed the difference between a rudder without

and behind a propeller, where rudder forces behind a propeller are higher for each rudder angle than the corresponding forces without a propeller. Muscari, Dubbioso, Viviani, and Di Mascio (2017) compared the performance of the two propellers on a twin screw vessel, where the flow to the rudders differ significantly. The windward rudder experience high influence of the cross flow to the effective rudder angle, while the leeward rudder experience an effective rudder angle that is almost equal to the nominal rudder angle. The rudder experiences an influence of the propeller and hull. The effective angle of attack of the rudder experiences the biggest influence of the propeller. As described by Muscari, Dubbioso, Viviani, and Di Mascio (2017), a drift angle on the rudder changes the effective angle of attack, as it is not only influenced by the nominal rudder area but also by flow straightening effects. The flow straightening effect can be obtained from the propeller loading. As the rudder side force in straight ahead conditions can be obtained, it is possible to capture the differences when a drift angle is applied. The difference between the rudder angle needed to deliver the same side force as for straight ahead conditions is the flow straightening factor γ.

He and Kinnas (2017) studied the unsteady interaction between the propeller and rudder. The rudder is influenced by induced velocities of the propeller, while the presence of the rudder under an angle of 5 degrees induces some extra unsteadiness in the thrust delivered by the propeller. This is caused by the fact that the propeller is in the unsteady wake of the propeller. According to He and Kinnas (2017), the difference in K_T can be declared by the blockage effect by the rudder. The influence of the distance between the propeller and the rudder is shown in Figure 3.18. In Figure 3.18b, the lift coefficient is shown. It changes during a propeller revolution. However, when the distance from the propeller becomes larger, there is less interaction with the propeller wake. As the inflow for the rudder becomes more steady, the lift force will also show less fluctuations. The conclusion of He and Kinnas (2017) is that there is almost no influence when the rudder is placed further than a distance of $1.50R$. However, the propeller thrust is still unsteady during a rotation, which is the nature of the rotating propeller. It can be seen that the bigger distance to the rudder dampens the fluctuations of the propeller thrust coefficient K_T in Figure 3.18a.

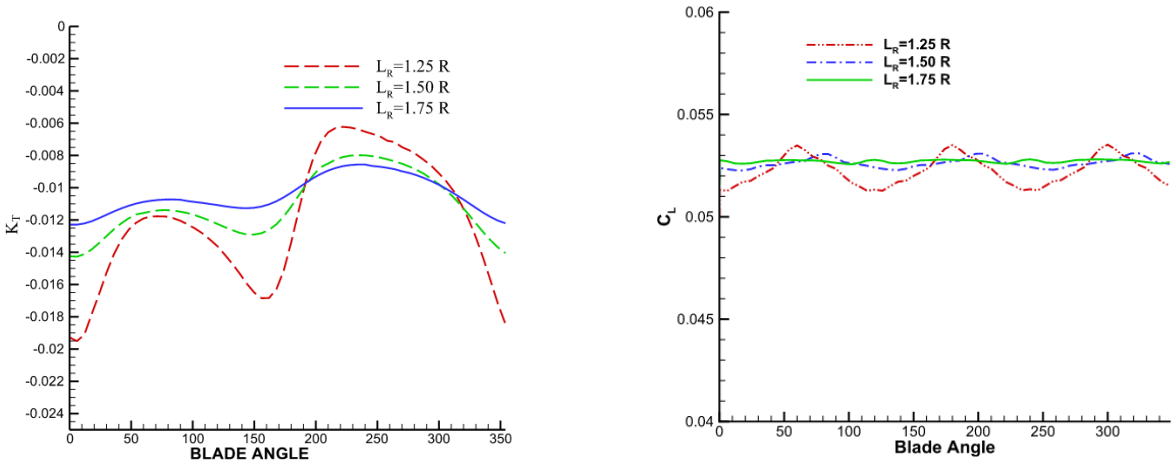

(a) Thrust coefficient for different X/D (He and Kinnas (2017))

(b) Lift coefficient for different X/D (He and Kinnas (2017))

Figure 3.18: Propeller and rudder force for different distance between propeller and rudder

L. Wang et al. (2019) showed the influence of a rudder on the wake of a propeller. The propeller-rudder configuration is simulated in open-water conditions. This was done for rudder angle of $\delta = 0°$ and $\delta = 20°$, at two different loading conditions. The rudder causes blockage of the accelerated flow behind the propeller, influencing the mean velocity field behind the propeller. In Figure 3.19, the axial velocity field is shown at the a distance of x/R=0.75 of the propeller. When the rudder angle is zero, a small reduction of the axial velocity of the flow is already observed. In Figure 3.19, the reduction in (a) and (b) is located at the centreline between the top and bottom of the propeller, at the location of the rudder. For δ=20°, the area of the propeller wake that is influenced by the rudder has increased. On the starboard side of the propeller wake a velocity deficit is showing up, due to the blockage effect, leading to an imbalanced and asymmetrical wake profile behind the propeller. Moreover, in Figure 3.19, the

comparison between two loading conditions is made. L. Wang et al. (2019) found that lighter loaded propellers are more prone to a rudder in the propeller wake. The velocity reduction as a result of the rudder angle in Figure 3.19(c), is less than in Figure 3.19(d).

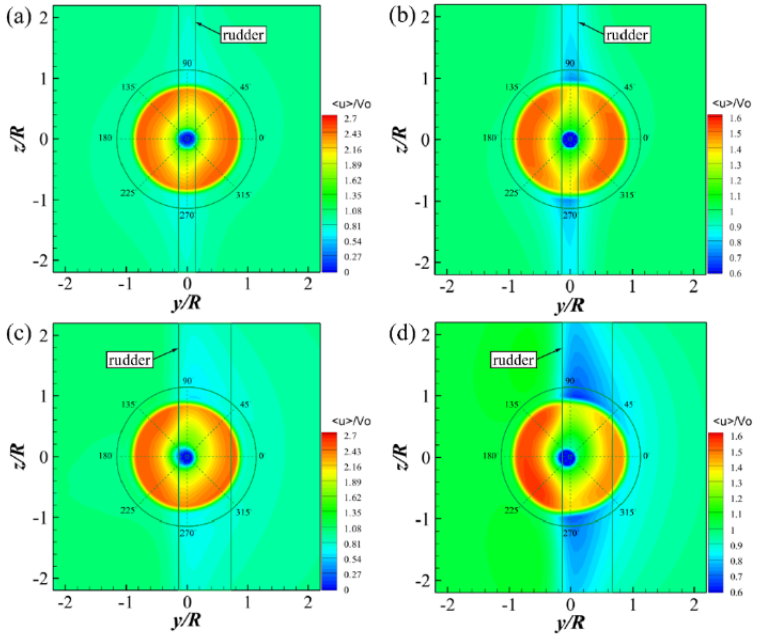

Figure 3.19: Axial velocity for a propeller before a rudder, with (a,c) $J = 0.45$, (b,d) $J = 0.71$, (a,b) $\delta = 0$ and (c,d) $\delta = 20$ (L. Wang et al. (2019))

Also, Villa et al. (2020) describes the propeller load effect. However, the method used in this paper is not able to predict detailed flow phenomena and is therefore also not able to predict rudder stall. It is observed that the thrust measured in the simulations is higher than the open water thrust. In the paper it was mentioned that the possible conclusion for the higher thrust is that the rudder interact via pressure fields instead of velocities. This could declare the accurate prediction of the rudder forces. Also the impact of the position of the propeller was investigated by Villa et al. (2020). Here it is shown that the lift coefficient is not changing for smaller rudder angles were the rudder is not affected by stall.

Lastly, the vortices coming from the propeller also face the rudder. For example, Felli (2021) show the interaction between a wing and tip vortices of the propeller. Experimentally the interaction with both sides of the rudder was investigated. Hu et al. (2024) and Hu et al. (2019) also performed numerical analysis of the interaction of these vortices with the rudder leading edge and both sides of the rudder. This interaction is certainly a problem to dive deeper into for research on propeller-rudder interaction.

3.4. Conclusion

In this section the following sub-question was answered:

Which effects of oblique flow and advance coefficient on propeller performance and wake characteristics of a propeller are already found in previous studies?

The propeller under drift is studied in several previous research studies. The flow to the propeller changes as a result of the changed direction of the inflow. A propeller in open water is only affected by this change and will show an imbalance between the top and bottom part, where the top position is the position of maximum thrust. However, behind a ship hull, the propeller is also influenced by the ship wake. This causes a shift in maximum thrust position. For twin-screwed ships, the propellers on both sides operate in a different flow regime as one of the propellers is affected by the wake of the ship, while the other propeller faces pure oblique flow. Also, the pressure and velocity profile are dependent on the advance coefficient. It was shown that the velocity behind the propeller was mixing up more for

low advance coefficients and high drift angles.

The influence of oblique flow on propeller forces and moments depends on advance coefficient. The higher J, the higher the impact of drift. The propeller forces changes periodically and non-uniform due to the non-uniformity of the inflow at the propeller plane. This introduces the problem of in-plane loads, as the propeller forces on upper and lower half and port side and starboard side of the propeller are not balanced well. This in-plane load causes vibrations of the propeller. It was also noted that the forces on the ship are also influenced by a drift angle, which is important for course keeping and manoeuvring.

Lastly, propeller-rudder interaction was shortly introduced. The propeller straightens the flow to the rudder. Therefore, the experienced drift angle by the rudder differs from the ship's drift angle. Moreover, drift angles influence the lift and drag characteristics of the propeller, but the trend remains approximately the same. The curves are shifted as a result of the drift angle. On the contrary, the lift coefficient curve changes for varying advance coefficients. The increase in lift for increasing rudder angle δ is smaller for higher J.

As the amount of experimental studies covering propellers at a drift angle is limited, this emphasizes the importance of experimental investigation of propellers in these conditions. Moreover, most research focus on medium or low advance coefficient, while in WASP conditions, J is expect to increase further, as the propeller is lighter loaded. Therefore the research question is:

What are the effects on thrust and torque generated by a marine propeller model, measured experimentally in an open water environment, under oblique flow conditions and varying loading conditions, imitating typical WASP conditions?

Following the steps outlined by the sub-questions, the research question can be answered. The combination of both experimental and numerical results enables to find both thrust and torque as wake characteristics of the propeller at drift.

4

Experimental methodology

The goal of the research is to find the effects of oblique flow on thrust and torque experimentally. This chapter describes the methodology used for the experiments. To measure this effects, an experimental set-up is constructed. The purpose of this chapter is to answer sub-question 2: *Which specific experimental set up can be used for accurately determining the thrust and torque under oblique flow and varying loading conditions?* This is done by describing the towing tank facility, the set-up, data acquisition, definitions and the measurement matrix.

4.1. Towing tank

The experiments were carried out in Towing Tank No.1 in the department of Maritime and Transport Technology, Mechanical Engineering at the TU Delft. The towing tank has a length of 142 meter and a width of 4.22 meter ("Towing tank No. 1" (2025)). The maximum water depth is 2.50 meter. The carriage of the towing tank has a maximum speed of 7.0 m/s. Moreover, a wavemaker is installed in the towing tank. This wavemaker can generate waves with wavelengths of 0.30 to 6.00 meter.

4.2. Experimental set-up

The propeller that is tested needs to be mounted to the carriage and also be driven. The propeller open-water dynamometer (POD or gondola) is used to perform these open-water tests. This gondola is manufactured by MARIN by order of TU Delft. It consists of a strut profile and a propeller shaft.

The gondola can be equipped with two strut profiles: A short strut and a longer strut. The long strut should be mounted to the gondola when tests are performed in the towing tank. The shorter strut is manufactured to use the gondola in the cavitation tunnel. When mounting the strut to the gondola some checks needs to be done. Firstly, the O-rings need to be checked and replaced if those are damaged. These rings ensure that the gondola is watertight. Moreover, it is important that the cables, that are used for both power supply and transferring the signal, are pulled carefully through the strut. Finally, the bolts need to be lubricated and the strut can be placed on the gondola, by tighten the bolts crosswise. The strut ensures that the propeller can be submerged according to the ITTC guidelines as shown in Figure 2.9. In Figure 4.1, a drawing of the gondola is shown.

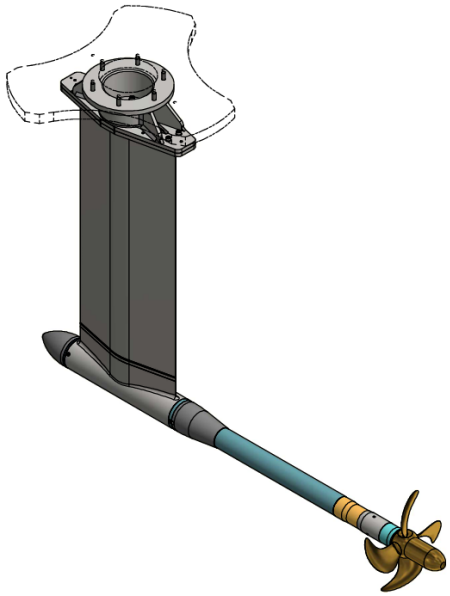

Figure 4.1: Drawing of the gondola (MARIN)

The gondola can reach rotational speeds up to 2400 rpm. The minimum rotational speed is 5 rpm, which can be used for zero load measurements. The maximum torque that the gondola can deliver is 12 Nm at the maximum rotational speed of 2400 rpm. Moreover, the gondola is equipped with an encoder, which can be used as input for PIV measurements. These pulses can be used to ensure the position of the propeller blades at a certain time. The encoder gives 7200 pulses per rotation.

The gondola is mounted on the HexaPod. On the gondola's strut, a connecting piece is placed, which is needed to tighten the gondola to the HexaPod. This connection is fastened to the gondola before connection to the HexaPod, as this is easier during hoisting the gondola on the carriage. Here again, it is important to pull the cables through this connection, such that those can be reached after connecting the gondola to the HexaPod. The HexaPod is a device that can position an object that is mounted to it. With the HexaPod the gondola can be positioned under the right drift angle. Moreover, the minimum submergence of the propeller can be ensured by adjusting the z-coordinate. The HexaPod is attached to the carriage using beams. The hexapod can be seen on the left-hand of Figures 4.2 and 4.3.

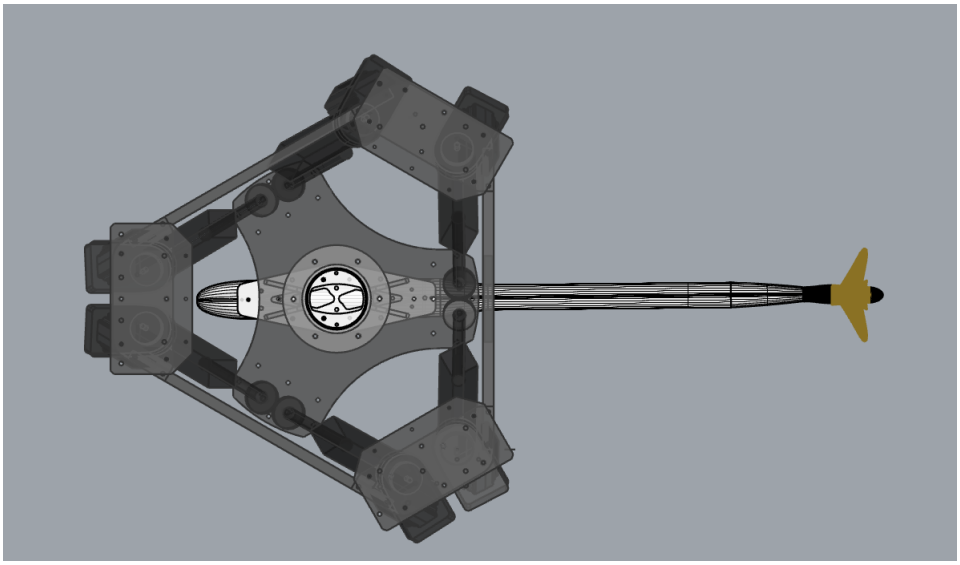

Figure 4.2: Drawing of top-view of the experimental set-up

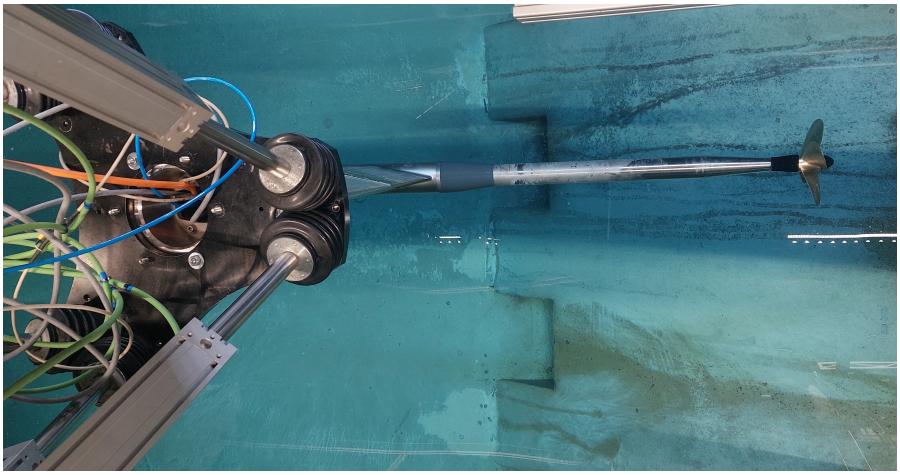

Figure 4.3: Top-view of the experimental set-up

In the settings of the Hexapod, the centre of rotation was set at the position of the propeller. This means that the propeller stays at the same position when a drift angle is applied with the HexaPod. The direction of the gondola is opposite to that of conventional open-water tests. In most common set-ups, the propeller is pushed by the POD. In other words, the propeller is upstream of the gondola. This configuration ensures that the propeller is facing undisturbed inflow and is also called pulling configuration. However, in this measurement campaign the propeller is in a pushing configuration, which means that the strut and the shaft of the gondola are upstream the propeller. Initially, both pulling and pushing configuration were planned to be measured. However, this brings another challenge, as the complete construction below the carriage should be turned around. Moreover, the propeller can not be reached when the gondola is turned, due to the increasing depth of the towing tank close the the end. Therefore, based on the limited available time in the towing tank, the choice has been made to test in pushing configuration only. In straight ahead condition, the strut is not producing lift as the flow around the strut is symmetrical. Therefore, the influence of the strut on the propeller is minimal in that case.

The propeller is mounted on the shaft. The shaft is driven by two permanent magnet engines, which are connected in parallel. To get this engines working, they should be connected to the power net. A control box is used to deliver the power. The cables from the gondola should be connected to this box. Firstly, an circular connector (at the end of the orange cable) connects the motor to the box. A grey cable, also with a circular connection, is used for feedback from the engines. The encoder can be connected to a computer where the program that needs this as an input is running. There is also an emergency button that should be placed on the carriage. This button can stop the propeller rotating, when needed for safety reasons, without damaging the force transducer.

The permanent magnet engines are controlled by the Servo Drive. To connect the computer to the gondola, the drive interface RS232 should connect the box with this computer. This can be done by using a null modem cable with SUB-D9 connections on each side. When this cable is properly connected, the Servo Drive application can be used.

In the Servo Drive, the set-up of the gondola's engines can be adjusted. This consists for example of the motor settings and the loops for current, velocity and position of the propeller. Moreover, the monitor shows the loads, voltage and power of the engines. Also, the rotational speed of the shaft can be monitored during a run. The terminal is used to set a certain rotational speed. After enabling the shaft to rotate, the command *'J 50'* can be used to set a rotational speed of 50 rpm. For clockwise rotation of the propeller, a minus needs to be added.

The propeller used for the experiments is a propeller that is similar to the Wageningen B4-70 propeller. This propeller is provided by MARIN and it is made out of bronze. The characteristics of the propeller are given in Table 4.1.

Table 4.1: Characteristics of the propeller model

Diameter D [m]	0.21739
Number of blades Z [#]	4
Expanded Blade Area Ratio A_e/A_0 [-]	0.669
Pitch at 0.7R $P_{0.7}$	0.21748
Pitch ratio $P_{0.7}/D$	1.000
Pitch at blade root [m]	0.19213
Pitch at blade tip [m]	0.21661
Skew angle [°]	7.29
Blade rake [m]	0.01528

The propeller is a right-handed propeller with a fixed pitch. This propeller was mounted at the end of the gondola's shaft. However, the POD is not specifically manufactured for this propeller. This causes a gap between the flow cap of the gondola and the propeller. To ensure an as uniform inflow as possible an additional part is needed to cover this gap. The force transducer is also positioned here, and should obviously be protected from influence of the incoming water. Moreover, an end-cap was missing, which is also needed for smooth stream around the propeller. These parts were 3D printed, and are shown in Figure 4.4. They can also be seen in Figure 4.3, as the black parts before and behind the propeller.

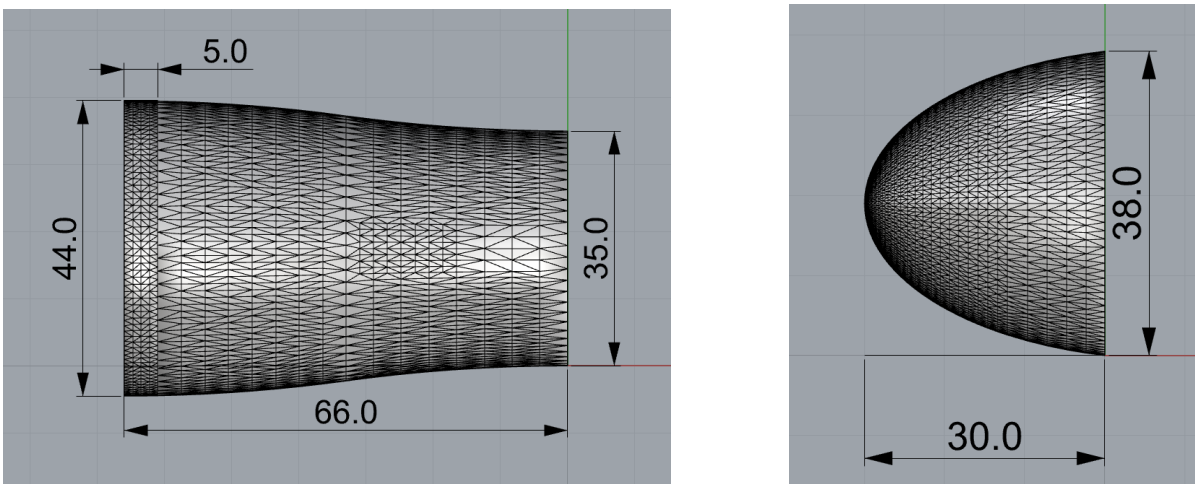

(a) Additional part behind flow cap

(b) End-cap behind the propeller

Figure 4.4: Additional 3D printed parts

The POD is equipped with a force transducer to measure the thrust and torque of the propeller. The force transducer used is of the type 232S, which is shown in Figure 4.5. This force transducer needs to be placed at the end of the shaft. Firstly, the rings inside the shaft need to be lubricated with Vaseline, to ensure that these rings keep the gondola watertight. Thereafter, the force transducer can be hold before the shaft at the right position, using the pin that ensures the right orientation of the transducer. Lastly, the bolds should be tighten crosswise, until the transducer is fixed. The 3D-printed stream cap can be placed now.

Figure 4.5: Force transducer type 232S

This force transducer is intended for experiments with small propeller models, like the propeller used in this campaign. The maximum thrust that can be measured safely without damaging the force transducer is 430 N, whilst the measurement range for thrust is 340 N. The maximum measuring range for torque is 14 Nm and the safe load range is for torque up to 18 Nm. These maxima are one of the requirements to take into consideration for the conditions that will be tested. Calibration factors were obtained by tests performed by MARIN. The formulas following from this calibration can be found in equations 4.1 and 4.2.

$$\begin{aligned} T_m &= c_1 \cdot T_0 - T_{correction} \\ T_{correction} &= 0.062 \cdot Q_m + 0.036 \cdot Q_m^2 \end{aligned} \tag{4.1}$$

$$Q_m = c_2 \cdot Q_0 \tag{4.2}$$

Here, T_m and Q_m are the measured thrust in N and torque in Nm respectively. T_0 and Q_0 are the signals of thrust and torque in mV/V. For the thrust, there is also a correction needed. This is caused by the fact that some thrust is measured when pure torque is applied. This means that the thrust measured by the force transducer is slightly to high when there is also torque applied. For this reason, the correction is subtracted from the measured value of the thrust. c_1 is the calibration constant for thrust in N/(mV/V). This constant is equal to 214.164. c_2 is the calibration constant for thrust in Nm/(mV/V). This constant is equal to 8.839. According to calibration report of MARIN, there is no interaction between the thrust and torque signals when pure thrust force is applied. Therefore, no correction is needed for Q_m.

4.3. Data acquisition

The measured signals of the force transducers are firstly amplified by the signal amplifier (PICAS). The force transducer is connected to the signal amplifier by cables that can be reached at the opening at the top of the gondola. This device shows a signal of 5 V for each mV/V. To determine thrust and torque, calibration factors c_1 and c_2 now can be multiplied by 0.2 (mv/V)/V. This gives calibration constants that directly transfer the amplified measured signal to Newton and Newton-meter: $c_1 = 42.8328$ N/V and $c_2 = 1.7678$ Nm/V.

As the signals measured by the amplifier are arbitrary and not equal to zero, when zero load condition, a zero run is performed before each run. This is done before each run, because this zero load signal also varies during the day. Moreover, this signal is slightly changing when adjusting the z-coordinate of the HexaPod. This is probably caused by the fact that the cables are more stretched when the gondola is positioned lower. The zero runs are performed at a rotational speed of 7 rpm. This ensures clearance from the gondola's lower limits and maintains consistency with the parameters used in the calibration report. The signal of the signal amplifier is used to sample and digitalise the signal by the data acquisition system. The data is sampled with a rate of 1000 Hz, so each second 1000 data points are obtained.

4.4. Definitions

The coordinate system used during the experiments is shown in Figure 4.6. Note that the most general symbol for a yaw angle is not used here, as drift angle was already noted by β throughout the whole project. Therefore β_m is introduced, which is the drift angle of the model.

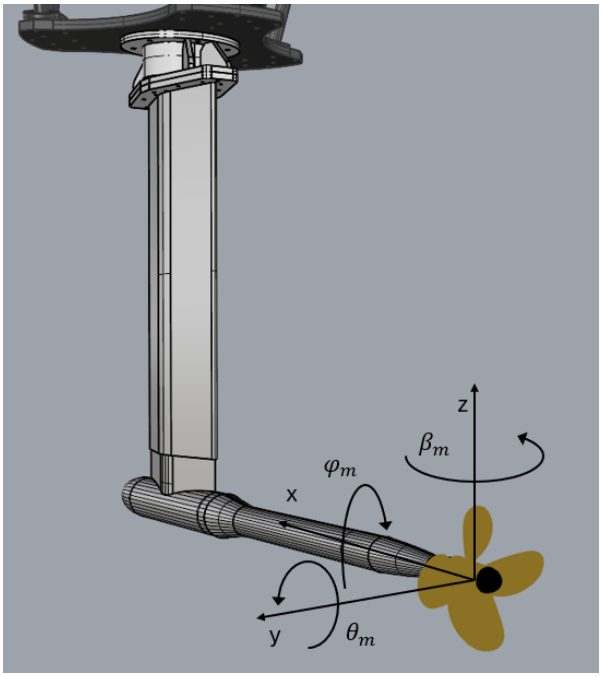

Figure 4.6: Coordinate system

As described, the centre of rotation of the HexaPod is located at the origin of this coordinate system. The inflow is in this configuration in the negative x-direction. For negative β_m, the propeller is on the left side of the gondola, while for positive β_m, the propeller in on the right side of the gondola.

4.5. Measurement matrix

The measurements that are performed need to cover at least varying drift angles for different advance ratios, so that the research question can be answered. As WASP conditions are of interest, the drift angles that will be tested will not exceed 15°. Moreover, the most critical advance coefficients J are the high values, as this loading conditions correspond to propellers that are lightly loaded, which is the case when thrust is partially generated by WASP devices.

Since the thrust and torque characteristics of the propeller are unknown, thrust and torque will be measured for as much loading conditions as possible, including low J. To decide which carriage speed V_A and rotational speed n_p are used, it is firstly important to account for the limits of the set-up. The upper and lower limit of the gondola of 5 rpm and 2400 rpm respectively is one of those limits. This excludes some combinations of V_A and n_p values. Moreover, the Reynold's number must exceed $2.0 \cdot 10^5$, to obtain trustworthy results (International Towing Tank Conference (2021)). This requirement shows that the carriage speed should be at leat 1.5 m/s. Lastly, the force transducer may not exceed its limits, and therefore an estimation of the forces needs to be made. Those are estimated using the known open-water diagram of the similar Wageningen B4-70 propeller (Bernitsas et al. (1981)). The estimated thrust and torque showed that a carriage speed of 1.5 m/s has the best trade-off between number of advance coefficients that can be measured and a sufficient Reynold's number. In Appendix A (see Chapter 8) the results for all combinations are shown. Based on these four criteria, the parameters for the measurements are chosen.

Also, the influence of Reynold's number for some advance ratios will be measured. This is done by increasing the carriage speed. Due to the higher speed, the rotational speed of the propeller is also higher to measure at the same advance coefficients. However, this measurements can only be done for some higher advance ratios J, as thrust and torque are higher in this case. Due to the limitations of the force transducer and the gondola's maximum rotational speed, it is not possible to measure for low J. The carriage speed for these runs is 3.5 m/s. In Table 4.2 the Reynolds number for each run is given.

Table 4.2: Comparison of Reynolds number of high and low speed measurements

V_A [m/s]	1.5	3.5
J [-]	$Re_{0.7}$ [-]	$Re_{0.7}$ [-]
0.4	$6.29{\cdot}10^5$	-
0.5	$5.07{\cdot}10^5$	-
0.6	$4.27{\cdot}10^5$	$9.97{\cdot}10^5$
0.7	$3.71{\cdot}10^5$	$8.65{\cdot}10^5$
0.8	$3.29{\cdot}10^5$	$7.68{\cdot}10^5$
0.9	$2.97{\cdot}10^5$	$6.93{\cdot}10^5$
1.0	$2.72{\cdot}10^5$	$6.34{\cdot}10^5$
1.1	$2.51{\cdot}10^5$	$5.87{\cdot}10^5$

As shown above, the Reynolds number of the case with carriage speed 3.5 m/s is more than twice the Reynolds number for 1.5 m/s. This may result is more accurate measurements in the runs with high carriage speed.

In Table 4.3, the full overview of all measurements that will be performed are given. For all cases, the influence on both positive as negative drift angle will be measured.

Table 4.3: Overview of the measurement matrix

V_A [m/s]	J [-]	0.4	0.5	0.6	0.7	0.8	0.9	1.0	1.1
1.5	n_p [rpm]	1035	828	690	591.4	517.5	460	414	376.4
3.5	n_p [rpm]	-	-	1610	1380	1207.5	1073.3	966	878.2
1.5, 3.5	β_m	0, $\pm$5, $\pm$10, $\pm$15							

During the tests, the physical parameters as in Table 4.4 were attained. The temperature is an estimation, on which water density ρ_w and kinematic viscosity ν are based.

Table 4.4: Conditions during experiments

Water depth [m]	2.16
Tank width [m]	4.22
Water temperature T [°C]	17.0
Water density ρ_w [kg/m³]	998.8
Kinematic viscosity ν [m²/s]	$1.0811 \cdot 10^{-6}$
Gravitational acceleration g [m/s²]	9.81

5

Experimental results

The experiments are carried out with the set-up described in chapter 4. The results will be presented in this chapter. The goal of this chapter is to provide a large part of the answer to research question:

What are the effects on thrust and torque generated by a marine propeller model, measured experimentally in an open-water environment, under oblique flow conditions and varying loading conditions, imitating typical WASP conditions?

Moreover, an answer is formulated to the third sub-question:

How does a wing profile upstream the propeller influence the performance of the propeller in oblique flow compared to open water conditions?

The results of the measurement campaign are presented first as mean values. Thereafter, the uncertainty of the experiments is determined. Lastly, a frequency analysis is done on the time signals. The results will be shown mostly for three selected cases, which cover high-loading, medium loading and light loading conditions. These are respectively the cases with advance coefficient $J = 0.5$, $J = 0.8$, $J = 1.0$. All other measured values can be found in Appendix B in chapter 9.

During the measurements some problems were encountered, which will be explained first before showing the actual results. Firstly, the gondola was not able to reach all desired rotational speeds. This was caused by settings in the Servo Drive. The gondola's engines reached a set limit of the current, which enabled the shaft to reach requested rotational speed. For the carriage speed of 1.5 m/s this occurred for $J = 0.4$. Here the propeller rotated with 969.8 rpm on average, whilst this should be 1035 rpm. This corresponds to an advance coefficient of $J = 0.427$. This point is used for each drift angle β_m, such that no data points are lost. The same problem occurred for $J = 0.6$ and $J = 0.7$ for $V_A = 3.5$ m/s. Here 1610 rpm and 1380 rpm were the intended rotational speeds respectively. However, in both cases the maximum reachable speed was 1259.1 rpm instead, which gives $J = 0.77$. In this case, the measurements for those advance ratios were cancelled in oblique flow condition, as the difference with $J = 0.8$ is minimal.

Also, the 3D-printed end-cap and the additional part of the flow cap gave some problems with the signals once. Here, the signal showed variations with two peak that repeated with the same frequency as the shaft frequency. This could already be seen during the zero run, where zero load is applied to the propeller. The most probable cause for this is that the hub touched one of those parts, which then obviously repeats each revolution. This was probably due to deformation of the parts due to the temperature of the water. This problem was fixed, by slowly tighten and loosen the end-cap of the propeller. Afterwards, the measured signal in the zero run was again the same as before this problem was encountered, showing that the propeller did not touch these parts anymore.

5.1. Mean thrust and torque

To extract the mean thrust and torque values, the measured signal needs to be adjusted. Each run is performed by first starting the propeller. When the propeller has reached the desired rotational speed, the run is started and data acquisition also starts. Thereafter, the carriage start to ride, until the end of the towing tank. Thrust and torque therefore vary during the measurement, since they are highly depended on carriage speed. Therefore it is not possible to use the full time signal, so a segment where the carriage speed is at the required value is selected. An example of the selection of such a segment is shown in Figure 5.1.

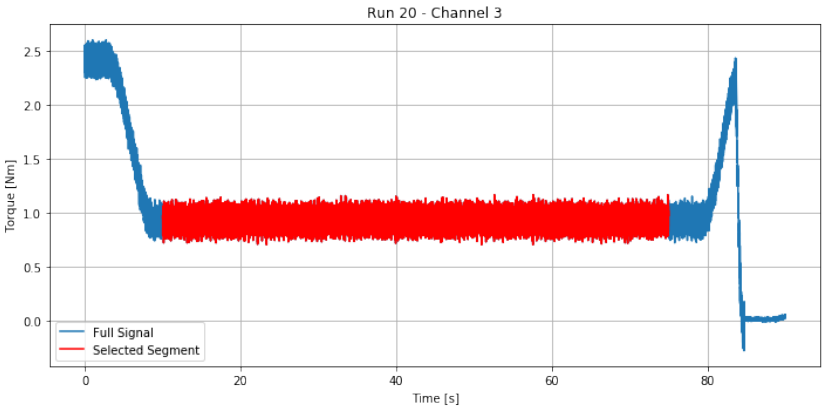

Figure 5.1: Example of selected segment from the torque signal

The torque is high at the start, as this represents bollard pull condition. At the end the propeller is stopped, as the torque generated falls down to zero. The mean of the measured signals is determined based on a fixed length of the time frame. For $V_A = 1.5$ m/s, this time frame was 65 seconds. With a sampling rate of 1000 Hz, this gives 65000 data points each run. Repeat runs were also performed for some cases. For 1.5 m/s the amount of data points is higher than for 3.5 m/s as the total time to reach the end of the towing tank is lower. Therefore, 20000 data points were measured per run for the higher carriage speed, corresponding to a segment length of 20 seconds.

The mean values of thrust coefficient K_T, torque coefficient K_Q, and open-water efficiency η_0 are calculated using formulas 2.3, 2.4 and 2.5. Here, also the mean value of the rotational speed n_p is used to obtain one single value.

5.1.1. Straight ahead condition

As stated before, the propeller is similar to a Wageningen B4-70 propeller. Therefore, to check if measured thrust and torque are close to these values, a comparison with this propeller is made. The Wageningen B4-70 that is used for comparison, has the same propeller diameter and also the pitch ratio is the same. In Figure 5.2, the known K_T, $10K_Q$ and η_0 fit-lines for this propeller are shown. The data points shown represent the mean of the measured values during them measurement.

A first comparison shows good agreement of the measured data with the known propeller characteristics of the Wageningen B4-70 propeller. To demonstrate the difference of each data point with the propellers characteristic, a comparison between the mean measured thrust and torque coefficient and the known values for the Wageningen B4-70 propeller are shown in Table 5.1, including the relative difference.

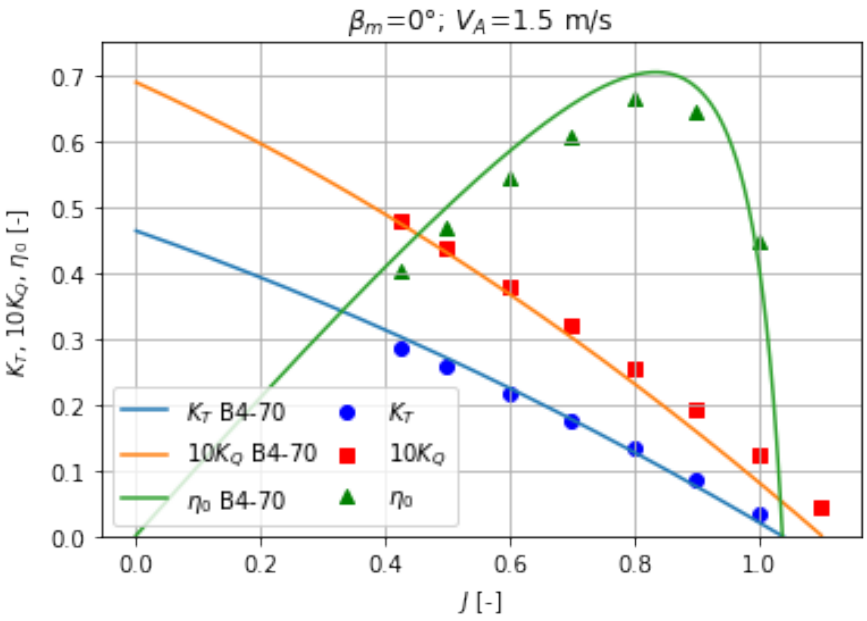

Figure 5.2: Comparison of results for $\beta_m = 0°$, $V_A = 1.5$ m/s to open-water characteristics of the Wageningen B4-70 propeller

Table 5.1: Comparison of measured mean values to Wageningen B4-70

J [-]	Wageningen B4-70		Propeller model		Difference [%]	
	K_T [-]	$10K_Q$ [-]	K_T [-]	$10K_Q$ [-]	K_T [-]	$10K_Q$ [-]
0.43	0.3133	0.4889	0.2843	0.4785	-9.26	-2.13
0.50	0.2701	0.4299	0.2581	0.4380	-4.44	1.88
0.60	0.2248	0.3674	0.2163	0.3793	-3.78	3.24
0.70	0.1772	0.3013	0.1745	0.3198	-1.52	6.14
0.80	0.1274	0.2316	0.1333	0.2553	4.63	10.23
0.90	0.0753	0.1584	0.0868	0.1934	15.22	22.10
1.00	0.0211	0.0817	0.0348	0.1235	64.92	51.16
1.10	-0.0354	0.0014	-0.0193	0.0438	-45.48	3028.57

In the figure and table above it is observed that the the experimental data and the fit-lines of the B4-70 propeller does not decrease at the same rate. For K_T, the measured values are lower for low J, while these are higher at high advance ratios. For K_Q, a similar trend can be seen: The measured values are close to the Wageningen B4-70 propeller for high loading conditions, whilst the differences increase for increasing J. This also declares the lower open-water efficiency of the propeller used in the experiments, since the torque is almost higher on each point. Only at the highest advance ratio considered, η_0 is higher than that η_0 of the Wageningen B4-70 propeller, which is caused by the relatively higher thrust. The fact that both propellers slightly differ is no surprise, as this propellers are similar but not exactly the same. However, this comparison shows that there is a good agreement between the measured and the already known values. Therefore, it can be assumed that the influence of the strut in front of the propeller is indeed minimal in straight ahead condition.

5.1.2. Influence of a drift angle

Knowing the characteristics of the propeller in straight ahead conditions enables us to compare this measurements to oblique inflow conditions. In Chapter 4, it was already described that the angles considered are 5, 10 and 15 degrees. These measurements are performed for both positive and negative drift angles. The results of this measurements are shown in Figure 5.3 for three different advance

ratios.

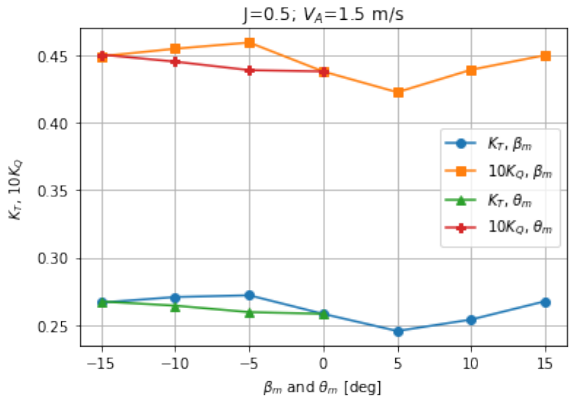

(a) K_T and $10K_Q$ for pitch and drift angles for J=0.5, V_A=1.5 m/s

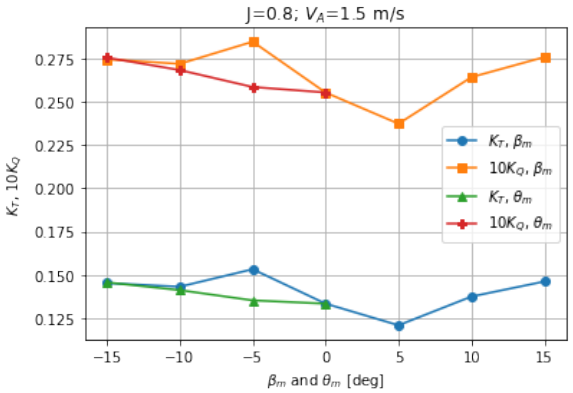

(b) K_T and $10K_Q$ for pitch and drift angles for $J = 0.8$, $V_A = 1.5$ m/s

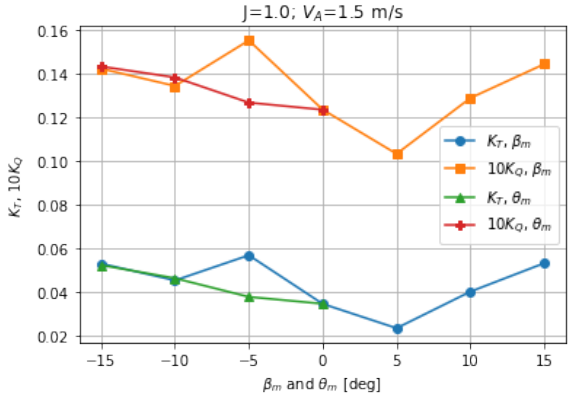

(c) K_T and $10K_Q$ for pitch and drift angles for $J = 1.0$, $V_A = 1.5$ m/s

Figure 5.3: K_T and $10K_Q$ for pitch and drift angles

From Figure 5.3 is can be concluded that the chosen configuration, with the gondola's strut upstream of the propeller, influences the thrust and torque of the propeller. While this effect was not observed for $\beta = 0°$, this influence is clearly visible for drift angles. The effect is the highest for the smallest drift angle. Both thrust as torque have a high peak for $\beta_m = -5°$ and a trough for $\beta_m = 5°$. Since this deviations are clearly an effect of the perturbations of the inflow by the gondola, some additional runs are performed with the strut at zero drift angle, but with a negative pitch angle. This experiments were performed for the same combinations of J and n_p as before. With a negative pitch angle, the propeller is mostly below wake of the strut of the gondola. These measurements were performed for $\theta_m = -5$ °, $\theta_m = -10°$ and $\theta_m = -15$ °.

The peaks and troughs in Figure 5.3 can be explained by the wake of the strut. The incoming flow first encounters the strut profile of the gondola. When $\beta_m = 0°$, the flow around this profile is axisymmetric. However, at drift angles, this axisymmetric flow disappears. In Figure 5.4, it can be observed that the flow around the strut is not symmetrical. This introduces vortices coming from the strut, which propagate downstream to the propeller. For negative drift angle, both thrust and torque show an increase. This increase can be declared using the vector representation of the velocities. The angle of attack of the propeller has increased on this local propeller position.

For positive drift angle, the effect of these vortices is opposite. This can be declared by the direction of rotation of the propeller, which is obviously the same for all measurements. At this position in the strut's wake, the propeller generates lower thrust and torque. For increasing β_m, this effect of amplifying or lowering the propeller forces is less observable and seems to disappear for the highest drift angles. The propeller is less or not affected by the gondola for these angles, as the propeller is placed outside

the wake of the strut due to the rotation of the gondola.

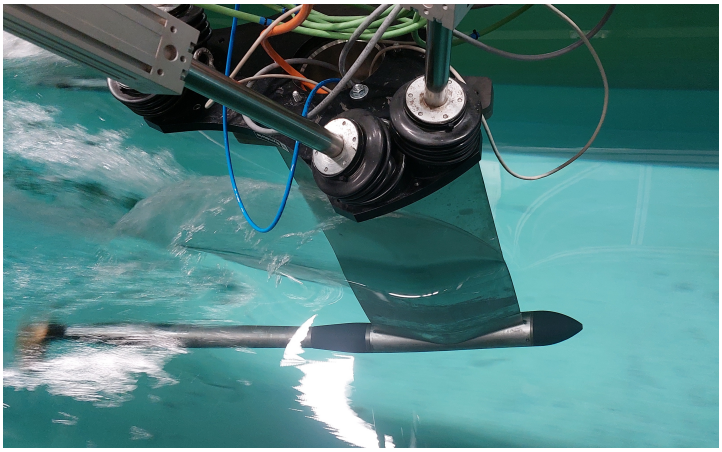

Figure 5.4: The gondola at a drift angle during a run, showing the asymmetrical flow around the strut

The results of the propeller at a pitch angle show a different trend. For increasing pitch angle θ_m, both thrust and torque increase. This trend is more in line with previous research, as propeller thrust and torque increase for increasing drift angle. This observation enhances the assumption that the strut causes the measured forces to be too high or low in the case with a drift angle. Moreover, the measurements show that the influence of the strut is also depended on propeller loading. This difference is the best visualised at $\beta_m = -10°$. At this angle, the strut still has an influence on both K_T and $10K_Q$. Both values are still higher than for $\theta_m = -10°$, which is also the case at $\beta_m = 5°$. One of the possible causes for this is the fact that the propeller rotates faster at lower J. Due to this higher rotational speed, the propeller is accelerating more of the incoming fluid than a slower rotating propeller. As a result, the flow that is attracted by the propeller is from a larger region including the part that is influenced by the strut's wake. It can be seen in Figures 5.3a, 5.3b and 5.3c that this effect is reducing for increasing advance coefficient J.

However, it should be noted that this set-up is still not a perfect replacement of a pulling propeller, which experiences uniform inflow. The propeller is still slightly in the wake of the strut. Moreover, an influence of the shaft on the propeller inflow is introduced. Both the influence of the shaft and the influence of the strut influences will show up at the zero degrees position of the propeller plane. In further analysis of the results, the measurements with pitch angle will be considered. This is because it is proved that the measured values in pitch condition are less affected by the strut than with a drift angle.

5.1.3. Influence of Reynolds number

The Reynolds number at $V_A = 1.5$ m/s is close to the lower limits in some cases. Therefore, some tests are performed at an higher Reynolds number. This was done by increasing both carriage speed, which increased to 3.5 m/s, and rotational speed of the propeller, corresponding to the carriage speed to measure at the same J. In table 5.2, the mean value of K_T are shown for all pitch angles θ_m at both speeds.

Table 5.2: Comparison of mean values of K_T between measurements with varying Reynolds number

	V_A = 1.5 m/s				V_A = 3.5 m/s			
J[-] \ θ_m[deg]	0	5	10	15	0	5	10	15
0.80	0.1335	0.1354	0.1413	0.1458	0.1197	0.1234	0.1307	0.1373
0.90	0.0869	0.0885	0.0966	0.1005	0.0761	0.0791	0.0881	0.0950
1.00	0.0349	0.0381	0.0466	0.0526	0.0297	0.0348	0.0430	0.0508
1.10	-0.0193	-0.0178	-0.0075	-0.0015	-0.0192	-0.0149	-0.0073	0.0025

As can be seen, both cases show the same trend. Thrust is increasing for increasing pitch angle. However, the values show some differences. Measured thrust is slightly higher for lower Reynolds number. The differences are less than a percent up to 14.7%, besides $J = 1.10$ at 15 degrees, as this difference as a percentage is enormous, as the values are really small.

In table 5.3, the mean value of $10K_Q$ are shown for all pitch angles θ_m at both speeds.

Table 5.3: Comparison of mean values of $10K_Q$ between measurements with varying Reynolds number

	V_A = 1.5 m/s				V_A = 3.5 m/s			
θ_m[deg] / J[-]	0	5	10	15	0	5	10	15
0.80	0.2557	0.2588	0.2686	0.2759	0.2661	0.2709	0.2811	0.2910
0.90	0.1936	0.1947	0.2050	0.2111	0.2039	0.2079	0.2205	0.2298
1.00	0.1236	0.1268	0.1383	0.1433	0.1342	0.1418	0.1542	0.1650
1.10	0.0439	0.0465	0.0611	0.0668	0.0582	0.0657	0.0783	0.0928

Here, it is observed that torque is higher for the high Reynolds number. Here the differences are between 4% and 15%, besides $J = 1.10$. There the torque coefficient is 30-40% higher.

5.2. Uncertainty

All values shown above are mean values of the measured signal. These values are not the exact values, as several errors in the experiments can be made, which cause the values to deviate from the exact value. There are two types of errors made during an experiment: precision error and bias error. Precision errors are caused by the measured signal, and can be determined using statistical analysis. Bias errors originate from systematic deviations from the actual measured case. For this type of error, only estimates can be made.

5.2.1. Precision error

The distribution that applies to experimental measured quantities is the Student's t-distribution (Steimel and Humbolt (2025)). This distribution shows that a measured quantity with the Student's t-distribution has 95% confidence interval for t_{95}, which is equal to 1.960. This means that for the measured signals, 95% of the data points are inside the upper and lower limit defined by adding and subtracting $t_{95} \cdot \sigma_x$ from the mean value. In the uncertainty analysis below, this value is rounded to 2 for t_{95}. Therefore, the upper-bound given by $\overline{x} + 2 \cdot \sigma_x$ and the lower-bound given by $\overline{x} - 2 \cdot \sigma_x$ will contain 95% of all data points. Here, $\overline{x}$ is the mean value of variable x and σ_x is the standard deviation of variable x. The standard deviation of a data set is calculated with formula 5.1.

$$\sigma_x = \sqrt{\frac{\sum_i^N (\overline{x} - x_i)^2}{N}} \tag{5.1}$$

x_i is individual data point i, and N is the sample size, which is the total amount of data points. The standard deviation has the same units as parameter x Using this standard deviation, the total uncertainty of any parameter can be determined using formula 5.2.

$$U_x = 2 \cdot \sigma_x \tag{5.2}$$

Here, U_x is the uncertainty of variable x, having the same units as this variable. As it is only possible to determine the uncertainties of measured quantities with this method, the propagation of the errors of these parameter to the parameters of interest should be calculated.

For advance coefficient J, there are three variables that influence its uncertainty caused by precision errors: propeller diameter D_p, rotational speed n_p and advance velocity V_A. The contribution of the

propeller diameter D_p to the the precision error of J is assumed to be zero, as the dimensions of the propeller are known and do not vary during the experiments. Therefore, the advance coefficient is only dependent on advance speed V_A and propeller rotational speed n_p. The amount the advance ratio is changed by a change in one of those parameters is called sensitivity. The sensitivity of a parameter to changes in another parameter can be determined using the partial derivatives. The partial derivatives of J to both V_A and n_p can be found in formulas 5.3 and 5.4 respectively.

$$\frac{\partial J}{\partial V_A} = \frac{1}{n_p \cdot D_p} \tag{5.3}$$

$$\frac{\partial J}{\partial n_p} = -\frac{V_A}{n_p^2 \cdot D_p} \tag{5.4}$$

To obtain a value for the sensitivity, the mean values of the parameters in these equations are filled in. Using the sensitivities the total uncertainty of J can be calculated using formula 5.5.

$$U_J = \sqrt{\left(\frac{\partial J}{\partial V_A}\right)^2 \cdot U_{V_A}^2 + \left(\frac{\partial J}{\partial n_p}\right)^2 \cdot U_{n_p}^2} \tag{5.5}$$

The uncertainty of n_p is directly derived from the measured signals and therefore differs for each case. However, the carriage speed is not sampled during the measurements. Therefore, an approximation needs to be made. Based on the experiments done by Struijk (2015), the variations of V_A are estimated to be $\pm$0.001 m/s. From formula 5.3 and 5.4 it can be found that the the sensitivity is different for each advance coefficient due to the dependency to n_p.

For the thrust coefficient K_T, the same procedure can be followed. Firstly, the partial derivatives are derived from formula 2.3. These expressions for the sensitivity are given in formulas 5.6 and 5.7. As the temperature is only estimated, the fluctuations of temperature are not known. The temperature does affect the density of the water ρ_w. For fluctuations of the water temperature of less then 1.0°C (Struijk (2015)), ρ_w varies with a maximum of 0.02% (Paar (2025)). Therefore, the effects of temperature fluctuations is ignored during this analysis.

$$\frac{\partial K_T}{\partial T} = \frac{1}{\rho \cdot n_p^2 \cdot D_p^4} \tag{5.6}$$

$$\frac{\partial K_T}{\partial n_p} = -2 \cdot \frac{T}{\rho \cdot n_p^3 \cdot D_p^4} \tag{5.7}$$

From these sensitivities, the total uncertainty of K_T is given by formula 5.8

$$U_{K_T} = \sqrt{\left(\frac{\partial K_T}{\partial T}\right)^2 \cdot U_T^2 + \left(\frac{\partial K_T}{\partial n_p}\right)^2 \cdot U_{n_p}^2} \tag{5.8}$$

For K_Q, the steps are exactly the same as for K_T. The sensitivities are given in formulas 5.9 and 5.10.

$$\frac{\partial K_Q}{\partial Q} = \frac{1}{\rho \cdot n_p^2 \cdot D_p^5} \tag{5.9}$$

$$\frac{\partial K_Q}{\partial n_p} = -2 \cdot \frac{Q}{\rho \cdot n_p^3 \cdot D_p^5} \tag{5.10}$$

The total uncertainty of K_Q, is calculated using 5.11.

$$U_{K_Q} = \sqrt{\left(\frac{\partial K_Q}{\partial Q}\right)^2 \cdot U_Q^2 + \left(\frac{\partial K_Q}{\partial n_p}\right)^2 \cdot U_{n_p}^2} \tag{5.11}$$

In Table 5.4 the total uncertainty for J, K_T and K_Q as a result of precision errors are shown. Also the contribution of the parameters influencing this precision error are shown here.

Table 5.4: Uncertainties and contribution to total uncertainties, for θ_m=0° and V_A=1.5 m/s

J [-]	$U_J[-]$	$U_{V_A}[\%]$	$U_{n_p}[\%]$	$U_{K_T}[-]$	$U_T[\%]$	$U_{n_p}[\%]$	$U_{K_Q}[-]$	$U_Q[\%]$	$U_{n_p}[\%]$
0.43	0.0038	0.55	99.45	0.0106	76.92	23.08	0.0014	61.39	38.61
0.50	0.0053	0.39	99.61	0.0096	66.72	33.28	0.0019	76.79	23.21
0.60	0.0078	0.26	99.74	0.0104	70.94	29.06	0.0024	83.22	16.78
0.70	0.0104	0.20	99.80	0.0139	86.20	13.80	0.0034	92.14	7.86
0.80	0.0140	0.14	99.86	0.0151	90.43	9.57	0.0040	94.93	5.07
0.90	0.0180	0.11	99.89	0.0202	97.04	2.96	0.0058	98.21	1.79
1.00	0.0229	0.08	99.92	0.0245	99.57	0.43	0.0093	99.63	0.37
1.10	0.0272	0.07	99.93	0.0318	99.91	0.09	0.0144	99.98	0.02

For the advance ratio, it can be seen that almost the full uncertainty can be ascribed to the uncertainty of the rotational speed. The influence of the small fluctuations in advance velocity are ignorable for J. An increasing uncertainty is observed for U_J. This is caused by the fact that the standard deviation of the propeller is almost equal for all advance ratios, and is about 4.5 rpm. The total uncertainty of n_p increases, when the rotational speed is lower and the standard deviation remains the same. This can be explained by the sensitivity $\frac{\partial J}{\partial n_p}$. This sensitivity increases for decreasing n_p, as the rotational speed squared is in the denominator, since U_{n_p} stays almost constant, U_J increases. The sensitivities also explain why the share of U_{V_A} decreases. This is because it is proportional to $\frac{1}{n_p}$, which increases less for decreasing n_p.

The uncertainty for thrust coefficient K_T also shows an increasing uncertainty for increasing J. Here, U_{K_T} is mainly caused by the uncertainty of the measured thrust signal. The share of this component is increasing rapidly when the measured thrust forces reduce. This means that the measured signal is relatively fluctuating more than for lower J, where the measured forces are higher. This can be declared by the limits of the force transducer. To demonstrate: for $J = 0.5$, the mean measured thrust force is 110 N, whilst for $J = 1.0$ this is 3.7 N, as shown in Figure 5.5.

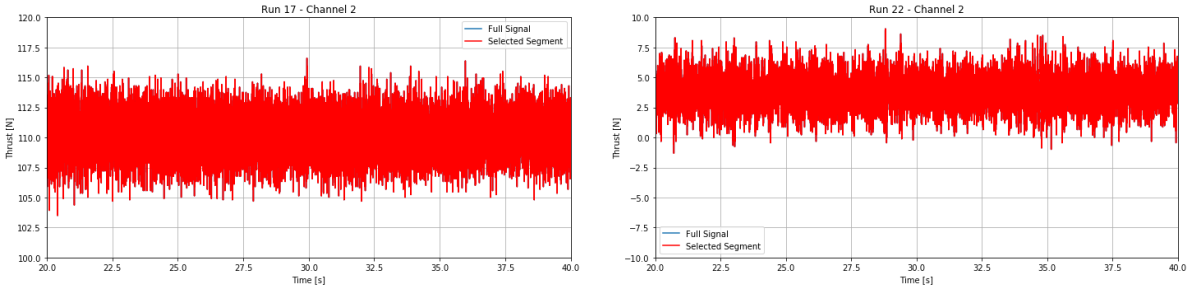

(a) Variation in thrust signal for $J = 0.5$, $\theta_m = 0°$ at $V_A = 1.5$ m/s

(b) Variation in thrust signal for $J = 1.0$, $\theta_m = 0°$ at $V_A = 1.5$ m/s

Figure 5.5: Variation in thrust signal for $J = 0.5$ and $J = 1.0$, $\theta_m = 0°$ at $V_A = 1.5$ m/s

Since the force of the light loading is 30 times smaller, it is plausible that the force transducer may be less accurate. As the force transducer's thrust measuring range covers this up to 340 N, the lowest measured values may be less accurate. For other force transducers, such as presented by Hottinger Brüel & Kjær (2025), the relative error of force transducers increases for decreasing force. Despite the

higher fluctuations at $J = 0.5$, shown in Figure 5.5a, compared to the higher advance ratio in Figure 5.5b, the relative error here is smaller, since its value is higher and closer to the maximum measurable thrust. Moreover, the high relative error for $J = 1.0$ prove why the share of thrust to the uncertainty of K_T grows for increasing J.

One other reason for the increasing uncertainty with increasing J could be that the force fluctuates more for high J due to the fluctuations in the inflow. As described by Yao (2015), the propeller is more prone to fluctuations in the inflow for low propeller loading. Those fluctuations in the inflow over the length of the towing tank are likely the same for each measurement. However, due to the lower rotational speed, these small changes in V_A can cause the increasing fluctuations of the measured signal.

Lastly, the torque coefficient K_Q shows even bigger variations. Here again, the correlation between J and the total uncertainty U_{K_Q} is clearly visible and the effect is even bigger than for the thrust coefficient. Here the measured torque $Q = 4.05$ Nm for $J = 0.5$ and $Q = 0.29$ Nm for $J = 1.0$. It seems that the accuracy of measured torque is reducing faster when approaching zero torque than thrust. Therefore it is even more sensitive to fluctuations and noise, such as vibrations.

Now the uncertainty for K_T and $10K_Q$ have been assessed, a discussion on the results for varying inflow angle can be given. In Figure 5.6 the thrust coefficient and 10 times the torque coefficient are shown for all measured pitch angles θ_m. For each point, the above described uncertainty is also shown. In Figure 5.6b, 5.6c and 5.6d, the grey line shows the mean values of the straight case for comparison.

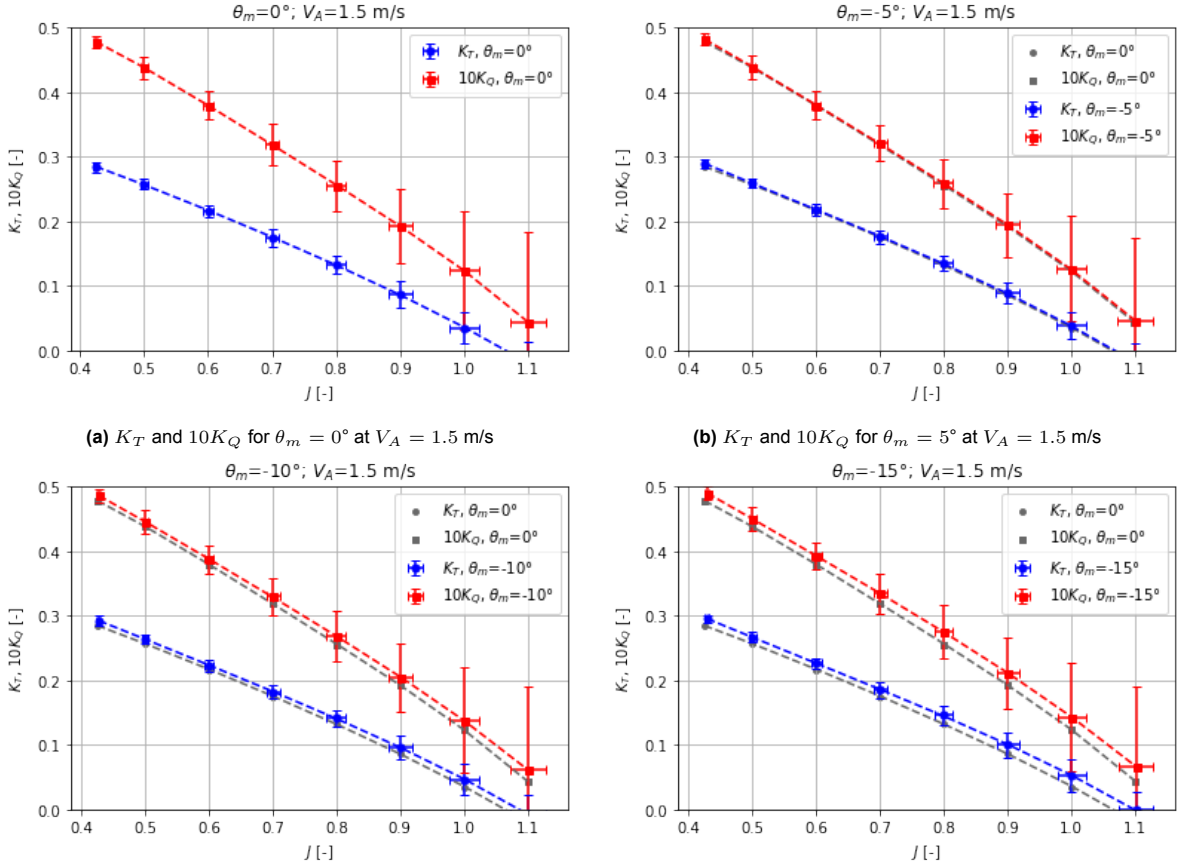

(a) K_T and $10K_Q$ for $\theta_m = 0°$ at $V_A = 1.5$ m/s

(b) K_T and $10K_Q$ for $\theta_m = 5°$ at $V_A = 1.5$ m/s

(c) K_T and $10K_Q$ for $\theta_m = 10°$ at $V_A = 1.5$ m/s

(d) K_T and $10K_Q$ for $\theta_m = 15°$ at $V_A = 1.5$ m/s

Figure 5.6: K_T and $10K_Q$ for all different pitch angles θ_m at $V_A = 1.5$ m/s

Based on the mean values, an increase in both thrust and torque was already observed for increasing pitch angle. Moreover, the dependency on J is also clearly visible as the difference between the straight case and the inclined cases increases for increasing advance ratio. For example, the increase in thrust coefficient for $J = 0.5$ for $\theta_m = 15°$ compared to $\theta_m = 0°$ is 0.01, whilst for $J = 1.0$ this is 0.14 in

absolute sense. Relatively this increases are 3.78% and 50.7% respectively. This again matches with the observation of Yao (2015) that a propeller with low thrust loading is more affected by oblique inflow conditions. This trend is also visible for torque, where both absolute as relative differences of K_Q with and without a pitch angle grow for increasing J.

However, Figure 5.6 also shows that the uncertainty, also increasing with J, increases even more than the difference between zero pitch angle and the other cases. Due to this large uncertainty intervals, the increase in mean value can not be fully verified with these experimental results. The fact that the highest uncertainty intervals show up at the highest J is particularly important as this is exactly the region where propellers of WASP ships will operate most of the time. Also, for almost all other data points the measured force and torque coefficients for $\theta_m = 0°$ lies in the uncertainty interval of the inclined cases. As the increase of both K_T and K_Q are not significant compared to its uncertainty, the straight open-water results for a propeller give a good indication of the resulting thrust and torque. Therefore, estimating propeller performance in an early design stage of a WASP ship would be possible with just using the known open-water characteristics. However, later on the drift angle will be important for the propeller's strength, due to generated in-plane loads, as described by Muscari, Dubbioso, Ortolani, and Di Mascio (2017).

One other observation as a result of the pitch angle, is the varying loads on the propeller on each blade position. As explained by Figure 3.2, the angle of attack, and therefore the forces of the propeller blade fluctuates, with a maximum value at $\theta = 0°$ and a minimum at $\theta = 180°$. However, since pitch is tested, the maximum and minimum force shift to $\theta = 90°$, $\theta = 270°$. As a result of these fluctuations, it could be expected that the standard deviation, and therefore also the uncertainty, of K_T and $10K_Q$ for increasing pitch angle also increases, as the signal would vary more during each revolution. To show this, the uncertainty of all angles for $J = 0.5$ and $J = 1.0$ are shown in Figure 5.7.

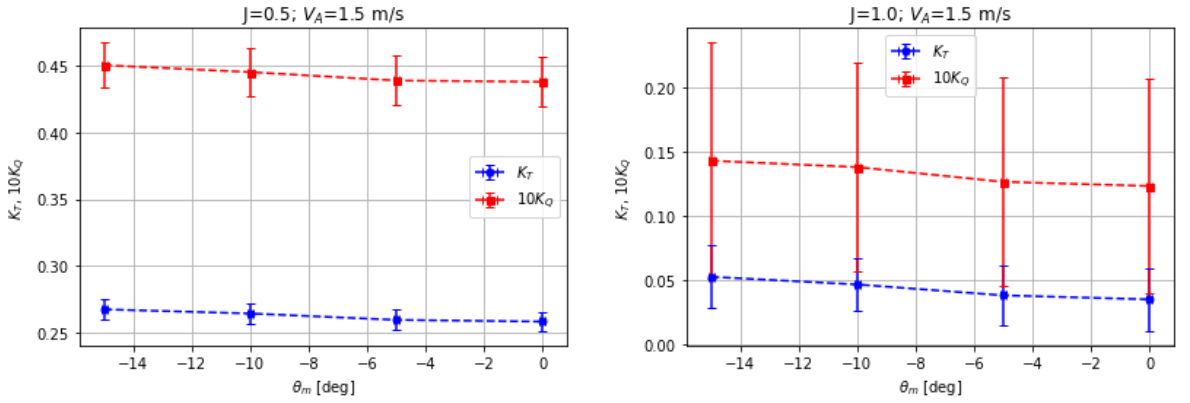

(a) K_T and $10K_Q$ for $J = 0.5$ for all pitch angles θ_m at $V_A = 1.5$ m/s **(b)** K_T and $10K_Q$ for $J = 0.5$ for all pitch angles θ_m at $V_A = 1.5$ m/s

Figure 5.7: K_T and $10K_Q$ for $J = 0.5$ and $J = 1.0$ for all pitch angles θ_m at $V_A = 1.5$ m/s

These Figures show that the uncertainty remains almost constant for increasing pitch angle. The standard deviation of the different measurements show some variations. However, these difference are small, for example U_{K_T} varies with a maximum of 0.002 between the pitch angles. This means that, for example, the uncertainty of the mean value of $\theta_m = 5°$ show a uncertainty that is 0.002 larger than the uncertainty of $\theta_m = 0°$. Moreover, there is no trend visible when comparing all advance ratios and both thrust and torque coefficient. The difference are small between all cases and the results show that the highest uncertainty is arbitrarily distributed over the different pitch angles. Therefore, it can be concluded that the force transducer did not capture the fluctuating forces on each individual propeller blade. The global force is measured and is not fluctuating more as a result of the pitch angle.

The carriage speed was also increased to 3.5 m/s. The results of this are shown in Figure 5.8.

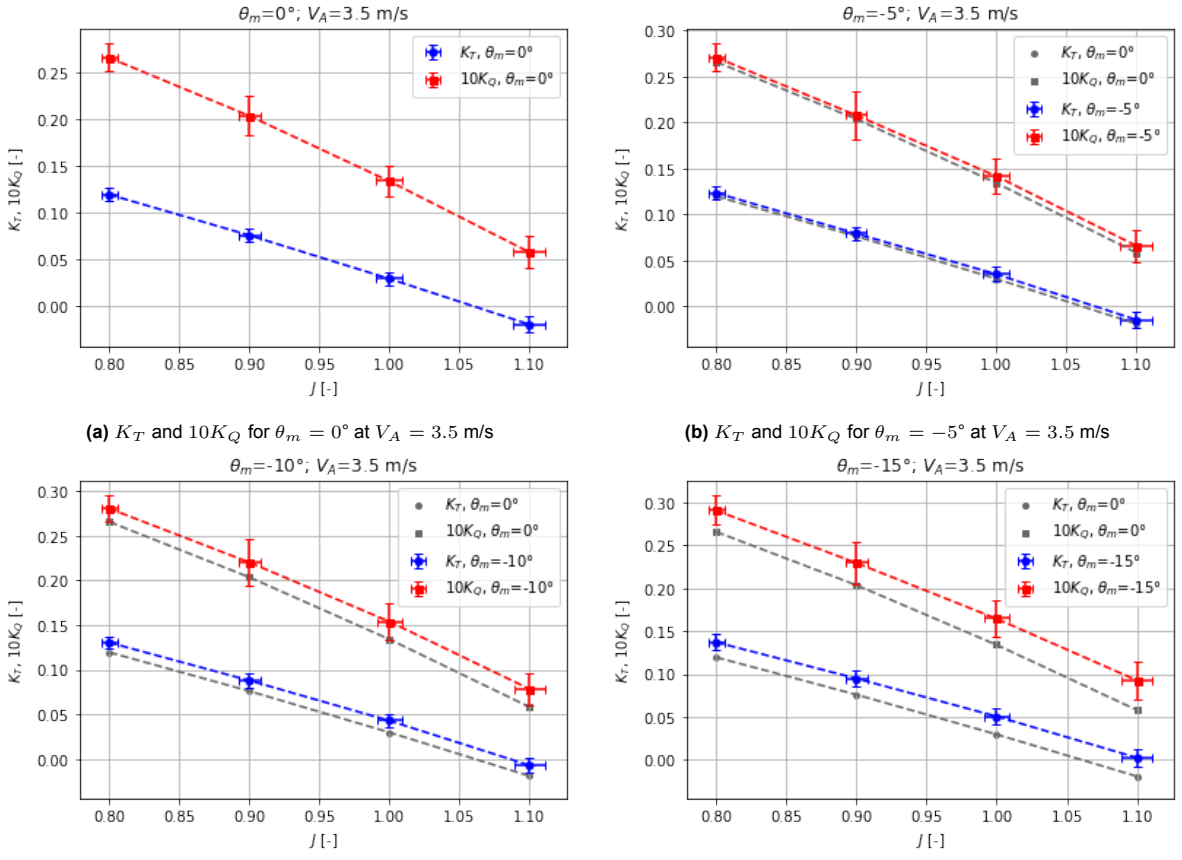

(a) K_T and $10K_Q$ for $\theta_m = 0°$ at $V_A = 3.5$ m/s

(b) K_T and $10K_Q$ for $\theta_m = -5°$ at $V_A = 3.5$ m/s

(c) K_T and $10K_Q$ for $\theta_m = -10°$ at $V_A = 3.5$ m/s

(d) K_T and $10K_Q$ for $\theta_m = -15°$ at $V_A = 3.5$ m/s

Figure 5.8: K_T and $10K_Q$ for all different pitch angles θ_m at $V_A = 3.5$ m/s

From these figures, the increase in uncertainty of advance coefficient J can again be observed. This uncertainty increases from $U_J \approx 0.006$ for $J = 0.8$ to $U_J \approx 0.011$ for $J = 1.1$, which is mainly caused by the lower rotational speed of the propeller. This uncertainty is independent on the pitch angle, like this was the case for the lower carriage speed. On the contrary, there seems to be a dependency of the uncertainty of the thrust and torque coefficients on pitch angle, whilst this was not the case at $V_A = 1.5$ m/s. For increasing pitch angle, the uncertainty slightly increases. This could indicate that the fluctuations in thrust and torque as a result of the pitch angle are slightly visible. This trend is found for almost all J. However, the increase is not always observed and not linear, as the difference in uncertainty between $\theta_m = -5°$ and $\theta_m = -10°$ is relatively small.

The increase of thrust and torque is again visible. However, the uncertainty these values is significantly lower than for $V_A = 1.5$ m/s. As shown in Figure 5.8d, the uncertainty does not reach the mean value of case without an angle. This shows that the increase of thrust and torque is more significantly shown in this data compared to the data in Figure 5.6. However, it should be noted that this mean value also has an uncertainty, see Figure 5.8a, which is not shown in comparison with the drift angle for visibility. The fact that this difference also appears for this combinations of carriage speed and rotational speed of the propeller, shows that this trend is probably captured well.

The most plausible reason for this reduction of uncertainty of K_T and K_Q is that the measured thrust and torque are higher compared to the case with a lower carriage speed. For example, for $J = 1.0$ the thrust force was 3.71 N for $V_A = 1.5$ m/s, whilst this is 29.4 N for $V_A = 3.5$ m/s. As shown in 5.5, the obtained thrust signal therefore show less fluctuations and the standard deviation decreases.

Moreover, the wake of the gondola's strut will slightly vary due to increased Reynolds number. The boundary layer is thicker at lower Reynolds numbers, which causes the viscous effects to increase in this layer (ITTC (2024)). As the passing flow has less time to drag along the gondola, the propeller is

less influenced by this wake, since the speed of the flow is less affected. Therefore, the variation of the force during a rotation flattens as this wake influence gives a less deep velocity deficit. This sounds a bit counter-intuitive, because above it was mentioned that fluctuations were observed as a result of the drift angle. However, this was a comparison between the measurements of the pitch angles, whilst here the uncertainty of two different carriage speeds are compared.

Also, the influence of θ_m seem to differ between both cases. This difference is shown by the comparison between $V_A = 1.5$ m/s and $V_A = 3.5$ m/s in Figure 5.9.

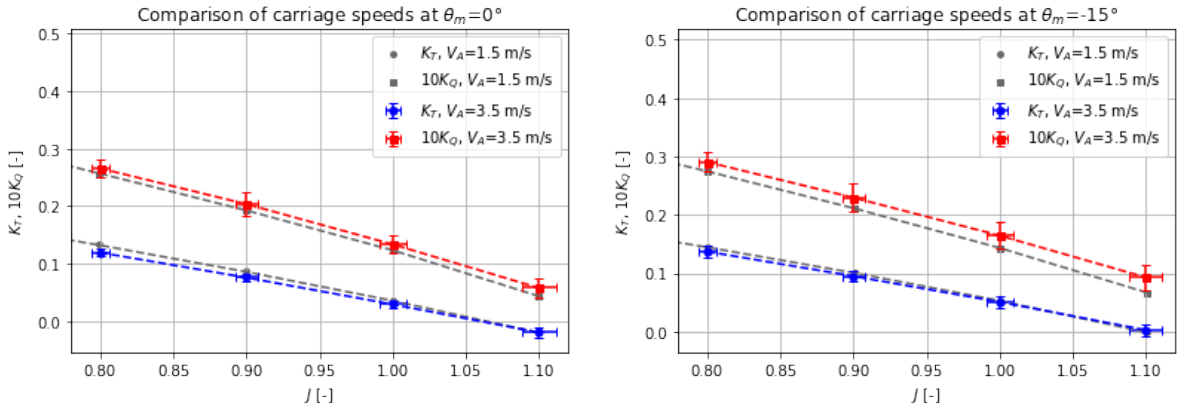

(a) K_T and $10K_Q$ for both carriage speeds at $\theta_m = 0°$

(b) K_T and $10K_Q$ for both carriage speeds at $\theta_m = -15°$

Figure 5.9: K_T and $10K_Q$ for both carriage speeds at $\theta_m = 0°$ and $\theta_m = -15°$

As already mentioned before, the thrust for the highest carriage speed is slightly lower than for the lower carriage speed. The torque is slightly higher, which can be seen in Figure 5.9a. In Figure 5.9b, where the propeller is at $\theta_m = -15°$, these differences have slightly changed. The thrust coefficient is now more equal, showing that thrust has increased more. This trend is also visible for the torque coefficient. Whilst $10K_Q$ was already higher without a pitch angle, this difference has increased at a 15-degrees pitch angle. This shows that the drift angle has more effect on the thrust and torque for the higher carriage speed, and therefore the higher Reynolds number. However, the uncertainty shows again that this difference is not significant enough to be proved with this data.

5.2.2. Bias error

Besides the precision error, there are always bias errors in experiments. Bias errors mostly originate from the test environment and the setup of the experiment. These errors are difficult to quantify, as these show up in each run and therefore only shift the measured value compared to the real exact value.

Firstly, there are several possible causes of bias errors in the experimental setup. The gondola is placed under the hexapod. Afterwards, the position needs to be calibrated, to check if the drift angle is zero in this case. This is done using a small light that was placed on a stationary place above the carriage. To check if the orientation of the gondola was good, the carriage passed this light on a slow speed and the track on the shaft of the gondola was checked. This was done on sight and therefore some uncertainty is introduced. An estimation of this error is $\beta_m = \pm 0.1°$. Moreover, the propeller is operating behind the shaft and the strut of the gondola. This introduces some wake field, which can cause some deviations in thrust and torque compared to real open water inflow. The strut in front of the propeller in combination with the uncertainty in drift angle increases this uncertainty, as the obtained results showed influence of the strut at a drift angle for small angles. Also, some uncertainty can originate from the calibration factors. The calibration factors were obtained a few years ago. Thereafter, the force transducer is not used anymore. However, a new calibration test, could also introduce some uncertainty, as such setups also could contain some bias errors.

Then there are some environmental factors that can have an influence on the deviation of the measured value compared to the real value. The water temperature T could change over time. The water

temperature influences both the density of the water ρ_w as the kinematic viscosity ν. However, the temperature is not measured continuously, so once again this can be a source of uncertainty due to bias errors. Lastly, there can be some influence from the fact that the runs are carried out in sequence. A 20-minute gap was left between each run such that small waves disappeared. However, it can be that there is some difference with the first measurements of a day, since there the water is more calm. This error is covered by always repeating the first run of the day to ensure the same testing conditions.

5.3. Signal analysis

Till now the time-averaged values of K_T and K_Q were considered. As the expectation for propeller at a drift angle is to have varying loads, it is expected that these fluctuations should be found in the time signals of the measurements. From the time signals the dominant frequencies in these signals can be extracted. Sun et al. (2023) showed that the blade passing frequency (BPF) is the dominant frequency in thrust and torque signal. The blade passing frequency is defined as the rotational speed of the propeller times the amount of blades: $BPF = n_p \cdot Z$. Sun et al. applied the frequency analysis to a simulation for propellers that are at drift behind a ship. In the performed experiments, this same outcome could be expected.

First, the signal needs to be filtered. Initially, the signal is noisy and needs to be smoothened. Therefore a Savitzky–Golay filter is applied. The Savitzky–Golay filter is a filter that uses a least square method which smoothens the signal (Savitzky and Golay (1964)). This is done by using a window that applies a polynomial to the data points in this window. The least-square solution of this polynomial is calculated to follow the trend of the signal as good as possible, reducing the noise level. This filter is applied to the obtained signals from the experiment. The applied window-size spans 21 data points, and the order of the polynomial used to fit to the data is three. The window is kept relatively small such that the filtered signal still follows the original signal as good as possible, but removing the peaks. In Figure 5.10, an example of the filter applied to a torque signal is shown.

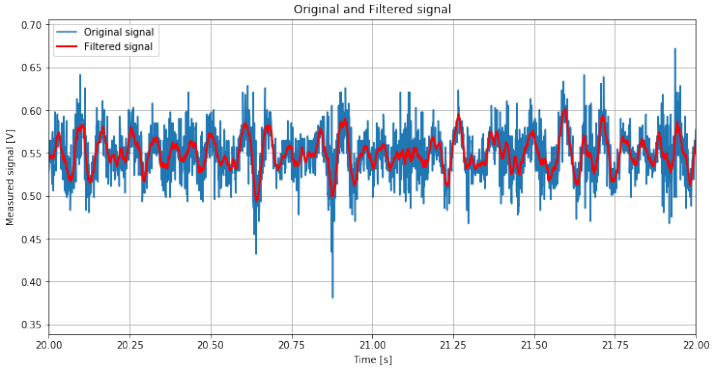

Figure 5.10: Example of original signal and filtered signal

Before the time-domain signal can be converted to the frequency-domain, a window function is applied to the signal. This reduces spectral leakage. Spectral leakage occurs because most signals do not contain an integer number of cycles of the sine functions that the signal contains (National Instruments (2006)). The Fast Fourier Transform (FFT) assumes that the full time signal contains an integer cycles. However, in most experimental this is not the case as the start and end of the measurement is determined without taking this frequencies into account. Therefore, the begin and endpoint of the signal are likely to be at a different part of the cycle, which causes the value to be different. When the FFT is applied to the full signal, the boundaries do not match. This causes the FFT to analyse a discontinuous function. As this transition appears as a jump in the value of the signal, this induces some additional high frequencies. Applying a window function reduces this effect.

The window function applied is the hamming function. This function is applied to ensure lower the noise from surrounding frequencies. In National Instruments (2006), this is explained by the influence on the side lobes. The hamming function cancels these side lobes well, but others are less cancelled. This is

because the endpoints do not reach zero, which means that there are still some discontinuities in the signal used in the FFT. In Figure 5.11, the hamming function is shown.

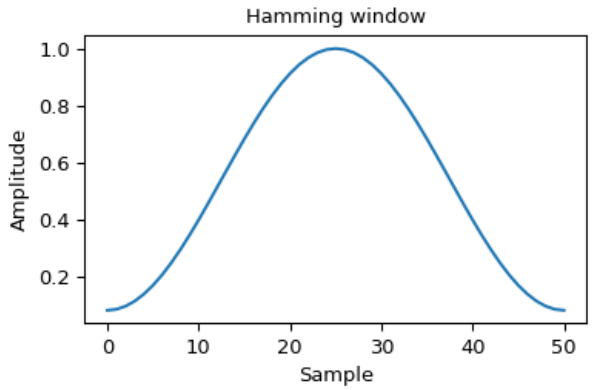

Figure 5.11: Hamming function ("SciPy v1.16.2 Manual" (2008))

Despite the small discontinuities, the Hamming window is used, because it captures the difference between frequencies close to each other better than other window functions, such as the Hanning function. The motivation for this will be shown later, as noise and the blade passing frequency are sometimes frequencies that are close to each other.

The time domain is converted to the frequency domain using Fast Fourier Transform. The FFT decomposes the signal in sinusoidal components with varying amplitudes and frequencies. By analysing the decomposed signal, the amplitude of each signal indicates which frequencies are dominant in the signal. Before performing the FFT, the signal is split into four segments of equal size. This means that for the runs with $V_A = 1.5$ m/s, each part contains 16250 data points. For $V_A = 3.5$ m/s each segment contains 5000 data points. A Hamming window is applied to each segment. Finally, the FFT is done for each of these segments and the results are averaged to obtain a single frequency spectrum.

Firstly, the results of the lowest carriage speed, which is 1.5 m/s will be presented. At this low speed, the rotational speed is lower than for 3.5 m/s and therefore the peaks of the blade passing frequencies are expected at lower frequencies. In Figure 5.12, the frequency spectra for $J = 0.5$, $J = 0.8$ and $J = 1.0$ are shown. The vertical lines show multiples of the blade passing frequency. However, it should be noted that also $0.25 \cdot BPF$ and $0.5 \cdot BPF$ are shown. The shaft frequencies of these advance coefficients are 13.8, 8.625 and 6.9 Hz respectively.

Surprisingly, both the shaft frequency, which is $0.25 \cdot BPF$, and $0.5 \cdot BPF$ are the dominant frequencies in the signal. This not in line with previous experiments, as Sun et al. (2023) found the BPF itself as dominant frequency. Moreover, there was found that also $2 \cdot BPF$ and $4 \cdot BPF$ are observed as peaks. However, these are not observed in those frequency spectra, as these are not significantly higher than other high frequencies observed in the FFT. It can be observed that for the lowest J, the magnitude of the shaft frequency is the highest. However, for increasing J, it is observed that the magnitude of this frequency decreases. Moreover, the frequency that corresponds to $0.5 \cdot BPF$ increases for increasing advance ratios. What can be seen for low thrust loading is that the noise is in the same frequency range as the dominant frequencies. For these J, the shaft frequency is relatively small compared to the noise.

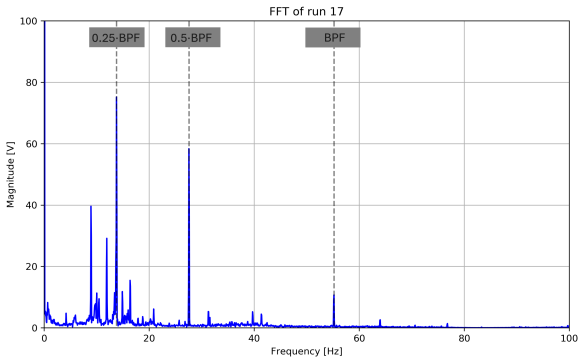

(a) FFT of thrust signal for $J = 0.5$ at $V_A = 1.5$ m/s

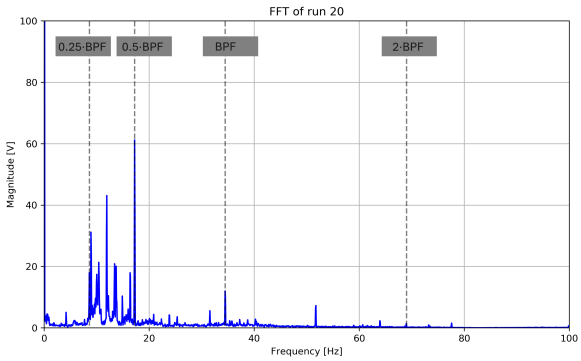

(b) FFT of thrust signal for $J = 0.8$ at $V_A = 1.5$ m/s

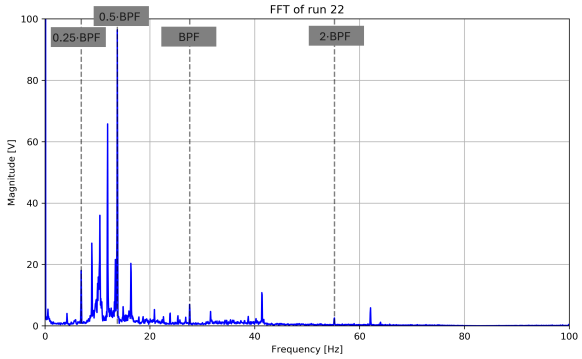

(c) FFT of thrust signal for $J = 1.0$ at $V_A = 1.5$ m/s

Figure 5.12: FFT of thrust signal for $J = 0.5$, $J = 0.8$ and $J = 1.0$ at $V_A = 1.5$ m/s

This low frequency noise is found in each run at $V_A = 1.5$ m/s. The frequencies that show up the most are 8.93 Hz and 11.93 Hz. Especially 8.93 Hz is close to $0.25 \cdot BPF$ of $J = 0.8$. However, each of these frequencies are observed separately. In general it was found that for $J = 0.8$ and higher, the highest noise frequency of those two was dominant compared to the lower one. This is a bit counter-intuitive, as for high J, the propeller's BPF and its multiples are lower and closer to 8.93 Hz. Other frequencies that show up frequently are 10.4 Hz, 12.2 Hz 13.4 Hz and 16.4 Hz.

When the carriage speed is increased, the propeller rotational speed is also increased and therefore $0.25 \cdot BPF$ and $0.5 \cdot BPF$ is not in the range of the low-frequency noise anymore. The FFT results of $J = 0.8$ and $J = 1.0$ for $V_A = 3.5$ m/s, are shown in Figure 5.13.

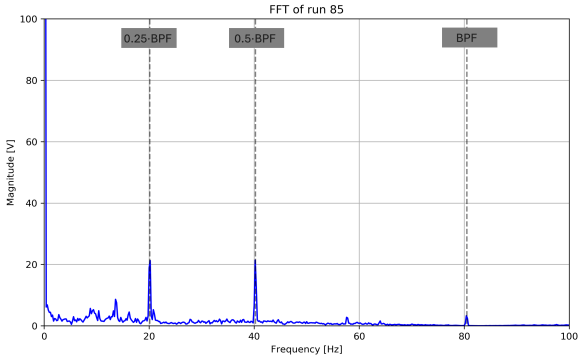

(a) FFT of thrust signal for $J = 0.8$ at $V_A = 3.5$ m/s

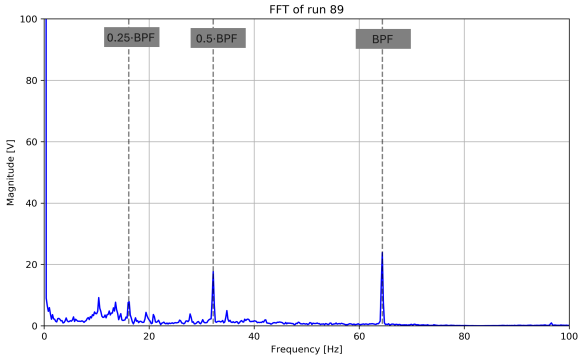

(b) FFT of thrust signal for $J = 1.0$ at $V_A = 3.5$ m/s

Figure 5.13: FFT of thrust signal for $J = 0.8$ and $J = 1.0$ at $V_A = 3.5$ m/s

Here, the magnitudes of the found frequencies are all lower than for 1.5 m/s. This can be caused by the fact that the fluctuations of the signal are less compared too the lower velocity as seen in the uncertainty

analysis. Moreover, since the frequencies are not in the region of low-frequency noise, the multiples of the BPF look more pronounced. However, relatively, the noise is still significant. In Figure 5.13b, the blade passing frequency itself is the biggest, as it was expected to appear in all signals. However, this is rather an exception than a trend. Also, the shaft frequency almost completely disappears between the noise. The noise frequencies that are mainly found at this higher speed are 8.8 Hz, 10.4 Hz and 13.6 Hz.

The noise in above-mentioned cases can have several causes. Firstly, a possible contribution of the wheels of the carriage was checked, as those would add a periodically contribution to the signal. The diameter of the wheels are 0.690 meter, and therefore the circumference is $\pi \cdot 0.690 = 2.168$ meter. If the wheels are one of the causes of the noise, this would show up as a peak around the frequency of the rotation of the wheels. For $V_A = 1.5$ m/s, this frequency would be 0.691 Hz, whilst for $V_A = 3.5$ m/s, this is 1.615 Hz. Despite observing small peaks close to these frequencies, these exact frequencies are not found, indicating that the noise is not originating from there. Moreover, the peaks found around these frequencies are very small compared to the noise in the region of the shaft frequency.

Another observation that has been made, is the fact that the noise is not velocity depended. If this was the case, a factor of $\frac{3.5}{1.5} = 2.33$ between the noise frequencies at the low and high speed is expected. However, as shown with the given noise signals that appear the most for both cases, this factor is not observed. On the contrary, the frequencies are in the same frequency span, showing that the noise is not velocity depended.

Three other possible causes remain, which are not surely the main cause of the noise. Firstly, the signal from the force transducer is already very noisy. An example is given in 5.10, where it can be seen that the signal is consists of many different frequencies. The filter could be changed by using a wider window. However, this would also affect the other frequencies as the general trend of the signal is barely followed in that case.

One other possible problem is the control system of the gondola. This control loop ensures that the requested rotational speed of the shaft is maintained during the run. In other experiments with the gondola, this effect was observed for relatively low n_p, which where under 50 rpm. In Figure 5.14, an example of the signal of the propeller's rotational speed is given.

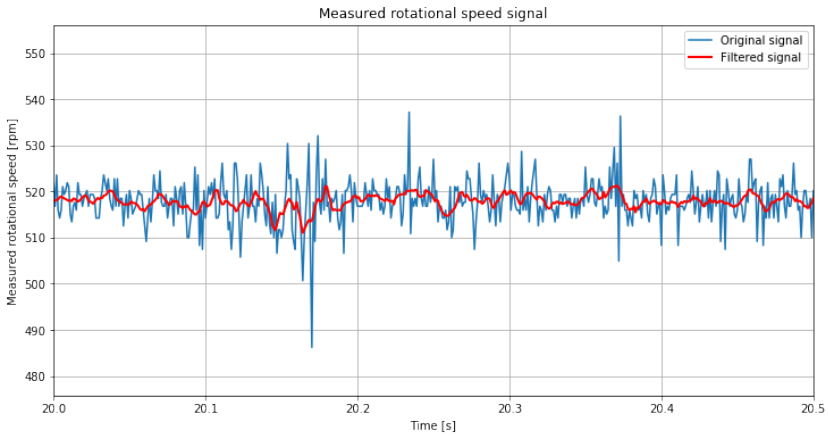

Figure 5.14: Example of the propeller rotational speed signal

Despite, the fact that the measured signal is varying, the control loop is able to keep the requested rotational speed. This control problem therefore seems to be less significant for higher n_p. However, from this signal it is hard to distinguish which part of the fluctuations are caused by data acquisition and what the share of the control loop of the ServoDrive is.

Lastly, it is remarkable that the frequencies of the noise that are found are almost always the same, indicating that the noise is also independent or partial independent of n_p. Another explanation of these frequencies could originate from vibrations of the structure. As explained in chapter 4, the gondola is mounted to the carriage via the HexaPod and beams. This structure therefore has some natural

frequencies. An explanation that those frequencies show up can be that the structure is excited with frequencies close to those natural frequencies.

Based on C. Wang et al. (2017), the influence of the pitch angle θ_m should be noticed as well. They showed that the magnitude of the BPF and its multiples should increase for increasing pitch angle. This could also be expected by analysing in plane loads, which were for example explained by Dubbioso et al. (2013). They stated that the variations in all propeller increased for increasing θ_m. This increasing fluctuations imply the higher magnitude for the signal with the frequency of the passing blades. Since the BPF itself is not found, the influence of the pitch angle on the shaft frequency and $0.5 \cdot BPF$ is shown in Figure 5.15.

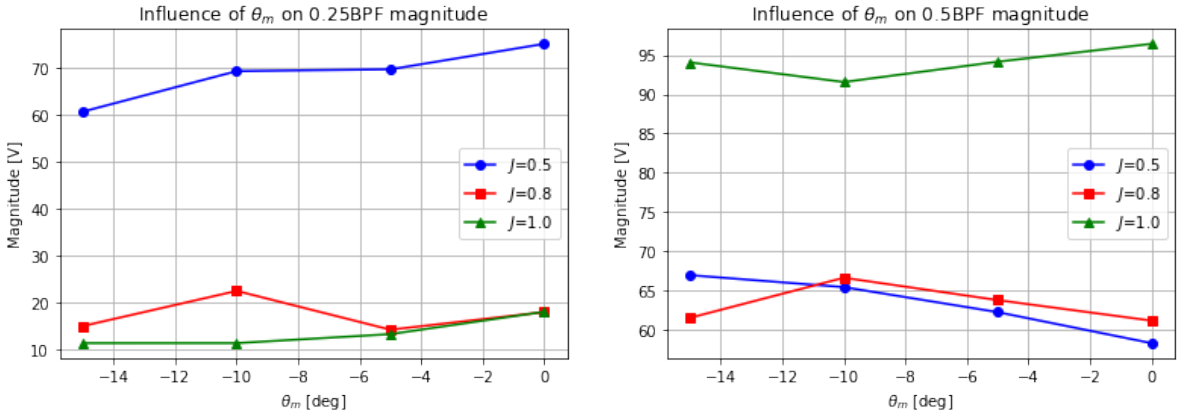

(a) Influence of θ_m on the magnitude of the frequency corresponding to $0.25 \cdot BPF$

(b) Influence of θ_m on the magnitude of the frequency corresponding to $0.5 \cdot BPF$

Figure 5.15: Influence of θ_m on the magnitude of the frequency corresponding to $0.25 \cdot BPF$ and $0.5 \cdot BPF$

Both figures show different trends. Firstly, in Figure 5.15a, a decreasing trend is observed for almost all points. This is the opposite trend that was observed by C. Wang et al. (2017). Moreover, for the mildly-loaded and lightly-loaded propeller, the magnitudes are relatively small. This was already observed in Figure 5.12, where these frequencies are difficult to find between the signal's noise.

For $0.5 \cdot BPF$ in Figure 5.15b, a completely different trend is shown. For $J = 0.5$ and $J = 0.8$, the expected increase seem to be visible. However, this was not found for $J = 1.0$. Also interesting to mention is the fact that the magnitude of this frequency is the highest for $J = 1.0$. Since fluctuations in inflow as a result of an angle is affecting the propeller forces more for low propeller loading, as stated by Yao (2015). Therefore, it should not be surprising if these frequencies have a larger magnitude, as thrust and torque show more fluctuations. However, the fact that $J = 0.5$ and $J = 0.8$ are close to each other, and that this distribution of advance ratios is also not visible in Figure 5.15a, show that this is not demonstrated with these experiments.

5.4. Discussion

In the sections above, the results are shown and explained. The agreement with trends found in previous research studies, show that the results are promising. K_T and $10K_Q$ show an increase for increasing pitch angle, with a higher influence at high J. Also the shaft frequency and its multiples were observed in the frequency domain. However, the low-frequency noise is relatively large here. The cause of this is probably due to some vibrations from the structure or the carriage.

In this section some additional comparison with literature will be made, an evaluation of the test set-up is given and an indication is given for the implications on full-scale.

Firstly, the results of the experiment are compared to the approximation of Gutsche (1964). The calculation method used is explained in Appendix D, in chapter 11. The results of the calculations are presented in Figure 5.16. For the calculation, the measurement results of the propeller without a drift

or pitch angle is used as reference. The expected thrust and torque coefficient are based on these results to find the agreement of Gutsche's method with the experimental data.

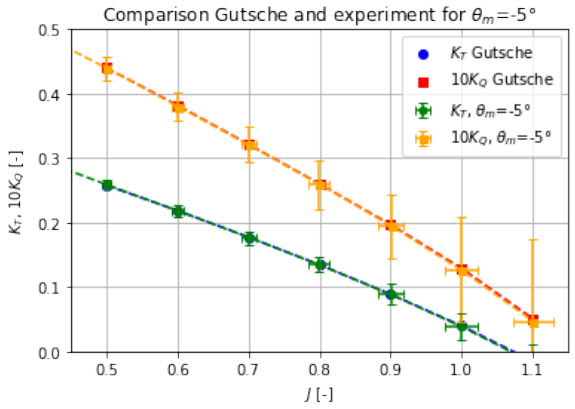

(a) Comparison of experimental results to approximation method of Gutsche for $\theta_m = -5$ ° (Gutsche (1964))

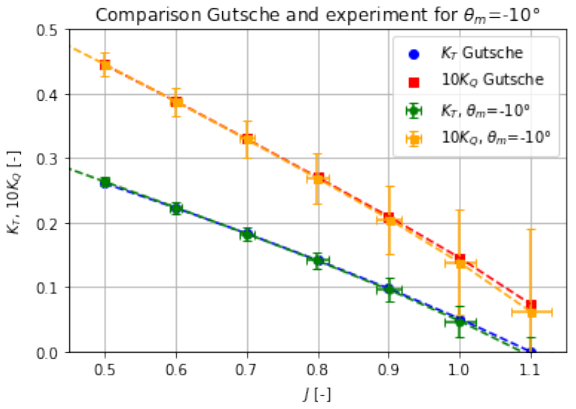

(b) Comparison of experimental results to approximation method of Gutsche for $\theta_m = -10$ ° (Gutsche (1964))

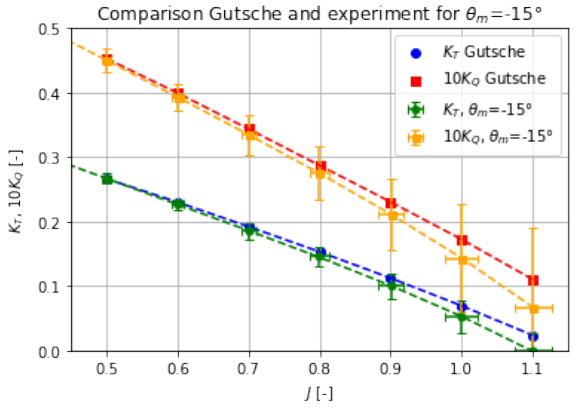

(c) Comparison of experimental results to approximation method of Gutsche for $\theta_m = -15$ ° (Gutsche (1964))

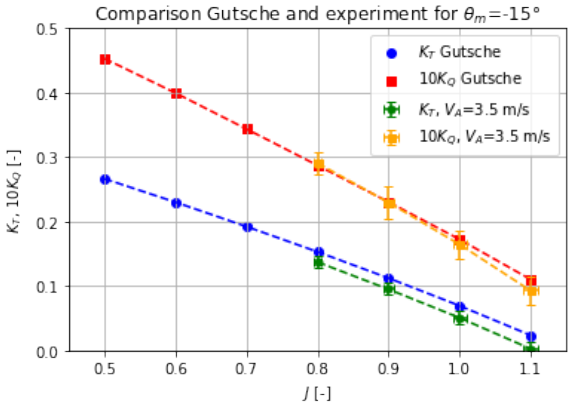

(d) Comparison of experimental results to approximation method of Gutsche for $\theta_m = -15$ ° at $V_A = 3.5$ m/s (Gutsche (1964))

Figure 5.16: Comparison of experimental results to approximation method of Gutsche for $\theta_m = -5$ °, $\theta_m = -10$ ° and $\theta_m = -15$ ° (Gutsche (1964))

Figure 5.16a and 5.16b shows that the approximation of Gutsche is almost equal to the measured thrust and torque coefficient. Especially for the high-loaded cases, the difference is relatively small, with differences of less than 1.5% for $\theta_m = -5$° and $\theta_m = -10$°. From $J = 0.8$, the approximation start to deviate from the measurements, over-predicting both K_T and $10K_Q$. However, for $\theta_m = -15$°in Figure 5.16c, the discrepancies between the measurements and approximation start to increase. At $J = 0.8$, the difference is already 4%, which is much larger than for the smaller angles. Also the discrepancy for even higher advance ratios rises up to more than 160%. At higher Reynolds number, it was observed that the thrust coefficient is slightly lower, whilst the torque coefficient is slightly higher. As shown in Figure 5.16d, the thrust coefficient shows a similar difference between Gutsche's approximation and the results for $V_A = 1.5$ m/s. On the contrary, the torque coefficient is matching better in the case of $\theta_m = -15$ °, and for smaller angles even larger than the approximation of Gutsche.

Evaluating the test set-up, it can be concluded that the measurements have shown results that agree with previous research studies, indicating that the gondola and force transducer fitted well for these measurements. However, a few notes should be made on the set-up.

Firstly, it was shown that the configuration used, with the propeller behind the strut, has some disadvantages as the strut influenced the propeller at small drift angles. Moreover, all measurements were performed in this configuration and therefore the influence in this cases cannot be quantified introducing an unknown bias error for all results. This could be solved by also testing in real open-water conditions

with a completely uniform inflow. Also, the uncertainty of the measured signals is quite high, with fluctuations of more than 150% in the cases of the lowest thrust and torque. The results of a higher carriage speed already showed that the uncertainty decreased due to the fact that the lower limit of the force transducer was avoided. It could therefore be suggested to measure at even higher speeds. However, in that case, the settings of the gondola's Servo Drive should be changed, and a force transducer with higher upper limits should be used to be able to do safely measure thrust and torque for those cases.

Making an hypothesis for the full-scale could be done by analysing the results of the experiments, since all numbers obtained are non-dimensionalised by the propeller diameter and rotational speed. However, it should noted that some scaling effects will occur. Heinke et al. (2019) showed that experiments with a Reynolds number of at least $5.0 \cdot 10^5$ can be used to extrapolate the model scale K_T and K_Q to full-scale. Therefore, the results of the measurements with $V_A = 3.5$ m/s can be used as bench-mark for the full-scale numbers. It can therefore be assumed that a propeller at full-scale, would also generate higher torque and thrust, with the increase depending on the advance coefficient.

6

Numerical analysis

As the experiments are performed, a numerical analysis can be performed. This analysis is done to answer sub-question 4:

What are the effects on the wake characteristics of the propeller model and the propeller loading as a function of the rotation angle under oblique inflow and varying loading conditions determined using numerical simulations?

This is done by firstly describing the numerical set-up used, including the software and type of simulation. Secondly, the propeller geometry used, the domain and the mesh are presented. Lastly, the applied boundary conditions are given. Finally the results for both the global and blade loading of the propeller. Also the wake of the propeller at an angle is described.

6.1. Numerical set-up

For the numerical simulations OpenFOAM v2412 ("OpenFOAM" (2024)) was used. OpenFOAM is a free and open source CFD software that can be used to perform numerical simulations in several flow fields. The solver used is pimpleFoam, which is a combination of pisoFoam and simpleFoam. The pimple algorithm couples the velocity and pressure field when calculating these quantities. The simpleFoam loop is normally used for steady-state problems, whilst the pisoFoam loops can be used for transient problems, such as a rotating propeller.

The pimpleFoam algorithm in OpenFOAM is a Reynolds Averaged Navier-Stokes solver. These RANS (or RAS in OpenFOAM) simulations solve the equations using a Finite Volume Method. With this method the Reynolds Averaged Navier-Stokes equations for incompressible fluids is solved.

$$\nabla \cdot \overline{\boldsymbol{u}} = 0 \tag{6.1}$$

$$\frac{\partial}{\partial t}(\rho\overline{\boldsymbol{u}} + \nabla \cdot (\rho\overline{\boldsymbol{u}} \times \overline{\boldsymbol{u}}) = \boldsymbol{g} + \nabla \cdot (\overline{\boldsymbol{\tau}}) - \nabla \cdot (\rho\boldsymbol{R}) \tag{6.2}$$

Equation 6.1 shows the continuity equation for incompressible fluids, with $\boldsymbol{u}$, the velocity vector. In 6.2, the conservation of momentum is shown. Here $\overline{\tau}$ is the averaged stress tensor and $\boldsymbol{R}$ is the Reynolds stress tensor.

Reynolds decomposition is applied on the velocity term. This means that the velocity vector is split in a mean component and a fluctuating component as given in equation 6.3.

$$\boldsymbol{u} = \overline{\boldsymbol{u}} + \boldsymbol{u'} \tag{6.3}$$

Here, $\overline{u}$ is the mean velocity, and u' is the fluctuating part having a mean of zero. Wall functions are needed, such that the smallest turbulence scales does not need to be resolved. The wall functions used will be explained later.

6.1.1. Propeller model

For the numerical analysis, a digital propeller model is needed. However, since the propeller used in the experiment was relatively old, this data was not available. Also scanning the propeller did not provide a sufficient digital propeller geometry. Therefore, a digital propeller model that can directly be used is chosen. This is the E779A propeller model. This digital model was produced by Wolf Dynamics (2017). The specifications of this propeller are shown in table 6.1 (Salvatore et al. (2006)).

Table 6.1: Characteristics of the E779A propeller model

Diameter D_p [m]	0.22727
Number of blades Z [#]	4
Expanded Blade Area Ratio A_e/A_0 [-]	0.689
Pitch at 0.7R $P_{0.7}$	0.249997
Pitch ratio $P_{0.7}/D$	1.100
Skew angle [°]	0
Blade rake [m]	0.0080

Comparing these characteristics to that of the propeller in the experiments, see Table 4.1, some small differences can be noticed. Firstly, the INSEAN E779A propeller model has a slightly larger diameter. This difference should not affect the results, as both K_T and K_Q are non-dimensionalised numbers, so not dependent on propeller diameter. More important is the fact that the pitch ratio of this propeller model is higher than in the experiment. The higher P/D-ratio gives results in higher thrust and torque (Bernitsas et al. (1981), which will be the main cause of discrepancies between experimental and numerical values for thrust coefficient and torque coefficient. Moreover, the expanded blade area ratio is slightly higher, which also contributes to higher thrust and torque. The propeller geometry is shown in Figure 6.1a.

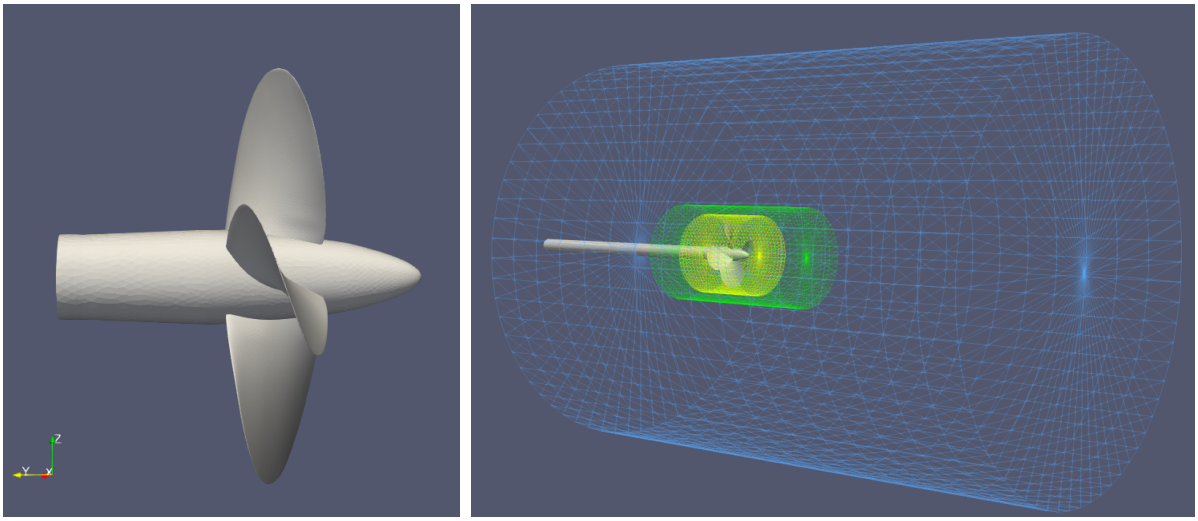

(a) E779A digital propeller geometry **(b)** Numerical domain of the simulations

Figure 6.1: K_T and $10K_Q$ for both carriage speeds at $\theta_m = 0°$ and $\theta_m = -15°$

6.1.2. Computational domain

In Figure 6.1b, the domain of the simulations is shown. Firstly, an important note is to show that the flow-direction is in negative y-direction. The propeller is also oriented in that direction, such as in the

experiment. The shaft of the propeller is upstream of the propeller. The strut of the gondola is not simulated. Reason for that is both computational efforts, and the fact that an open-water set-up is intended. The domain is cylindrical and consist of three cylindrical regions. The blue region is the outerCylinder, which defines the total numerical domain. The upstream boundary of this cylinder is the inlet, and the most downstream position is the outlet. The green part is the innerCylinder, used for extra refinement to analyse the wake of the propeller model. Lastly, the smallest yellow region is the innerCylinderSmall, which is the rotating part in the domain. The dimensions of the cylinders are shown in Table 6.2.

Table 6.2: Dimensions of the cylindrical regions in the domain

Name	Length [-]	Length [m]	Radius [-]	Radius [m]
outerCylinder	$8.0D_P$	1.680	$3.0D_P$	0.700
innerCylinder	$2.5D_P$	0.543	$0.75D_P$	0.163
innerCylinderSmall	$1.01D_P$	0.237	$0.6D_P$	0.133

The innerCylinderSmall is defined to introduce the rotating part of the mesh using Arbitrary Mesh Interface (AMI). AMI is commonly used in transient propeller simulations. It produces two patches, which overlap. Between these patches an interpolation of the physical parameters is applied. This is done because the mesh of the rotating part is not perfectly aligned with the static mesh at each time step. In this simulation, this is done with the cyclicAMI. This dynamic mesh region is rotating with a predefined rotational speed, around an axis that can be changed. Therefore, this method can also be used for the propeller at a drift angle, as the axis of rotation is changed.

6.1.3. Mesh

Meshing is done using blockMesh and snappyHexMesh in OpenFOAM. The blockMesh algorithm is used to define the edges of the domain. It generates hexahedral blocks that are used as base mesh, after which the outerCylinder cuts the edges of this box to obtain the cylindrical domain. The chosen cell size of the base mesh is 0.04 meter ($0.18 \cdot D_P$, which was also used by Gaggero and Villa (2016). Therefore the total domain consists of 42 blocks in the length, which is along the y-axis. In the x-direction and z-direction the total amount of blocks is 35.

Thereafter, snappyHexMesh is used to mesh the regions, surfaces and feature edges of the propeller, hub and cylinders. The propeller geometry is split into two parts (Wolf Dynamics (2017)): the back and the face of the blade. This separation in the geometry allow to refine the leading and trailing edge. In Table 6.3, the refinement levels applied to each part are shown.

Table 6.3: Overview of the refinements of surfaces, regions and feature edges

Name	Refinement level	Cell size [mm]	Feature refinement level	Feature refinement cell size [mm]
outerCylinder	0	40	0	40
innerCylinder	4	2.5	-	-
innerCylinderSmall	5	1.25	5	1.25
Propeller blades	5	1.25	6, 9	0.625; 0.078
Hub and Stem	5	1.25	5	1.25

The outerCylinder is not extra refined, since this is the base mesh size, which covers also areas which are of less interest. The innerCylinder however is additionally refined, as this region is of interest as its visualises the wake of the propeller. To have a gradual transition between the outer and inner cylinder, some buffer layer cells are introduced, as this gives a better diffusion in the end. The innerCylinderSmall needs a refinement of at least one level more, as the fields would probably already have been diffused before arriving in the wake refinement. The refinement for the innerCylinderSmall is based on mesh refinements used by Zhang and Zhang (2022). In this paper, some refinement regions were added

close to the propeller tip to capture the tip vortex. The medium grid in this research has a local cell size of $0.004 \cdot D_P$ at the transition from the tip refinement to the wake refinement. This mesh size can be used here as it is not needed to perfectly capture the tip vortex, which is the case in the study of Zhang and Zhang (2022). Therefore, level 5 refinement is chosen, which is a cell size of $0.0055 \cdot D_P$.

The propeller blades needed the most refinement to capture its geometry. The surface is first refined with refinement level 5. This level is also used for the propeller hub and stem. The hub is the part of the propeller shaft that is inside the rotating domain, whilst the stem is the part in the static mesh. However, this refinement level is not sufficient for the leading and trailing edge of the propeller, as the angles of the geometry are too high in that region. Therefore, based on Gaggero and Villa (2016), the feature edges are refined up to level 9. Moreover, the cells on a distance of 0.002 meter to this feature edges are refined up to level 6, as shown in Figure 6.2b.

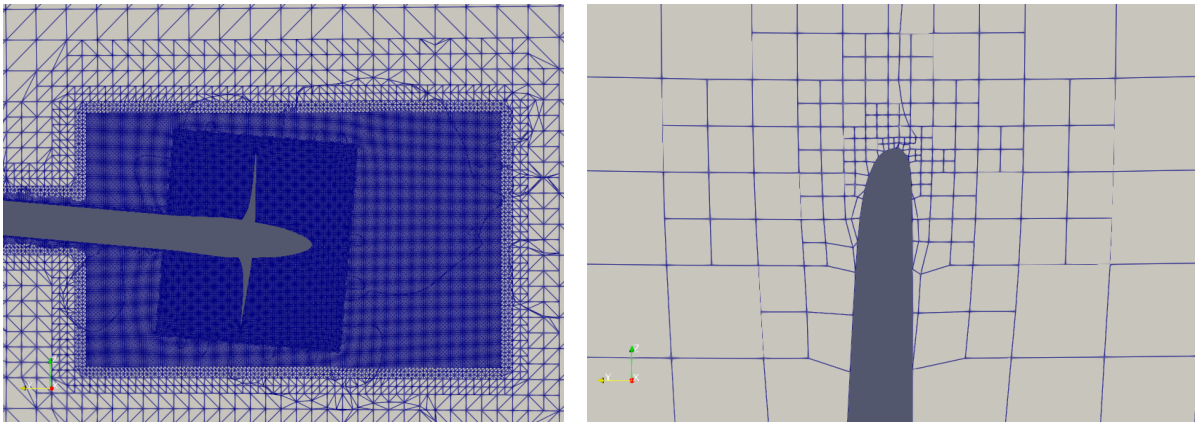

(a) Mesh refinements regions for $\theta_m = -5°$ **(b)** Refinement on the feature edges of the propeller blades

Figure 6.2: K_T and $10K_Q$ for both carriage speeds at $\theta_m = 0°$ and $\theta_m = -15°$

Figure 6.2a shows the different refinement regions, with the innerCylinderSmall at a pitch angle. This part is also at an angle as the mesh rotates around the same axis as the propeller. In Figure 6.2b, it is clearly visible that this is the mesh after castellation and snapping. When these steps are performed snappyHexMesh creates layers to form a prism layer with cells that have a smaller cell height. This prism layer is needed to resolve the viscous boundary layer. In this boundary layer, the velocity profile changes, as the viscous effects near a wall become dominant. To resolve the flow in this boundary layer, a certain cell height should be reached. This cell height can be estimated by determining the value for y^+. This is a non-dimensional distance from the wall in viscous lengths (Pope (2000)). This is the real distance from the wall, divided by the viscous length-scale, which is depended on kinematic viscosity and friction velocity.

To estimate the value for y^+, the first step is to determine the Reynolds number. This is done at the radial position of $r = 0.7R$, as in equation 6.4.

$$Re_{0.7} = \frac{c_{0.7}\sqrt{V_A^2 + (0.7\pi n_p D_p)^2}}{\nu} \tag{6.4}$$

Thereafter, a skin-friction coefficient C_f is calculated, using the regression formula in 6.5. The wall shear stress τ_w is calculated as in formula 6.6. Note that the reference velocity here is the velocity that the propeller blade experiences, which is a combination of both the inflow velocity and the propeller's rotational speed.

$$C_f = \left(2 \cdot \log_{10}(Re_{0.7}) - 0.65\right)^{-2.3} \tag{6.5}$$

$$\tau_w = \frac{1}{2} \cdot V_{rel}^2 \cdot \rho_w \cdot C_f \tag{6.6}$$

The friction velocity is defined as the fraction of the wall shear stress and the density of water, as shown in formula 6.7.

$$u_\tau = \sqrt{\frac{\tau_w}{\rho_w}} \tag{6.7}$$

The kinematic viscosity ν divided by this friction velocity gives the viscous length-scale δ_ν. Dividing the distance from the wall y, which is the cell height next to the surface in the case of a mesh, by this length-scale gives the definition of the non-dimensional wall distance y^+, as shown in 6.8.

$$y^+ = \frac{y \cdot u_\tau}{\nu} \tag{6.8}$$

The described calculation is performed using the propeller dimensions in Table 6.1, $c_{0.7} = 0.075$ m, $\nu = 1.08 \cdot 10^{-6}$ m²/s, $\rho_w = 998.8$ kg/m³ and $n_p = 8.625$ rps. The cells close to the propeller are refined to refinement level 6. From Table 6.3, the cell height of these cells is 0.625 mm. These numbers lead to a y^+ value of 127.06. To comply to the requirements of the y^+ value according to the log law, y^+ should be in the range of: $30 \leq y^+ \leq 300$. The log law describes the velocity profile in the boundary layer in this y^+ range (Pope (2000)). To comply this profile, the y^+ should be in this range. As the cells close to the propeller are small, this is already the case.

The addition of layers has been performed. However, the simulations became highly unstable for these meshes. Therefore, it is decided to perform the simulations without the layers. This will surely affect the results, but the results can still be used to observe trends. Moreover, the y^+ values close to the propeller are estimated to be in the right range.

6.1.4. Test conditions & boundary conditions

For the numerical analysis, the inflow speed is set to 1.5 m/s, the same as in most of the experiments. The propeller rotational speed is set to 517.5 rpm, which is also the same as in the experiments. However, this means that the advance ratio for this case is slightly lower than $J = 0.8$, because the E779A propeller model has a larger propeller diameter. Therefore these simulations are performed at $J = 0.765$.

As already mentioned, a uniform inflow velocity of 1.5 m/s in the negative y-direction is imposed. At the outlet, the flow leaves the domain. However, it the inflow to the outlet is set to zero to prevent backflow. On the outerCylinder, a no-slip condition is applied. The propeller blades and hub are defined as moving wall, as these are rotating parts of the mesh.

The pressure at the inlet and the outerCylinder is defined as *'zeroGradient'*. This allows the pressure to adjust at the inlet according to the defined inlet velocity. At the outlet, the pressure is set to zero, which imitates ambient pressure.

The turbulence model used in the simulations is the $k-\epsilon$ model. This turbulence model is a model that solves the transport equations of two turbulence parameters. These are the turbulent energy k, which is calculated as in 6.9, and the turbulent dissipation rate ϵ, calculated with formula 6.10.

$$k = \frac{3}{2}\left(U_\infty \cdot I\right)^2 \tag{6.9}$$

In these equations, U_∞ is the reference velocity, which is 1.5 m/s in this case. I is the turbulent intensity, which is estimated to be 0.01. This results in a kinetic energy $k = 3.375 \cdot 10^{-4}$ m²/s².

$$\epsilon = C_\mu^{\frac{3}{4}} \frac{k^{\frac{3}{2}}}{l} \tag{6.10}$$

Here, C_μ is a turbulence model constant, which is equal to 0.09. l is the turbulent length-scale. The turbulent length-scale is estimated as $0.07 \cdot D_P$, which is 0.0152 meter. This gives a dissipation rate of $\epsilon = 6.70 \cdot 10^{-5}$ m²/s³.

Lastly, the turbulent viscosity ν_t is determined based on k and ϵ, as shown in equation 6.11.

$$\nu_t = C_\mu \cdot \frac{k^2}{\epsilon} \tag{6.11}$$

The complete discretization and solution schemes are given in Appendix C (see chapter 10).

6.2. Numerical results

The results of the simulations are described in this section. Firstly the total propeller forces and moments are presented. Thereafter the loads of a single propeller blade are analysed. Lastly, some wake characteristics of the propeller are shown.

6.2.1. Total propeller loads

Firstly, the total propeller loads are analysed. In OpenFOAM, the forces are obtained in three directions. The axis of these directions is aligned with the propeller. In the domain, the y-direction is in the flow direction. However, for consistency the force aligned with the propeller, the thrust force, is called F_x. The side force is referred to as F_y and the vertical force F_z. The moments are labelled in line with these conventions, which means that torque is referred to as M_x.

From the simulations, the thrust and torque are extracted. Firstly, the forces are compared to the open-water characteristics of the INSEAN E779A propeller (Salvatore et al. (2006)). This is shown in Figure 6.3b.

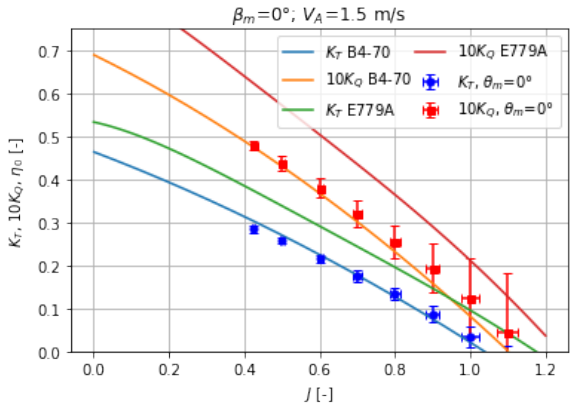

(a) K_T and $10K_Q$ for the experimental propeller model, Wageningen B4-70 propeller model and INSEAN E779A propeller model for $\theta_m = 0°$ at $V_A = 1.5$ m/s

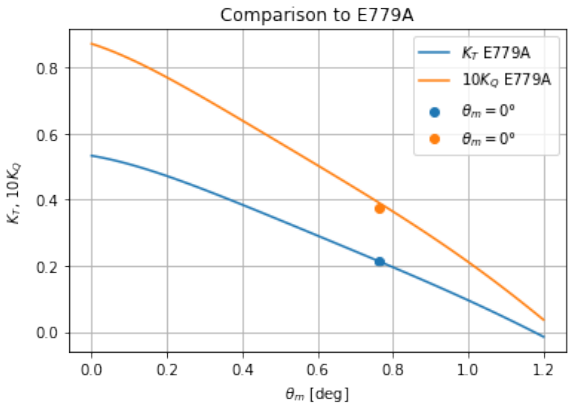

(b) Comparison of K_T obtained from the simulations with open-water characteristics of the INSEAN E779A propeller (Salvatore et al. (2006))

Figure 6.3: Comparison of both experimental and numerical results to available propeller model data

This shows that the case without pitch angle matches well with the known K_T characteristic of the E779A propeller, whilst the torque coefficient $10K_Q$ is slightly lower than expected. As shown in Figure 6.3b, there is no uncertainty interval given. This is because the simulation is done for one mesh refinement only. To estimate the discretization error of those quantities, are refinement study needs to be done, as the error is calculated using the trend based on several different mesh refinements (L. Eça and Hoekstra (2014)). With only one mesh size considered, this analysis can not be performed.

The data of the numerical simulations is not used for comparison to the experimental results. As explained earlier, the propeller used in the experiments is similar to the Wageningen B4-70 propeller. As shown in Figure 6.3a, the experimental data matches the data of this propeller well. However, the difference with the E779A propeller is significantly larger, showing that the propellers differ to much for a valid comparison. Therefore, results in this section will be compared to the available data of the E779A propeller.

In Table 6.4, the total forces and moments are presented for all directions and pitch angles considered. Those are determined from the moment that the values were converged. The averaged values cover 15 propeller rotations, which is equal to 1.74 seconds. The expected increase in thrust for increasing pitch angle is not captured. Here K_T is 0.2146, 0.2212 and 0.2158, for $0°$, $-5°$ and $-10°$ respectively. The total thrust force remains almost the same for each case. The differences between the experimental and numerical set-up could explain this difference. The presence of the strut of the gondola introduces a small velocity deficit which affects the propeller. Moreover, the absence of the prism layer can cause errors in solving for viscous effects.

Table 6.4: Total forces and moments obtained from the numerical simulations

θ_m	0°	-5°	-10°
F_x [N]	42.54306	43.85322	42.78085
F_y [N]	-0.00572	0.612771	1.245253
F_z [N]	-0.00012	6.197888	12.41125
M_x [Nm]	1.70296	1.77776	1.83381
M_y [Nm]	-0.00074	0.125622	0.251754
M_z [Nm]	-8.8 $\cdot 10^{-5}$	0.113376	0.235725

For torque, an increase is found, as $10K_Q$ was 0.3780, 0.3946 and 0.4070 for increasing pitch angle. The increase observed between $\theta_m = 0°$ and $\theta_m = -10°$ at this advance ratio is even bigger than for the experiments, as the increase in the experiments was 5.1%, whilst here, the increase was found to be 7.7%.

The fact that this effect is not observed, show that there could be an error. In numerical simulations, there are three types of errors that can be made: round-off errors, iterative errors and discretization errors (Eça and Hoekstra (2006)). According to Eça and Hoekstra, the round off errors are negligible in most cases. As stated before, the discretization error can not be computed, as only one mesh size is considered. Therefore, it is worth to look at the iterative error. This is the error made due to the fact that the equations in the simulation need to be calculated iteratively. For integral quantities as thrust and torque, the iterative error can be estimated using the L_∞-norm. This the maximum difference between each iteration of the quantity. As thrust and torque has one single value for each iteration per, this norm is the difference of thrust for each time step. In Figure 6.4a, the total thrust is shown for $\theta_m = 10°$. The L_∞-norm is shown in Figure 6.4b.

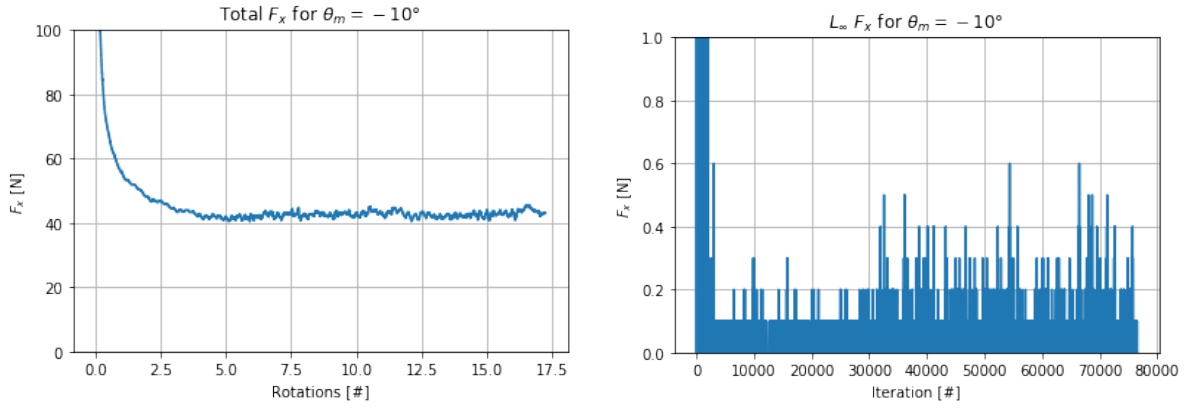

(a) Total thrust for $\theta_m = -10°$

(b) L_∞ for the thrust for $\theta_m = -10°$

Figure 6.4: Total thrust and L_∞ for $\theta_m = -10°$

As shown above, the total thrust force converges to a value around the mean. However, it keeps fluctuating by $1 - 2\%$ of the total value. The same is observed for both other cases. This could partly

declare the fact that trend of increasing thrust for increasing pitch angle is not observed. However, this can not declare the fact that all other forces and moments show the trends that are expected.

As stated by Muscari, Dubbioso, Ortolani, and Di Mascio (2017)), the pitch angle introduces in-plane loads. The side force and horizontal force are zero in straight ahead condition, whilst these forces start increasing for increasing pitch angle. The mean F_y and F_z show a linear increase with the inflow angle, which was also observed by Dubbioso et al. (2013). The in-plane loads, M_y and M_z also show a linear increase. These moments originate from imbalance of the generation of the side and vertical force between propeller blade positions.

6.2.2. Propeller Blade Loads

The numerical simulations allow to extract forces for a single blade, whilst this was not possible in the experiments. For this analysis, the blade that starts at top position is selected. In Figure 6.5, the varying forces and moments are shown for this propeller blade. From Figure 6.5a and 6.5d, which represent thrust and torque generated by the blade, a clear dependency on the pitch angle is shown. Despite, the fact that an increase in thrust is not observed, the dependency on blade position is visible as the force fluctuates periodically during each rotation. Moreover, the fluctuations increase for increasing angle. This shows that even for WASP ships, where the drift angles are small, the varying blade loads show up. For torque, the same observations can be done, with the additional fact that M_x fluctuates around a higher mean value.

The side force and vertical force in Figure 6.5b and 6.5c show that even without a pitch angle, the force fluctuates. However, as the forces fluctuate around zero, these cancel each other. For the pitch angles, a shift of these fluctuations is observed, as the mean is non-zero. The same trends are observed for M_y and M_z, as these can only be non-zero if the forces are not balanced during a propeller rotation.

The imbalance of the generation of F_y and F_z is shown in Figure 6.6. In Figure 6.6b, it is shown that the lower half of the propeller plane generates a side force opposite to the upper half. Here, the magnitudes are not equal with opposite sign, as the force in the lower half is more positive than the force in the upper half is negative. This introduces M_y, which is the moment around the y-axis.

For F_z, the difference is observed between the port side of the propeller plane and the starboard side. Here, the vertical force is the highest in the 90 degrees position and the lowest at the opposite side, at 270 degrees. The magnitude of the vertical force on the port side is lower than on the starboard side and therefore the propeller experiences a net vertical force. M_z is caused by this imbalance, and is therefore distributed the same over the circumferential position as F_z.

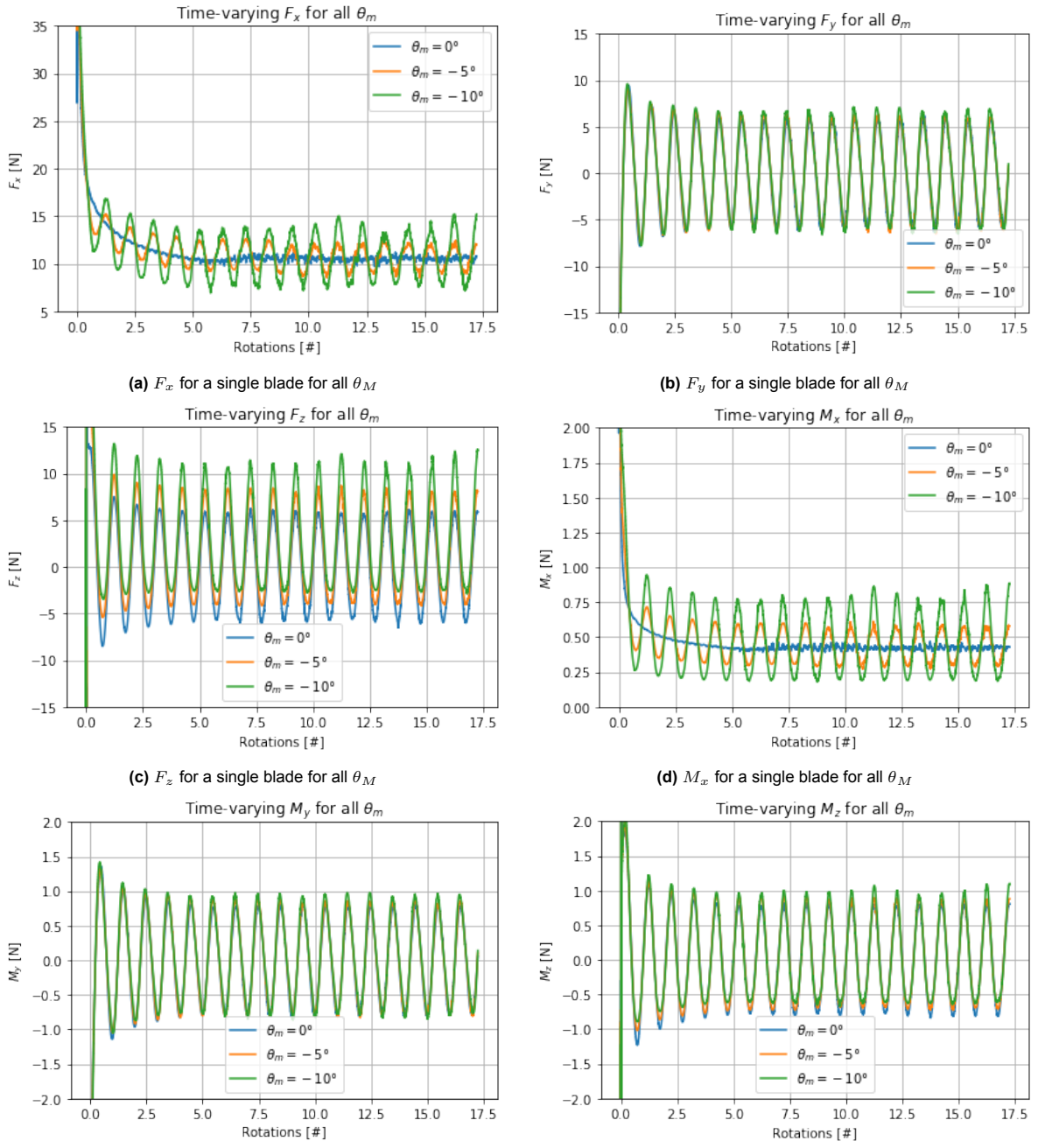

(a) F_x for a single blade for all θ_M

(b) F_y for a single blade for all θ_M

(c) F_z for a single blade for all θ_M

(d) M_x for a single blade for all θ_M

(e) M_y for a single blade for all θ_M

(f) M_z for a single blade for all θ_M

Figure 6.5: F_x, F_y and F_z for a single blade for all θ_M

Figure 6.6a shows the distribution of the thrust over the propeller plane. As already shown in Figure 3.2, the angle of attack varies during the rotation of the propeller. In that figure, the propeller was at a drift angle, with the maximum in the top position. For a pitch angle, the effect is the same as the inflow is going upwards, as in a ship wake. As a result the maximum thrust force can be found close to the 90 degrees position. However, Figure 6.6a shows that this is not exactly at this position but slightly later. This could be ascribed to fact that the propeller is placed downstream of the propeller shaft, this propeller shaft probably changes the local inflow. This will be further analysed using the wake of the propeller.

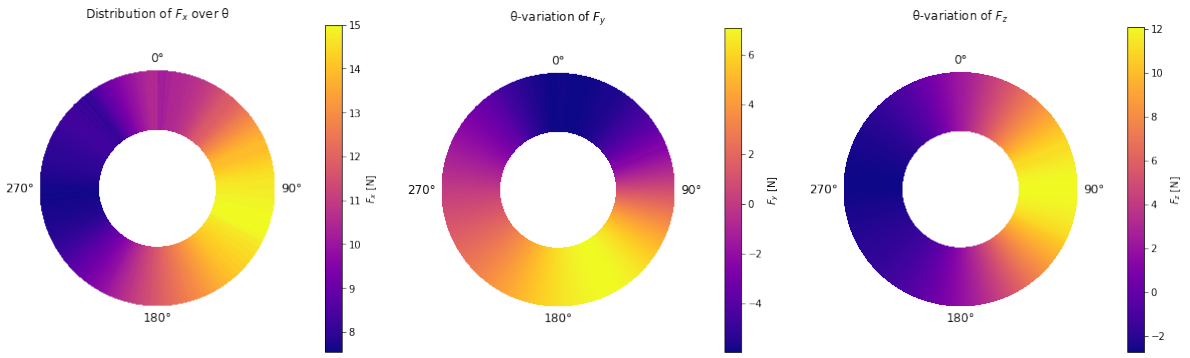

(a) Variation over θ of F_x for $\theta_m = -10°$ **(b)** Variation over θ of F_y for $\theta_m = -10°$ **(c)** Variation over θ of F_z for $\theta_m = -10°$

Figure 6.6: Variation over θ of F_x, F_y and F_z for $\theta_m = -10°$

6.2.3. Wake characteristics

The wake of the propeller is also extracted from the simulations. Firstly, the wake behind the propeller can be compared to LDV measurements of Salvatore et al. (2006). The RMS of the velocity in a plane behind the propeller is shown in Figure 6.7a.

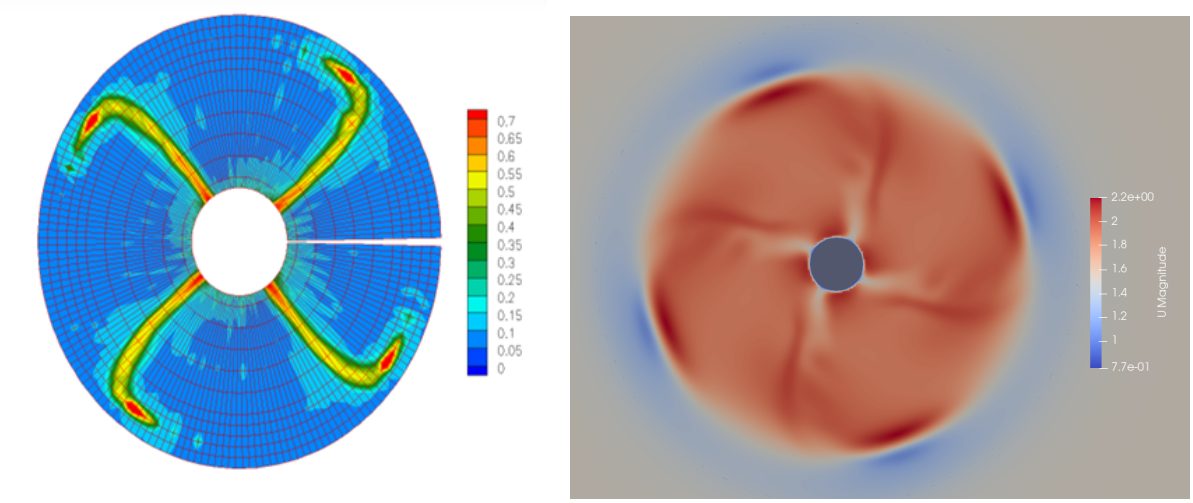

(a) Velocity behind E779A propeller model (Salvatore et al. (2006)) **(b)** Velocity magnitude at $x = 0.25D_p$ behind the propeller for $\theta_m = 0°$

Figure 6.7: Comparison of experimental (Salvatore et al. (2006)) and numerical results of velocity behind the propeller

In Figure 6.7b, the magnitude of the velocity is shown for the case without a pitch angle. Despite the fact that the results are not of good resolution, the same trends can be observed. The high velocities at the location of the propeller tip are captured. Moreover, the higher velocity at the position of the propeller blades is also visible, due to the acceleration of the water there. Also, in both velocity profiles, the velocity close to the tip is slightly lower, whilst it is higher on the leading edge and close to the hub. Therefore, the simulations give comparable results to the LDV measurement of Salvatore et al. (2006), but the resolution is worse.

The influence of the inflow angle on the wake is for example shown in the axial flow velocity component. In Figure 6.8, this flow component is shown for each pitch angle. The shown planes are at the same distance from the propeller, and at the same angle as the propeller.

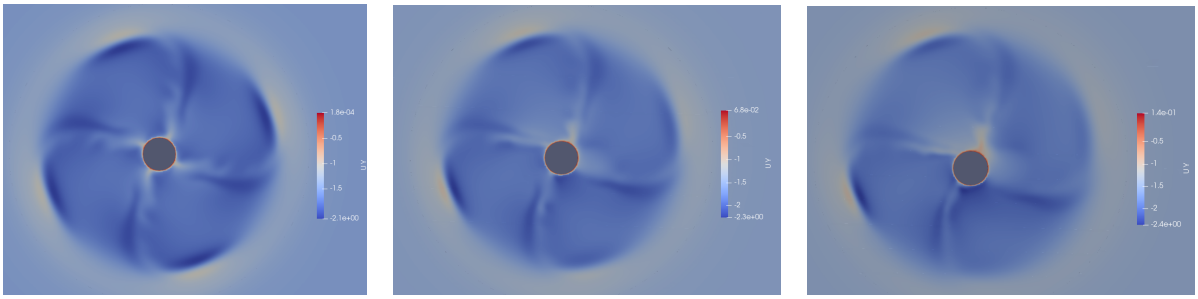

(a) Axial velocity at $x = 0.25D_p$ behind the propeller for $\theta_m = 0°$

(b) Axial velocity at $x = 0.25D_p$ behind the propeller for $\theta_m = -5°$

(c) Axial velocity at $x = 0.25D_p$ behind the propeller for $\theta_m = -10°$

Figure 6.8: Axial velocity at $x = 0.25D_p$ behind the propeller for $\theta_m = 0°$, $\theta_m = -5°$ and $\theta_m = -10°$

From these figures, two main differences can be observed. The maximum velocity, which appears behind the tip, is increasing slightly for increasing θ_m. Also, a small region with a velocity deficit appears close the hub in the 0 degrees position. This is found as the maximum velocity due to the fact that the inflow velocity is defined in negative y-direction. The velocity deficit is a consequence of the propeller shaft moving before the propeller as a result of the inclination. This effect increases for increasing pitch angle, showing that a larger part of the shaft is upstream the propeller, and also influences the flow behind the propeller.

In Figure 6.9, the same axial velocity component is shown as in Figure 6.8. This Figure show that the tip vortices due to a rotation are diffused very quickly. This indicates that the mesh is still to coarse, as velocity and pressure are diffused on a relatively small distance. However, the main flow features are still visible.

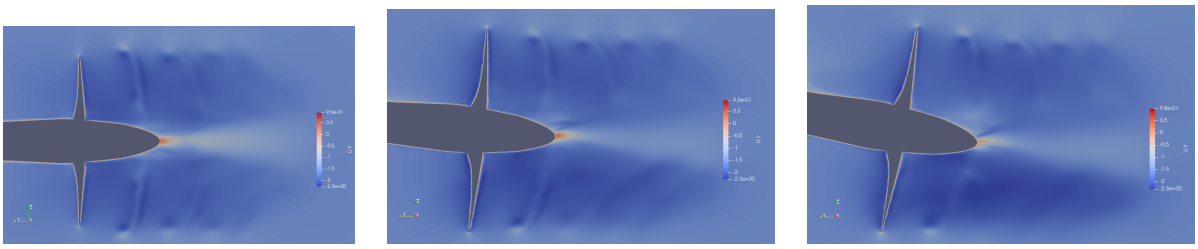

(a) Axial velocity for $\theta_m = 0°$

(b) Axial velocity for $\theta_m = -5°$

(c) Axial velocity for $\theta_m = -10°$

Figure 6.9: Axial velocity for $\theta_m = 0°$, $\theta_m = -5°$ and $\theta_m = -10°$

Here again, the highest velocity is found at the tips of the propeller blades. Moreover, it can be seen that the wake of the propeller is also oriented at an angle due to the pitch angle. This was also observed by Felli and Falchi (2018). Felli and Falchi (2018) found that the hub vortex also follows the inclination. However, this is not observed for these smaller pitch angles. It can also be seen that the direction of the tip vortex is already bended such that it follows the inflow, which is still in negative y-direction around the propeller.

It should be noted that the wake of the propeller is diffusing relatively fast. The iterative errors could give an estimation of the errors based on the residuals here. However, the residuals of both velocity and pressure were not saved during the simulations. Therefore, an estimation cannot be made on convergence based on this iterative error.

Lastly, the thrust distribution at a pitch angle could be shown by the pressure before the propeller. This is pressure is extracted by also defining a plane $0.25D_p$ upstream of the propeller to find the influence of the shaft. In Figure 6.10, the axial velocity component and the pressure of before the propeller are shown.

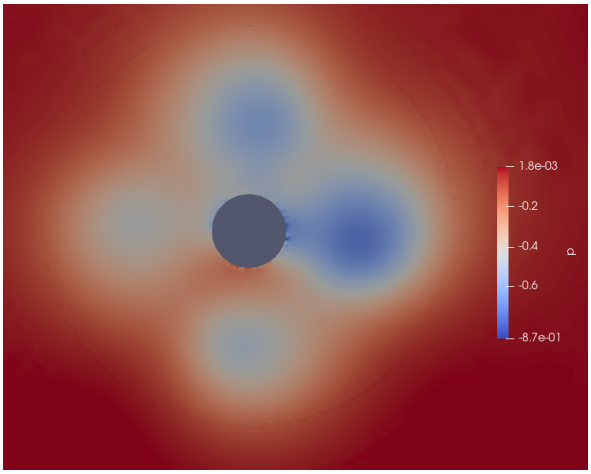

(a) Pressure at $x = -0.25D_P$ before the propeller for $\theta_m = -10°$

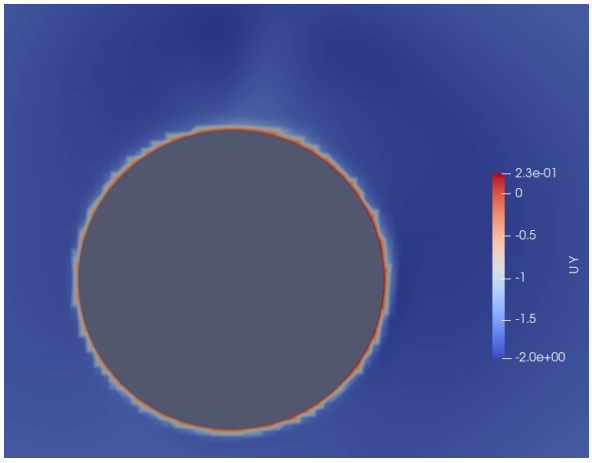

(b) Axial velocity at $x = -0.25D_P$ before the propeller for $\theta_m = -10°$

Figure 6.10: Pressure and axial velocity at $x = -0.25D_P$ before the propeller for $\theta_m = -10°$

From Figure 6.10a, it can be observed that the pressure is the lowest at the positions where the most thrust is generated. The distribution of the pressure shows a similar result as in Figure 6.6a. The lowest pressure is found at and slightly after the 90 degrees position, whilst at $\theta = 270°$ the pressure is relatively high. Figure 6.10b shows the axial velocity component before the propeller. This Figure shows again the velocity deficit in the top position of the propeller plane. However, the region around this deficit shows a slightly higher velocity than at the lower half of the propeller plane. As explained with Figure 3.1, the propeller blade will deliver less thrust when the inflow velocity is increased, as the angle of attack decreases in that case. This effect in combination with the pressure distribution could explain the thrust distribution that is therefore slightly shifted to the lower half, around $\theta = 100$ °.

7

Conclusion & Future research

To conclude this thesis, the research question will be answered:

What are the effects on thrust and torque generated by a marine propeller model, measured experimentally in an open-water environment, under oblique flow conditions and varying loading conditions, imitating typical WASP conditions?

To answer the research question, the sub-question were used as guidelines and their results are summarized shortly.

Experimental set-up
The gondola was used for experimentally determining the thrust and torque of the propeller. The gondola was connected to the HexaPod to adjust its orientation and to be able to set certain drift angles. The gondola was positioned in a pulling configuration, which was needed to reach the propeller in case of problems with the set-up. With this test set-up, and the chosen measurement matrix, the guidelines for open-water tests were followed.

Influence of strut
During the experiments, it was found that the strut upstream influences the performance of the propeller. At small drift angles, both K_T and K_Q showed locally a higher or lower value, depending on the direction of the drift angle. A dependency on J was found for this influence of the strut, as the influence was also observed for higher drift angles at low J. For the largest drift angle, the influence disappeared, as the propeller was not in the wake of the strut anymore. Due to this effect, the experiments were also performed with a pitch angle, which minimised the influence of the strut. This was done as it was found that the propeller showed results without a drift angle that are in good agreement with the reference propeller. This configuration introduced a small wake fraction, due to the propeller shaft.

Uncertainty and frequency analysis of the experiments
The uncertainty of the results showed that the measured signals were noisy. It was shown that the uncertainty of J was dominated by the uncertainty in rotational speed n_p, whilst the uncertainty of both K_T and K_Q was dominated by the fluctuations of the thrust and torque signal respectively. Moreover, when approaching the lower limits of the force transducer, the variations in measured thrust and torque increased. The frequency analysis showed indeed that, besides the shaft frequency and its multiples, including the blade passing frequency, there are some noise frequencies that appear in all measurements. This could be ascribed to vibrations of the structure or the carriage.

Numerical analysis of global and blade loads and wake of the propeller
The numerical analysis, showed an increase in torque for increasing pitch angle. Also the side force and vertical force increase linearly, and therefore also the moments that are caused by the imbalance of these forces. However, the thrust does not show this increase, which could be ascribed to numerical errors. The results showed that even at the smallest pitch angles, both thrust and torque generated by a single blade start to oscillate during a propeller revolution. This behaviour shows that in-plane loads

are also important to take into account for WASP ships, which sail at a small drift angle. Also, the wake of the propeller show the inclination angle and the pressure distribution show the imbalance of

7.1. Answer to research question

The experimental results showed good agreement with observations made in literature. When the pitch angle is increasing, both thrust and torque also increase. The increase is however not significant for small angles, as the differences for both thrust and torque remain below 3% for most advance ratios when comparing the smallest angle with zero angle.

A dependency on the advance ratio is also observed. As mentioned, where the increase for low advance ratios was about 3.78%, for high J, this was observed to be 50.7% and more. This relative difference is not only due to the lower values of K_T and K_Q in this region, but also due to a difference in absolute sense.

However, since the experimental uncertainty is very high, mainly for high J, the observed differences are not fully significant. Especially in the region where propellers of WASP ships will operate mostly, a small drift angle at a high advance ratio, the uncertainty is really more than 150%. However, the results at higher Reynolds numbers showed the same trends, but with significantly less uncertainty. On the contrary, the expected increase in uncertainty, due to variations of the loads of a single propeller blade is not captured by force transducer in any of the measurements. It can be concluded that the experimental results of this work showed the trends of the thrust and torque in an (almost) open-water environment. Blade loads were not measured and also the global thrust and torque did not show signs of the variations in thrust and torque during a revolution. The experiments show that it is possible to capture the influence of both oblique flow and advance ratio on the performance of a propeller. The results also show that some improvements can be made in the test set-up to capture these effects more accurately.

7.2. Future research

There are several topics that could be researched in the future. As stated, the experiments in this work were intended to mimic typical WASP conditions. Therefore, these experiments can be extended in several ways.

Firstly, in-plane moments could be analysed experimentally. In the literature review, see chapter 3, and in the numerical analysis in chapter 6, it was found that the propeller does generate these in-plane loads in oblique flow. It could be interesting to capture the forces and moments experimentally, as this would indicate what effects this would have on the strength of the propeller blades. This could be done by developing a set-up that is lighter than the current set-up, such that the loads in all directions can be measured.

In section 3.3, the interaction between propeller and rudder was introduced. It would be valuable to dive into the interaction of the propeller with the rudder both experimentally and numerically. In experiments this could be done by placing a rudder behind the propeller, to capture the change in forces of the propeller. Moreover, the change in lift and drag on the rudder could be determined.

Lastly, PIV measurements can be performed to also capture the flow characteristics of the propeller in oblique flow. During the experiments described in this thesis, some PIV measurements were already performed simultaneously. It would be interesting to show the interaction of vortices of the propeller with the rudder. This can be done by performing the same experiments with a propeller and a rudder and closely looking at the wake between the propeller and the rudder. Even more realistic set-ups could be considered with a stern profile before the propeller, imitating a situation close to the real world, where both propeller and rudder are affected by the ship hull.

References

Badoe, C. E., Phillips, A. B., & Turnock, S. R. (2015). Influence of drift angle on the computation of hull–propeller–rudder interaction. *Ocean Engineering*, *103*, 64–77. https://doi.org/10.1016/j.oceaneng.2015.04.059

Bernitsas, Ray, & Kinley. (1981, May). *Kt, kq and efficiency curves for the wageningen b-series propellers*. The University of Michigan.

Bruzzone, D., Gaggero, S., Bonvino, C. P., Villa, D., & Viviani, M. (2014). Rudder-propeller interaction: Analysis of different approximation techniques. *Proceedings of the 11thInternational Conference on Hydrodynamics (ICHD 2014)*.

Carlton, J. (2007, January 1). *Marine propellers and propulsion*. https://doi.org/10.1016/b978-0-7506-8150-6.x5000-1

Dubbioso, G., Muscari, R., & Di Mascio, A. (2013). Analysis of the performances of a marine propeller operating in oblique flow. *Computers & Fluids*, *75*, 86–102. https://doi.org/10.1016/j.compfluid.2013.01.017

Eça & Hoekstra. (2006, September). *On the influence of the iterative error in the numerical uncertainty of ship viscous flow calculations*. 26th Symposium on Naval Hydrodynamics.

Eça, L., & Hoekstra, M. (2014). A procedure for the estimation of the numerical uncertainty of CFD calculations based on grid refinement studies. *Journal of Computational Physics*, *262*, 104–130. https://doi.org/10.1016/j.jcp.2014.01.006

Eggers, R. (2019). Parametric variations and performance of wind assisted ship propulsion. *Maritime Research Institute Netherland (MARIN)*.

Felli, M. (2021). Underlying mechanisms of propeller wake interaction with a wing. *Journal of Fluid Mechanics*, *908*, A10. https://doi.org/10.1017/jfm.2020.792

Felli, M., & Falchi, M. (2018). Propeller wake evolution mechanisms in oblique flow conditions. *Journal of Fluid Mechanics*, *845*, 520–559. https://doi.org/10.1017/jfm.2018.232

Felli, M., Roberto, C., & Guj, G. (2009). Experimental analysis of the flow field around a propeller–rudder configuration. *Experiments in Fluids*, *46*(1), 147–164. https://doi.org/10.1007/s00348-008-0550-0

Gaggero, S., Dubbioso, G., Villa, D., Muscari, R., & Viviani, M. (2019). Propeller modeling approaches for off–design operative conditions. *Ocean Engineering*, *178*, 283–305. https://doi.org/10.1016/j.oceaneng.2019.02.069

Gaggero, S., & Villa, D. (2016, October 10). *Advanced openfoam® training*. Retrieved August 21, 2025, from https://www.wolfdynamics.com/training/naval/naval_applications.pdf

Giovannetti, L. M., Olsson, F., Alexandersson, M., Werner, S., & Finnsgård, C. (2020). The effects of hydrodynamic forces on maneuvrability coefficients for wind-assisted ships. *Volume 6A: Ocean Engineering*, V06AT06A051. https://doi.org/10.1115/OMAE2020-18673

Gutsche. (1964). The study of ships' propellers in oblique flow. *Schiffbauforschung*, *3*, 97–122.

Gypa, I., Jansson, M., Gustafsson, R., Werner, S., & Bensow, R. (2023). Controllable-pitch propeller design process for a wind-powered car-carrier optimising for total energy consumption. *Ocean Engineering*, *269*, 113426. https://doi.org/10.1016/j.oceaneng.2022.113426

He, L., & Kinnas, S. A. (2017). Numerical simulation of unsteady propeller/rudder interaction. *International Journal of Naval Architecture and Ocean Engineering*, *9*(6), 677–692. https://doi.org/10.1016/j.ijnaoe.2017.02.004

Heinke, Hellwig-Rieck, & Lübke. (2019). Influence of the reynolds number on the open water characteristics of propellers with short chord lengths. *Sixth International Symposium on Marine Propulsors*.

Hottinger Brüel & Kjær. (2025). *The key to new applications: Precision*. https://www.hbkworld.com/en/knowledge/resource-center/articles/the-key-to-new-applications-precision

Hu, J., Wan, Q., Li, X., Zhang, W., Ning, X., & Duan, C. (2024). Propeller-rudder interaction under different rudder angle. *Ocean Engineering*, *306*, 118104. https://doi.org/10.1016/j.oceaneng.2024.118104

Hu, J., Zhang, W., Sun, S., & Guo, C. (2019). Numerical simulation of vortex–rudder interactions behind the propeller. *Ocean Engineering*, *190*, 106446. https://doi.org/10.1016/j.oceaneng.2019.106446

IMO. (2023). *2023 imo strategy on reduction of ghg emissions from ships*. Retrieved February 4, 2025, from https://www.imo.org/en/OurWork/Environment/Pages/2023-IMO-Strategy-on-Reduction-of-GHG-Emissions-from-Ships.aspx

International Towing Tank Conference. (2021). *Open water test: Ittc recommended procedures and guidelines: 7.5-02-03-02.1* (Technical Report) (Available via ITTC Quality System Manual). International Towing Tank Conference.

ITTC. (2024). *Practical guidelines for rans calculation of nominal wakes*. https://www.ittc.info/media/11966/75-03-03-02.pdf

Kerwin, J. E., Hadler, J. B., & Paulling, J. R. (2010, January 1). *Propulsion*. Society of Naval Architects & Marine Engineers.

Kramer, J. A., Steen, S., & Savio, L. (2016). Drift forces – wingsails vs flettner rotors. *Conference Paper*.

Liu, J., & Hekkenberg, R. (2017). Sixty years of research on ship rudders: Effects of design choices on rudder performance. *Ships and Offshore Structures*, *12*(4), 495–512. https://doi.org/10.1080/17445302.2016.1178205

Longo, J., & Stern, F. (2002). Effects of drift angle on model ship flow. *Experiments in Fluids*, *32*(5), 558–569. https://doi.org/10.1007/s00348-001-0397-0

Lücke, T. (n.d.). Propeller and rudder in off-design conditions. *Third International Symposium on Marine Propulsors*.

Marcu, O., & Robe-Voinea, E.-G. (2024). Stern flow hydrodynamics around a self-propelled maneuvering VLCC ship. *Engineering, Technology & Applied Science Research*, *14*(4), 15283–15290. https://doi.org/10.48084/etasr.7624

Molland, A. F., & Turnock, S. R. (2002). Flow straightening effects on a ship rudder due to upstream propeller and hull.

Molland, A. F., & Turnock. (2007, January 1). *Marine rudders and control surfaces: Principles, data, design and applications*. https://eprints.soton.ac.uk/48364/

Morteza Javadpour, S., Eskafi Noghani, A., Ghassemi, H., & Molyneux, D. (2019). Hydrodynamic characteristics of the propeller-rudder interaction by RANS solver. *American Journal of Mechanical Engineering*, *7*(1), 35–40. https://doi.org/10.12691/ajme-7-1-4

Muscari, R., Dubbioso, G., Ortolani, F., & Di Mascio, A. (2017). CFD analysis of the sensitivity of propeller bearing loads to stern appendages and propulsive configurations. *Applied Ocean Research*, *69*, 205–219. https://doi.org/10.1016/j.apor.2017.11.004

Muscari, R., Dubbioso, G., Viviani, M., & Di Mascio, A. (2017). Analysis of the asymmetric behavior of propeller–rudder system of twin screw ships by CFD. *Ocean Engineering*, *143*, 269–281. https://doi.org/10.1016/j.oceaneng.2017.07.056

National Instruments. (2006, August 31). *Understanding ffts and windowing*. https://www.ni.com/en/shop/data-acquisition/measurement-fundamentals/analog-fundamentals/understanding-ffts-and-windowing.html?srsltid=AfmBOoogSXhXxjpLB6-mRm95fM3s8Q3kHrniWac8PfMyGAQfZELzTp8x

Olsson, F., Giovannetti, L., Werner, S., & Finnsgård, C. (2020). A performance depowering investigation for wind powered cargo ships along a route. *Journal of Sailing Technology*, *5*(1), 47–60. https://doi.org/10.5957/jst/2020.3.1.47

Openfoam (comp. software; Version v2412). (2024, December 24). https://www.openfoam.com/

Ortolani, F., & Dubbioso, G. (2019). Experimental investigation of blade and propeller loads: Steady turning motion. *Applied Ocean Research*, *91*, 101874. https://doi.org/10.1016/j.apor.2019.101874

Ortolani, F., Dubbioso, G., Muscari, R., Mauro, S., & Di Mascio, A. (2018). Experimental and numerical investigation of propeller loads in off-design conditions. *Journal of Marine Science and Engineering*, *6*(2), 45. https://doi.org/10.3390/jmse6020045

Ortolani, F., Viviani, M., Tani, G., & Dubbioso, G. (2020). Experimental investigation of single blade loads by captive model tests in pure oblique flow. *Ocean Engineering*, *196*, 106789. https://doi.org/10.1016/j.oceaneng.2019.106789

Paar, A. (2025). Viscosity of Water. https://wiki.anton-paar.com/en/water/

Perez, T., & Blanke, M. (2002). Mathematical ship modeling for control applications. *DTU Library*. https://backend.orbit.dtu.dk/ws/files/137166308/Mathematical_Ship_Modeling_for_Control_Applications_Perez_Blanke.pdf

Phillips, A. B., Turnock, S. R., & Furlong, M. (2010). Accurate capture of propeller-rudder interaction using a coupled blade element momentum-RANS approach. *Ship Technology Research*, *57*(2), 128–139. https://doi.org/10.1179/str.2010.57.2.005

Pope, S. B. (2000, August 10). *Turbulent flows*. https://doi.org/10.1017/cbo9780511840531

Propeller, screw propeller. (n.d.). https://www.wartsila.com/encyclopedia/term/propeller-screw-propeller

Reducing emissions from the shipping sector. (n.d.). Retrieved February 4, 2025, from https://climate.ec.europa.eu/eu-action/transport/reducing-emissions-shipping-sector_en

Rijpkema, D., Starke, B., & Bosschers, J. (2013). Numerical simulation of propeller-hull interaction and determination of the effective wake field using a hybrid RANS-BEM approach.

Salvatore, F., Francisco, A. P., Felli, M., Calcagni, D., & Fabio, D. F. (2006, June 15). *Description of the insean e779a propeller experimental dataset*. INSEAN. https://doi.org/10.5281/zenodo.6077997

Savitzky, A., & Golay, M. J. E. (1964). Smoothing and differentiation of data by simplified least squares procedures. *Analytical Chemistry*, *36*(8), 1627–1639. https://doi.org/10.1021/ac60214a047

Scipy v1.16.2 manual. (2008). Retrieved September 17, 2025, from https://docs.scipy.org/doc/scipy/reference/generated/scipy.signal.windows.hamming.html#scipy.signal.windows.hamming

Shamsi, R., & Ghassemi, H. (2017). Determining the hydrodynamic loads of the marine propeller forces in oblique flow and off-design condition. *Iranian Journal of Science and Technology, Transactions of Mechanical Engineering*, *41*(2), 121–127. https://doi.org/10.1007/s40997-016-0049-x

Steimel & Humbolt. (2025, July 15). *Statistical analysis of data for engineers*. LibreTexts. https://eng.libretexts.org/Courses/California_State_Polytechnic_University_Humboldt/Statistical_Analysis_of_Data_for_Engineers

Struijk, G. D. (2015). Hydrodynamics of wind-assisted ships. *TU Delft Repository*.

Sun, S., Li, L., Wang, C., & Zhang, H. (2018). Numerical prediction analysis of propeller exciting force for hull–propeller–rudder system in oblique flow. *International Journal of Naval Architecture and Ocean Engineering*, *10*(1), 69–84. https://doi.org/10.1016/j.ijnaoe.2017.03.005

Sun, S., Zhang, Y., Guo, Z., Li, X., & Huang, Z. (2023). Research on propeller bearing force of a four-screw ship in oblique flow. *Ocean Engineering*, *276*, 114164. https://doi.org/10.1016/j.oceaneng.2023.114164

Thies, F., & Ringsberg, J. W. (2023). Retrofitting WASP to a RoPax vessel—design, performance and uncertainties. *Energies*, *16*(2), 673. https://doi.org/10.3390/en16020673

Tillig, F., & Ringsberg, J. W. (2020). Design, operation and analysis of wind-assisted cargo ships. *Ocean Engineering*, *211*, 107603. https://doi.org/10.1016/j.oceaneng.2020.107603

Towing tank no. 1. (2025). Retrieved July 21, 2025, from https://www.tudelft.nl/me/over/afdelingen/maritime-and-transport-technology/research/ship-hydromechanics/facilities/towing-tank-no-1

Tupper, E. C. (2013, January 1). *Resistance* (5th ed.). https://www.sciencedirect.com/science/article/pii/B9780080982373000175

Villa, D., Franceschi, A., & Viviani, M. (2020). Numerical analysis of the rudder–propeller interaction. *Journal of Marine Science and Engineering*, *8*(12), 990. https://doi.org/10.3390/jmse8120990

Wang, C., Sun, S., Sun, S., & Li, L. (2017). Numerical analysis of propeller exciting force in oblique flow. *Journal of Marine Science and Technology*, *22*(4), 602–619. https://doi.org/10.1007/s00773-017-0431-4

Wang, L., Guo, C., Xu, P., & Su, Y. (2019). Analysis of the wake dynamics of a propeller operating before a rudder. *Ocean Engineering*, *188*, 106250. https://doi.org/10.1016/j.oceaneng.2019.106250

Wang, L., Liu, X., Guo, J., Li, M., & Liao, J. (2023). The dynamic characteristics in the wake systems of a propeller operating under different loading conditions. *Ocean Engineering*, *286*, 115518. https://doi.org/10.1016/j.oceaneng.2023.115518

Werner, S., Papanikolaou, A., Fagergren, C., Dessen, L., Kuttenkeuler, J., Santén, V., & Steinbach, C. (2023). The orcelle project – towards wind-powered ships for deep sea cargo transport. *September 28, 2023*, D021S002R008. https://doi.org/10.5957/SMC-2023-089

Wolf Dynamics. (2017). *Openfoam - naval applications*. Retrieved August 21, 2025, from https://www.wolfdynamics.com/tutorials.html?id=178

Woud, H. K., & Stapersma, D. (2002, January 1). *Design of propulsion and electric power generation systems*. http://ci.nii.ac.jp/ncid/BA64216262

Yao, J. (2015). Investigation on hydrodynamic performance of a marine propeller in oblique flow by RANS computations. *International Journal of Naval Architecture and Ocean Engineering*, *7*(1), 56–69. https://doi.org/10.1515/ijnaoe-2015-0005

Zhang, Q., Jaiman, R. K., Ma, P., & Liu, J. (2020). Investigation on the performance of a ducted propeller in oblique flow. *Journal of Offshore Mechanics and Arctic Engineering*, *142*(1), 011801. https://doi.org/10.1115/1.4043943

Zhang, Y., Hudson, D., Windén, B., & Turnock, S. (n.d.). Evaluating the effects of drift angle on the self-propelled ship using blade element momentum theory.

Zhang, Y.-x., Chen, K., & Jiang, D.-p. (2020). CFD analysis of the lateral loads of a propeller in oblique flow. *Ocean Engineering*, *202*, 107153. https://doi.org/10.1016/j.oceaneng.2020.107153

Zhang & Zhang. (2022, October). *Numerical prediction of propeller tip vortex cavitation inception and the influence of water quality*. 7th Internationa; Symposium of Marine Propulsors. https://www.marinepropulsors.com/proceedings/2022/3-2-3.pdf

8

Appendix A: Parameter choices

In this Appendix, the results of the estimations described in Chapter 4 are shown. The measurement matrix is based on the results presented in this appendix. Red indicates that a combination is not possible or sufficient according to ITTC guidelines (International Towing Tank Conference (2021)). In Table 8.1, the rotational speed n_p is shown for all combinations of carriage speed and advance coefficient J. These are calculated using formula 2.2. In Table 8.2, the Reynolds number for all combinations of carriage speed and advance coefficient J. These are calculated according to formula 2.14

Table 8.1: Possible RPM for different combinations of velocity and advance coefficient

V_A[m/s] \ J[-]	0.1	0.2	0.3	0.4	0.5	0.6	0.7	0.8	0.9	1.0	1.1
0.5	1380.008	690.0041	460.0028	345.0021	276.0017	230.0014	197.1440	172.5010	153.3343	138.0008	125.4553
1.0	2760.017	1380.008	920.0055	690.0041	552.0033	460.0028	394.2881	345.0021	306.6685	276.0017	250.9106
1.5	4140.025	2070.012	1380.008	1035.006	828.0050	690.0041	591.4321	517.5031	460.0028	414.0025	376.3659
2.0	5520.033	2760.017	1840.011	1380.008	1104.006	920.0055	788.5762	690.0041	613.3370	552.0033	501.8212
2.5	6900.041	3450.021	2300.014	1725.010	1380.008	1150.006	985.7202	862.5052	766.6713	690.0041	627.2765
3.0	8280.050	4140.025	2760.017	2070.012	1656.0099	1380.008	1182.864	1035.006	920.0055	828.0050	752.7318
3.5	9660.058	4830.029	3220.019	2415.014	1932.011	1610.010	1380.008	1207.507	1073.340	966.0058	878.1871
4.0	11040.066	5520.033	3680.022	2760.017	2208.013	1840.011	1577.152	1380.008	1226.674	1104.007	1003.642
4.5	12420.075	6210.037	4140.025	3105.019	2484.015	2070.012	1774.296	1552.509	1380.008	1242.007	1129.098
5.0	13800.083	6900.041	4600.028	3450.021	2760.017	2300.014	1971.440	1725.010	1533.343	1380.008	1254.553
5.5	15180.091	7590.046	5060.030	3795.023	3036.018	2530.015	2168.584	1897.511	1686.677	1518.009	1380.008
6.0	16560.099	8280.050	5520.033	4140.025	3312.020	2760.017	2365.728	2070.012	1840.011	1656.010	1505.464
6.5	17940.108	8970.054	5980.036	4485.027	3588.022	2990.018	2562.873	2242.513	1993.345	1794.011	1630.919
7.0	19320.116	9660.058	6440.039	4830.029	3864.023	3220.019	2760.017	2415.014	2146.680	1932.012	1756.374

Table 8.2: Possible Reynolds numbers for different combinations of velocity and advance coefficient

V_A[m/s] \ J[-]	0.1	0.2	0.3	0.4	0.5	0.6	0.7	0.8	0.9	1.0	1.1	1.2
0.5	$8.26 \cdot 10^5$	$4.14 \cdot 10^5$	$2.77 \cdot 10^5$	$2.10 \cdot 10^5$	$1.69 \cdot 10^5$	$1.42 \cdot 10^5$	$1.24 \cdot 10^5$	$1.10 \cdot 10^5$	$9.90 \cdot 10^4$	$9.06 \cdot 10^4$	$8.38 \cdot 10^4$	$7.83 \cdot 10^4$
1.0	$1.65 \cdot 10^6$	$8.28 \cdot 10^5$	$5.55 \cdot 10^5$	$4.19 \cdot 10^5$	$3.38 \cdot 10^5$	$2.85 \cdot 10^5$	$2.47 \cdot 10^5$	$2.19 \cdot 10^5$	$1.98 \cdot 10^5$	$1.81 \cdot 10^5$	$1.68 \cdot 10^5$	$1.57 \cdot 10^5$
1.5	$2.48 \cdot 10^6$	$1.24 \cdot 10^6$	$8.32 \cdot 10^5$	$6.29 \cdot 10^5$	$5.07 \cdot 10^5$	$4.27 \cdot 10^5$	$3.71 \cdot 10^5$	$3.29 \cdot 10^5$	$2.97 \cdot 10^5$	$2.72 \cdot 10^5$	$2.51 \cdot 10^5$	$2.35 \cdot 10^5$
2.0	$3.30 \cdot 10^6$	$1.66 \cdot 10^6$	$1.11 \cdot 10^6$	$8.38 \cdot 10^5$	$6.77 \cdot 10^5$	$5.70 \cdot 10^5$	$4.95 \cdot 10^5$	$4.39 \cdot 10^5$	$3.96 \cdot 10^5$	$3.62 \cdot 10^5$	$3.35 \cdot 10^5$	$3.13 \cdot 10^5$
2.5	$4.13 \cdot 10^6$	$2.07 \cdot 10^6$	$1.39 \cdot 10^6$	$1.05 \cdot 10^6$	$8.46 \cdot 10^5$	$7.12 \cdot 10^5$	$6.18 \cdot 10^5$	$5.48 \cdot 10^5$	$4.95 \cdot 10^5$	$4.53 \cdot 10^5$	$4.19 \cdot 10^5$	$3.91 \cdot 10^5$
3.0	$4.95 \cdot 10^6$	$2.48 \cdot 10^6$	$1.66 \cdot 10^6$	$1.26 \cdot 10^6$	$1.01 \cdot 10^6$	$8.55 \cdot 10^5$	$7.42 \cdot 10^5$	$6.58 \cdot 10^5$	$5.94 \cdot 10^5$	$5.44 \cdot 10^5$	$5.03 \cdot 10^5$	$4.70 \cdot 10^5$
3.5	$5.78 \cdot 10^6$	$2.90 \cdot 10^6$	$1.94 \cdot 10^6$	$1.47 \cdot 10^6$	$1.18 \cdot 10^6$	$9.97 \cdot 10^5$	$8.65 \cdot 10^5$	$7.68 \cdot 10^5$	$6.93 \cdot 10^5$	$6.34 \cdot 10^5$	$5.87 \cdot 10^5$	$5.48 \cdot 10^5$
4.0	$6.60 \cdot 10^6$	$3.31 \cdot 10^6$	$2.22 \cdot 10^6$	$1.68 \cdot 10^6$	$1.35 \cdot 10^6$	$1.14 \cdot 10^6$	$9.89 \cdot 10^5$	$8.78 \cdot 10^5$	$7.92 \cdot 10^5$	$7.25 \cdot 10^5$	$6.71 \cdot 10^5$	$6.26 \cdot 10^5$
4.5	$7.43 \cdot 10^6$	$3.73 \cdot 10^6$	$2.50 \cdot 10^6$	$1.89 \cdot 10^6$	$1.52 \cdot 10^6$	$1.28 \cdot 10^6$	$1.11 \cdot 10^6$	$9.87 \cdot 10^5$	$8.91 \cdot 10^5$	$8.15 \cdot 10^5$	$7.54 \cdot 10^5$	$7.05 \cdot 10^5$
5.0	$8.26 \cdot 10^6$	$4.14 \cdot 10^6$	$2.77 \cdot 10^6$	$2.10 \cdot 10^6$	$1.69 \cdot 10^6$	$1.42 \cdot 10^6$	$1.24 \cdot 10^6$	$1.10 \cdot 10^6$	$9.90 \cdot 10^5$	$9.06 \cdot 10^5$	$8.38 \cdot 10^5$	$7.83 \cdot 10^5$
5.5	$9.08 \cdot 10^6$	$4.55 \cdot 10^6$	$3.05 \cdot 10^6$	$2.31 \cdot 10^6$	$1.86 \cdot 10^6$	$1.57 \cdot 10^6$	$1.36 \cdot 10^6$	$1.21 \cdot 10^6$	$1.09 \cdot 10^6$	$9.97 \cdot 10^5$	$9.22 \cdot 10^5$	$8.61 \cdot 10^5$
6.0	$9.91 \cdot 10^6$	$4.97 \cdot 10^6$	$3.33 \cdot 10^6$	$2.51 \cdot 10^6$	$2.03 \cdot 10^6$	$1.71 \cdot 10^6$	$1.48 \cdot 10^6$	$1.32 \cdot 10^6$	$1.19 \cdot 10^6$	$1.09 \cdot 10^6$	$1.01 \cdot 10^6$	$9.39 \cdot 10^5$
6.5	$1.07 \cdot 10^7$	$5.38 \cdot 10^6$	$3.61 \cdot 10^6$	$2.72 \cdot 10^6$	$2.20 \cdot 10^6$	$1.85 \cdot 10^6$	$1.61 \cdot 10^6$	$1.43 \cdot 10^6$	$1.29 \cdot 10^6$	$1.18 \cdot 10^6$	$1.09 \cdot 10^6$	$1.02 \cdot 10^6$
7.0	$1.16 \cdot 10^7$	$5.80 \cdot 10^6$	$3.88 \cdot 10^6$	$2.93 \cdot 10^6$	$2.37 \cdot 10^6$	$1.99 \cdot 10^6$	$1.73 \cdot 10^6$	$1.54 \cdot 10^6$	$1.39 \cdot 10^6$	$1.27 \cdot 10^6$	$1.17 \cdot 10^6$	$1.10 \cdot 10^6$

Table 8.3 shows the estimated thrust generated by the propeller. This calculation is based on the open-water characteristics of the Wageningen B4-70 propeller (Bernitsas et al. (1981)). It shows which thrust forces can be measured safely with the force transducer.

Table 8.3: Estimated thrust [N] for different combinations of velocity and advance coefficient

V_A[m/s] \ J[-]	0.1	0.2	0.3	0.4	0.5	0.6	0.7	0.8	0.9	1.0
0.5	496.21	115.19	45.95	22.89	12.76	7.55	4.58	2.22	1.17	0.47
1.0	1984.85	460.77	183.78	91.56	51.04	30.19	18.32	8.86	4.67	1.89
1.5	4465.92	1036.73	413.51	206.02	114.84	67.93	41.23	19.94	10.50	4.25
2.0	7939.41	1843.08	735.13	366.25	204.16	120.77	73.30	35.44	18.67	7.56
2.5	12405.33	2879.81	1148.64	572.27	318.99	188.71	114.53	55.38	29.17	11.81
3.0	17863.68	4146.93	1654.04	824.07	459.35	271.74	164.92	79.75	42.01	17.01
3.5	24314.45	5644.43	2251.34	1121.65	625.23	369.86	224.48	108.55	57.18	23.16
4.0	31757.65	7372.31	2940.52	1465.01	816.63	483.09	293.20	141.78	74.68	30.25
4.5	40193.28	9330.58	3721.60	1854.15	1033.54	611.41	371.07	179.43	94.52	38.28
5.0	49621.33	11519.24	4594.57	2289.08	1275.98	754.82	458.12	221.52	116.69	47.26
5.5	60041.81	13938.28	5559.43	2769.79	1543.93	913.33	554.32	268.04	141.19	57.18
6.0	71454.72	16587.70	6616.18	3296.27	1837.41	1086.94	659.69	318.99	168.03	68.05
6.5	83860.05	19467.51	7764.82	3868.54	2156.40	1275.65	774.22	374.38	197.20	79.87
7.0	97257.81	22577.71	9005.35	4486.60	2500.92	1479.45	897.91	434.19	228.71	92.63

Table 8.4 shows the estimated torque generated by the propeller. This calculation is also based on the open-water characteristics of the Wageningen B4-70 propeller (Bernitsas et al. (1981)). It shows which amount of torque can be measured safely with the force transducer.

Table 8.4: Estimated torque [Nm] for different combinations of velocity and advance coefficient

V_A[m/s] \ J[-]	0.1	0.2	0.3	0.4	0.5	0.6	0.7	0.8	0.9	1.0
0.5	15.41	3.72	1.54	0.80	0.43	0.27	0.17	0.10	0.06	0.04
1.0	61.64	14.90	6.16	3.21	1.73	1.08	0.67	0.42	0.25	0.15
1.5	138.69	33.52	13.87	7.22	3.88	2.44	1.51	0.94	0.57	0.35
2.0	246.56	59.59	24.66	12.84	6.90	4.34	2.68	1.67	1.01	0.62
2.5	385.26	93.10	38.53	20.07	10.79	6.78	4.19	2.61	1.59	0.96
3.0	554.77	134.07	55.48	28.89	15.53	9.76	6.04	3.76	2.28	1.39
3.5	755.10	182.48	75.51	39.33	21.14	13.28	8.22	5.11	3.11	1.89
4.0	986.26	238.35	98.63	51.37	27.62	17.35	10.73	6.68	4.06	2.47
4.5	1248.23	301.66	124.82	65.01	34.95	21.96	13.59	8.45	5.14	3.12
5.0	1541.03	372.41	154.10	80.26	43.15	27.11	16.77	10.43	6.34	3.85
5.5	1864.64	450.62	186.46	97.12	52.21	32.80	20.30	12.63	7.67	4.66
6.0	2219.08	536.28	221.91	115.58	62.13	39.04	24.15	15.03	9.13	5.55
6.5	2604.33	629.38	260.43	135.64	72.92	45.82	28.35	17.63	10.72	6.51
7.0	3020.41	729.93	302.04	157.31	84.57	53.14	32.88	20.45	12.43	7.55

9

Appendix B: Measurement results

In this Appendix, the mean values of thrust and torque for all measurements are given. The tables are sorted based on V_A, the use of β_m or θ_m and thrust and torque coefficient are presented in different tables.

In Table 9.1, the values for K_T are given for all drift angles β_m at $V_A = 1.5$ m/s.

Table 9.1: Mean values of measured trust coefficient K_T, $V_A = 1.5$ m/s

J[-] \ β_m[deg]	-15	-10	-5	0	5	10	15
0.43	0.2956	0.2973	0.2956	0.2847	0.2801	0.2782	0.2936
0.50	0.2665	0.2706	0.2719	0.2585	0.2454	0.2539	0.2675
0.60	0.2252	0.2280	0.2336	0.2166	0.2048	0.2190	0.2268
0.70	0.1857	0.1853	0.1932	0.1747	0.1628	0.1794	0.1863
0.80	0.1452	0.1431	0.1532	0.1335	0.1208	0.1374	0.1461
0.90	0.0987	0.0967	0.1071	0.0869	0.0745	0.0917	0.1020
1.00	0.0532	0.0455	0.0570	0.0349	0.0237	0.0404	0.0534
1.10	-0.0056	-0.0104	0.0021	-0.0193	-0.0314	-0.0144	-0.0001

In Table 9.2, the values for $10K_Q$ are given for all drift angles β_m at $V_A = 1.5$ m/s.

Table 9.2: Mean values of measured torque coefficient $10K_Q$, $V_A = 1.5$ m/s

J[-] \ β_m[deg]	-15	-10	-5	0	5	10	15
0.43	0.4895	0.4950	0.4969	0.4791	0.4682	0.4783	0.4893
0.50	0.4493	0.4549	0.4595	0.4386	0.4226	0.4393	0.4501
0.60	0.3921	0.3949	0.4023	0.3798	0.3620	0.3837	0.3928
0.70	0.3348	0.3352	0.3457	0.3202	0.3011	0.3260	0.3361
0.80	0.2745	0.2719	0.2847	0.2557	0.2373	0.2642	0.2758
0.90	0.2087	0.2053	0.2202	0.1936	0.1745	0.1996	0.2124
1.00	0.1422	0.1343	0.1551	0.1236	0.1033	0.1288	0.1443
1.10	0.0601	0.0555	0.0789	0.0439	0.0218	0.0502	0.0688

In Table 9.3, the values for K_T are given for all drift angles β_m at $V_A = 3.5$ m/s.

Table 9.3: Mean values of measured trust coefficient K_T, $V_A = 3.5$ m/s

β_m[deg] / J[-]	-15	-10	-5	0	5	10	15
0.77	-	-	-	0.1349	-	-	-
0.80	0.1376	0.1317	0.1336	0.1197	0.1123	0.1262	0.1361
0.90	0.0939	0.0854	0.0895	0.0761	0.0689	0.0828	0.0950
1.00	0.0480	0.0416	0.0446	0.0297	0.0230	0.0373	0.0516
1.10	0.0004	-0.0078	-0.0045	-0.0192	-0.0290	-0.0125	0.0018

In Table 9.4, the values for $10K_Q$ are given for all drift angles β_m at $V_A = 3.5$ m/s.

Table 9.4: Mean values of measured torque coefficient $10K_Q$, $V_A = 3.5$ m/s

β_m[deg] / J[-]	-15	-10	-5	0	5	10	15
0.77	-	-	-	0.2876	-	-	-
0.80	0.2893	0.2828	0.2868	0.2661	0.2537	0.2760	0.2886
0.90	0.2268	0.4363	0.2253	0.2039	0.1905	0.2121	0.2287
1.00	0.1588	0.1519	0.1596	0.1342	0.1211	0.1447	0.1646
1.10	0.0872	0.0769	0.0849	0.0582	0.0408	0.0693	0.0902

In Table 9.5, the values for K_T are given for all drift angles θ_m at $V_A = 1.5$ m/s.

Table 9.5: Mean values of measured trust coefficient K_T, $V_A = 1.5$ m/s

θ_m[deg] / J[-]	0	5	10	15
0.43	0.2847	0.2897	0.2925	0.2954
0.50	0.2585	0.2597	0.2645	0.2676
0.60	0.2166	0.2181	0.2234	0.2265
0.70	0.1747	0.1766	0.1824	0.1851
0.80	0.1335	0.1354	0.1413	0.1458
0.90	0.0869	0.0885	0.0966	0.1005
1.00	0.0349	0.0381	0.0466	0.0526
1.10	-0.0193	-0.0178	-0.0075	-0.0015

In Table 9.6, the values for $10K_Q$ are given for all drift angles θ_m at $V_A = 1.5$ m/s.

Table 9.6: Mean values of measured torque coefficient $10K_Q$, $V_A = 1.5$ m/s

θ_m[deg] / J[-]	0	5	10	15
0.43	0.4791	0.4830	0.4868	0.4905
0.50	0.4386	0.4396	0.4458	0.4511
0.60	0.3798	0.3805	0.3882	0.3932
0.70	0.3202	0.3218	0.3299	0.3345
0.80	0.2557	0.2588	0.2686	0.2759
0.90	0.1936	0.1947	0.2050	0.2111
1.00	0.1236	0.1268	0.1383	0.1433
1.10	0.0439	0.0465	0.0611	0.0668

In Table 9.7, the values for K_T are given for all drift angles θ_m at $V_A = 3.5$ m/s.

Table 9.7: Mean values of measured trust coefficient K_T, $V_A = 3.5$ m/s

θ_m[deg] / J[-]	0	5	10	15
0.77	0.1349	-	-	-
0.80	0.1197	0.1234	0.1307	0.1373
0.90	0.0761	0.0791	0.0881	0.0950
1.00	0.0297	0.0348	0.0430	0.0508
1.10	-0.0192	-0.0149	-0.0073	0.0025

In Table 9.8, the values for $10K_Q$ are given for all drift angles θ_m at $V_A = 3.5$ m/s.

Table 9.8: Mean values of measured torque coefficient $10K_Q$, $V_A = 3.5$ m/s

θ_m[deg] / J[-]	0	5	10	15
0.77	0.2876	-	-	-
0.80	0.2661	0.2709	0.2811	0.2910
0.90	0.2039	0.2079	0.2205	0.2298
1.00	0.1342	0.1418	0.1542	0.1650
1.10	0.0582	0.0657	0.0783	0.0928

10

Appendix C: Discretization Schemes & Solvers

The discretization schemes and solvers used during the simulations, described in Chapter 6, are shown in this appendix. Firstly, the fvSchemes file from the OpenFOAM case is shown. Thereafter the fvSolution file is given.

fvSchemes:

```
ddtSchemes
{
    default         Euler;
}

gradSchemes
{
    default         Gauss linear;
    grad(p)         Gauss linear;
    grad(U)         cellLimited Gauss linear 1;
}

divSchemes
{
    default         none;

    div(phi,U)      Gauss linearUpwind grad(U);

    turbulence      Gauss upwind;
    div(phi,k)      $turbulence;
    div(phi,epsilon) $turbulence;

    div((nuEff*dev2(T(grad(U))))) Gauss linear;
}

laplacianSchemes
{
    default         Gauss linear limited corrected 0.33;
}

interpolationSchemes
{
    default         linear;
}

snGradSchemes
{
    default         limited corrected 0.33;
}
```

fvSolution:

```
solvers
{
    "pcorr.*"
    {
        solver          GAMG;
        tolerance       1e-8;
        relTol          0.01;
        smoother        DICGaussSeidel;
        cacheAgglomeration true;
        nCellsInCoarsestLevel 10;
        agglomerator faceAreaPair;
        mergeLevels 1;
        maxIter         50;
    }

    p
    {
        $pcorr;
        tolerance       1e-5;
        relTol          0.01;
    }

    pFinal
    {
        $p;
        tolerance       1e-6;
        relTol          0;
    }

    "(U|k|epsilon)"
    {
        solver          smoothSolver;
        smoother        symGaussSeidel;
        tolerance       1e-6;
        relTol          0.1;
    }

    "(U|k|epsilon)Final"
    {
        solver          smoothSolver;
        smoother        symGaussSeidel;
        tolerance       1e-6;
        relTol          0;
    }
    "cellDisplacement.*"
    {
        solver          GAMG;
        smoother        GaussSeidel;
        tolerance       1e-09;
        relTol          0;
    }
    yPsi
    {
         solver         GAMG;
         smoother       GaussSeidel;
         tolerance      1e-09;
         relTol         0.0;
    }
    yPsiFinal
    {
         $yPsi;
    }
    Phi
    {
         solver          GAMG;
         smoother        DIC;
         tolerance       1e-06;
         relTol          0.01;
    }
```

```
70
71 }
72
73 PIMPLE
74 {
75     correctPhi          no;
76     nOuterCorrectors    2;
77     nCorrectors         2;
78     nNonOrthogonalCorrectors 2;
79 }
80
81 relaxationFactors
82 {
83     "(U|k|epsilon).*"   0.7;
84 }
85
86 cache
87 {
88     grad(U);
89 }
```

11

Appendix D: Approximation method of Gutsche

In this appendix, the calculation used to find the approximation for K_T and K_Q based on the propeller open-water characteristic is presented. This approximation method is developed by Gutsche, based on experimental results of propellers is an open-water environment with and without an inclination angle (Gutsche (1964)).

The rotational blade position θ of 3 points is needed. In the example given in the report of Gutsche, these are $60°$, $180°$ and $300°$. The following equations are performed for each of these blade positions. The first step is performing the calculation in formula 11.1.

$$C_1 \cdot \sin(\theta) = \frac{J \cdot C}{0.7\pi} \cdot \sin(\beta) \cdot \sin(\theta) \tag{11.1}$$

This calculation consists of a constant C_1, which is multiplied by a factor depending on the blade position. The constant follows from the rate of advance for a 'substitute bearing surface' at the location of $r = 0.7 \cdot R$. This relates the inflow to the rotational speed at a certain radial location. This expression follows from the fact that the rate of advance changes during a rotation, due to the inclination angle. C is an empirical constant, which is equal to 2, to match the experimental results.

From this formula, the next step can be performed using formula 11.2.

$$\frac{n_\theta}{n_p} = 1 - C_1 \cdot \sin(\theta) \tag{11.2}$$

Here n_θ is depended on θ, as this is the effective rotational speed of the blade. The advance ratio is also corrected for as a result of the inflow angle. This is done using formula 11.3.

$$J_\theta = J \cdot \cos(\beta) \cdot \frac{n}{n_\theta} \tag{11.3}$$

J_θ is the advance factor of the 'substitute bearing surface', which is varies from straight inflow. In formula 11.4, the difference between this advance factor and the actual advance ratio is calculated.

$$\Delta J = J_\theta - J \tag{11.4}$$

For this approximation method, the K_T and K_Q curves of the propeller in open-water are a required input. From these graphs, the value of K_T or K_Q at a certain J should be known to compute the value at an angle for this J. Also the local derivative of both curves with respect to J are required. In formulas

11.5 and 11.6, the amount of change in both thrust and torque coefficient, as a result of the difference between advance ratio and advance factor, are calculated.

$$\Delta K_T = \frac{dK_T}{dJ} \cdot \Delta J \tag{11.5}$$

$$\Delta K_Q = \frac{dK_Q}{dJ} \cdot \Delta J \tag{11.6}$$

In formula 11.7, the local thrust coefficient of the 'substitute bearing surface' is calculated. This local thrust coefficient is different on different blade positions, as generation of thrust is non-uniform during the rotation in oblique flow. In formula 11.8, the same calculation is performed for the local torque coefficient.

$$\frac{K_{T\theta}}{K_T} = 1 + \frac{\Delta K_T}{K_T} \tag{11.7}$$

$$\frac{K_{Q\theta}}{K_T} = 1 + \frac{\Delta K_Q}{K_Q} \tag{11.8}$$

Lastly, from the three circumferential positions, it is possible to calculate the ratio between the thrust and torque coefficient of straight open inflow and oblique inflow. For the thrust coefficient, this is shown in formula 11.9, and for torque this is shown in formula 11.10.

$$\frac{K_{T\beta}}{K_T} = \frac{1}{3}\left(\left(\left(\frac{n_\theta}{n}\right)^2 \cdot \frac{K_{T\theta}}{K_T}\right)_{\theta=60^\circ} + \left(\left(\frac{n_\theta}{n}\right)^2 \cdot \frac{K_{T\theta}}{K_T}\right)_{\theta=180^\circ} + \left(\left(\frac{n_\theta}{n}\right)^2 \cdot \frac{K_{T\theta}}{K_T}\right)_{\theta=300^\circ}\right) \tag{11.9}$$

$$\frac{K_{Q\beta}}{K_Q} = \frac{1}{3}\left(\left(\left(\frac{n_\theta}{n}\right)^2 \cdot \frac{K_{Q\theta}}{K_Q}\right)_{\theta=60^\circ} + \left(\left(\frac{n_\theta}{n}\right)^2 \cdot \frac{K_{Q\theta}}{K_Q}\right)_{\theta=180^\circ} + \left(\left(\frac{n_\theta}{n}\right)^2 \cdot \frac{K_{Q\theta}}{K_Q}\right)_{\theta=300^\circ}\right) \tag{11.10}$$

As the K_T and K_Q values of straight inflow are known, the estimate of the propeller in oblique flow can be finished.